University of Alabama in Huntsville

LOUIS

2020

Digital optical correlator alignment monitoring system for astronomical telescopes

Tomasz Marek Lis

Follow this and additional works at: https://louis.uah.edu/uah-dissertations

DIGITAL OPTICAL CORRELATOR ALIGNMENT MONITORING SYSTEM FOR ASTRONOMICAL TELESCOPES

by

Tomasz Marek Lis

A DISSERTATION

Submitted in partial fulfillment of the requirements
for the degree of Doctor of Philosophy
in
The Department of Physics
to
The School of Graduate Studies
of
The University of Alabama in Huntsville

HUNTSVILLE, ALABAMA

2020

In presenting this dissertation in partial fulfillment of the requirements for a doctoral degree from The University of Alabama in Huntsville, I agree that the Library of this University shall make it freely available for inspection. I further agree that permission for extensive copying for scholarly purposes may be granted by my advisor or, in his/her absence, by the Chair of the Department or the Dean of the School of Graduate Studies. It is also understood that due recognition shall be given to me and to The University of Alabama in Huntsville in any scholarly use which may be made of any material in this dissertation.
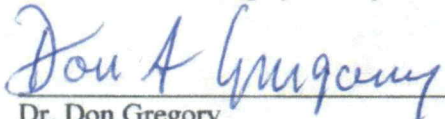
02/10/2020

(Student Signature)   (Date)
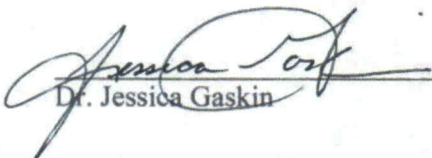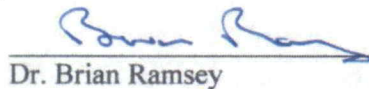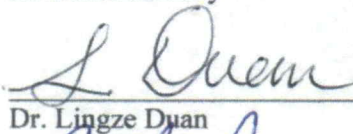
DISSERTATION APPROVAL FORM

Submitted by Tomasz Marek Lis in partial fulfillment of the requirements for the degree of Doctor of Philosophy in Physics and accepted on behalf of the Faculty of the School of Graduate Studies by the dissertation committee.

We, the undersigned members of the Graduate Faculty of The University of Alabama in Huntsville, certify that we have advised and/or supervised the candidate on the work described in this dissertation. We further certify that we have reviewed the dissertation manuscript and approve it in partial fulfillment of the requirements of the degree of Doctor of Philosophy in Physics.
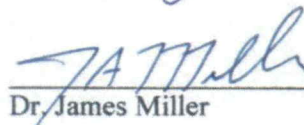
Dr. Don Gregory   2/10/20 (Date)   Committee Chair

Dr. Jessica Gaskin   2/10/20 (Date)
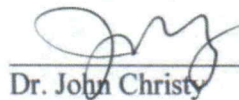
Dr. Brian Ramsey   2/11/20 (Date)

Dr. Lingze Duan   2/10/2020 (Date)

Dr. Patrick J. Reardon   2-10-20 (Date)

Dr. James Miller   02/25/2020 (Date)   Department Chair

Dr. John Christy   02/26/2020 (Date)   College Dean

Dr. David Berkowitz   2/26/2020 (Date)   Graduate Dean

iii

ABSTRACT

School of Graduate Studies

The University of Alabama in Huntsville

Degree _Doctor of Philosophy_   College/Dept.____Science/Physics_____

Name of Candidate _____Tomasz Marek Lis_____

Title___Digital Optical Correlator Alignment Monitoring System for Astronomical_____

_____Telescopes_____

The High Energy Replicated Optics to Explore the Sun (HEROES) program is a balloon-borne X-ray telescope mission to observe hard X-rays (~20 to 70 keV) from the Sun, the Crab Nebula and GRS 1915+105. The payload consists of eight X-ray mirror modules with a total of 114 optics, all mounted on a 6 m long optical bench. Each mirror module is complemented by a high-pressure xenon gas scintillation proportional counter. Attached to the payload is a camera that acquires star fields and then matches the acquired field to star maps to determine the pointing of the optical bench.

Slight misalignments between the star camera, the optical bench, and the telescope elements attached to the optical bench may occur during flight due to mechanical shifts, thermal gradients, and gravitational effects. These misalignments can result in diminished imaging and reduced photon collection efficiency. To monitor these misalignments during flight, a supplementary passive Bench Alignment Monitoring System (BAMS) was added to the payload. BAMS hardware comprises two cameras mounted directly to the optical bench and rings of LEDs mounted onto the telescope components. The LEDs in these rings are mounted in a predefined, asymmetric pattern

and their positions are tracked using an optical/digital correlator. The BAMS analysis software is a digital adaptation of an optical Joint Transform Correlator (JTC).

The aim is to enhance the observational proficiency of HEROES while providing insight into the magnitude of mechanically and thermally induced misalignments during flight. Post-flight analysis of the BAMS flight data showed that there was flexing of the payload due to thermal variations and sag with changing elevations which lead to HEROES pointing 3.6 arcminutes off-axis.

Abstract Approval: Committee Chair _Don A Gregory 2/11/20_
                                        Dr. Don A. Gregory   (Date)

                      Department Chair _JMiller 02/25/2020_
                                        Dr. James Miller

                      Graduate Dean   _____ 2/26/2020_
                                        Dr. David Berkowitz

v

ACKNOWLEDGMENTS

Throughout the writing of this dissertation I have received a tremendous amount of support and guidance. I would like to first thank my NASA advisor Dr. Jessica Gaskin who I am deeply indebted to. She has supported me throughout the writing of my dissertation and has spent endless hours editing my chapters and advising me when I was in need. Dr. Gaskin has been a constant source of encouragement and she has pushed me to be a better scientist and writer. Another individual I am extremely grateful to is my UAH advisor Dr. Don Gregory whose expertise in the field of optics has been a source of constant encouragement and help throughout the writing of this dissertation. Dr. Gregory's expertise was invaluable in the formulation of my research topic along with spending many hours editing my dissertation.

Another person I am extremely grateful to is John Jasper. John helped me tremendously throughout the work on my dissertation. John has provided me with expertise in computer programming and endless hours spent modifying the BAMS software. His assistance was invaluable to my success. I would also like to thank my NASA supervisors Dr. Andrew Keys, Roy Young and Paul Tatum whose continued support have allowed me to work on this dissertation.

I am thankful for Allyn Tennant providing me assistance to learn how to use the lextrct software he designed. I would also like to thank the members of my committee for

the help and commitment they gave me during my dissertation. I am grateful to the Marshal Space Flight Center and UAH for use of their facilities and funding to see my dissertation through to the end.

Nobody has been more important to me during the course of my work than the members of my family. I would like to thank my parents who supported and pushed me to achieve anything I set my mind to. I also want to thank June and David Carter who have helped tremendously throughout the course of my work. Most importantly, I want to thank my loving and supportive girlfriend Megan, who has been with me throughout my entire time working on this dissertation and has supported me endlessly in its completion.

TABLE OF CONTENTS

List of Figures

List of Tables

Acronyms

AOI	Area of Interest
AMS	Alignment Monitoring System
BAMS	Benchtop Alignment Monitoring System
C2C	Complex to Complex
CSBF	Columbia Scientific Balloon Facility
CTE	Coefficient of Thermal Expansion
FFT	Fast Fourier Transform
FFTW	Fastest Fourier Transform in the West
FWHM	Full Width Half Maximum
GPU	Graphics Processing Unit
HK	House Keeping
HXR	Hard X-ray
JTC	Joint Transform Correlator
LDB	Long Duration Balloon
PSF	Point Spread Function
PSD	Point Spread Density
PYAS	Pitch-Yaw Aspect System
R2C	Real to Complex
SAS	Solar Aspect System
SLM	Spatial Light Modulator
TI	Target Image
UAH	University of Alabama in Huntsville

Chapter 1

Introduction

In recent decades, the ability to focus X-rays has provided the instrumental basis for new discoveries in a relatively unexplored energy regime of the Electromagnetic Spectrum (EMS). Focusing higher energy photons, such as X-rays, requires unique optics and detectors because of their ability to penetrate through most materials. These optics are known today as grazing incidence optics, which means they utilize shallow angles to focus. These grazing incidence optics are therefore extremely sensitive to angular misalignments. When mounting X-ray optics modules and detectors on spacecraft or balloon borne craft for a flight mission there are many sources that can introduce misalignments such as thermal flexing due to Coefficient of Thermal Expansion (CTE) mismatch of the payload elements and gravitational sag. It is therefore critical to monitor the alignment between the optics and detectors during the mission so that image and spectroscopic data obtained during the flight can be optimally reconstructed. This is especially important for low-flux observations from faint sources. The alignment monitoring system for the High Energy Replicated Optics to Explore the Sun (HEROES), balloon-borne X-ray telescope was the first to employ an alignment monitoring system that takes advantage of a well-known optical architecture known as a Joint Transform Correlator. This dissertation describes the design, testing and implementation of this

alignment monitoring system which came to be known as the Bench Alignment

Monitoring System (BAMS) to track these misalignments and use them to reconstruct the

data obtained post-flight. This dissertation includes:

- A description of the HEROES payload and the BAMS requirements.

- The derivation and explanation of the physics involved in designing and
  constructing BAMS, along with the software development and design

- Ground testing of the BAMS analysis software and hardware pre-flight.

- Application of the BAMS data in the post-flight HEROES data analysis.

- Improvements to BAMS for future balloon-borne and space-based telescopes

1.1 Hard X-ray Focusing Telescopes

A Hard X-ray (HXR) focusing telescope observes astronomical sources in the ~10

keV to ~100 keV energy regime, which is on the high energy end of the X-ray band as

shown in Figure 1.1 [1].
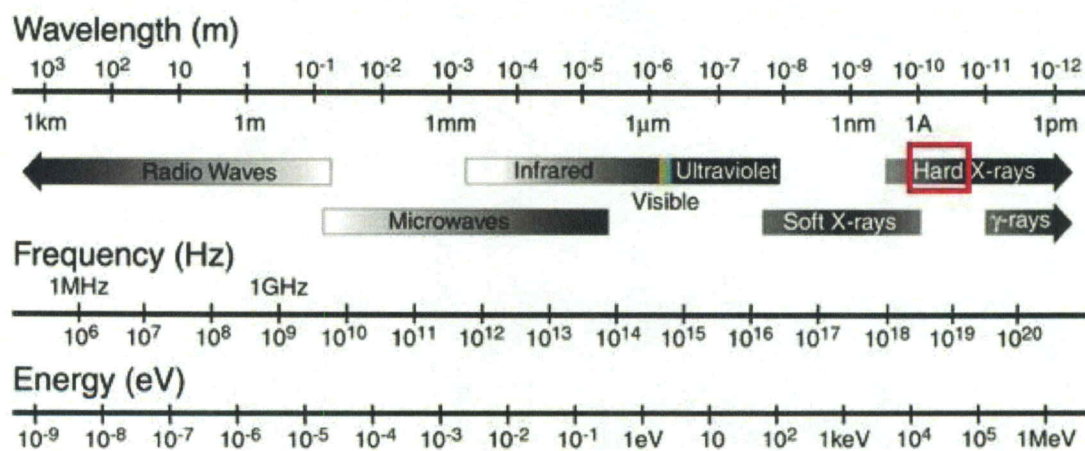
Figure 1.1: The electromagnetic spectrum with a red box around the section of the
electromagnetic spectrum where hard X-rays are located. Image credit: James H. Wittke,

2

School of Earth and Sustainability, Northern Arizona University. Reprinted with permission. [1]

Focusing these high-energy photons requires the use of specialized, high-precision optics known as grazing incidence optics. These precisely aligned optics focus the X-rays from an astrophysical source onto complimentary detectors for imaging and spectroscopy. As can be seen in Figure 1.2, ground based X-ray telescopes are not possible because HXRs, which are indicated by the green box, cannot penetrate far enough into the atmosphere to be sufficiently detected [2]. This means that either a high-altitude balloon, sounding rocket or a space-based payload must be used.

During flight, there are several issues that may cause the X-ray telescope to become misaligned and they are discussed in more detail in Section 2.3. The focus of this dissertation is on creating, developing and testing an alignment monitoring system suitable for a scientific balloon platform, but also applicable in any system requiring precise alignment monitoring
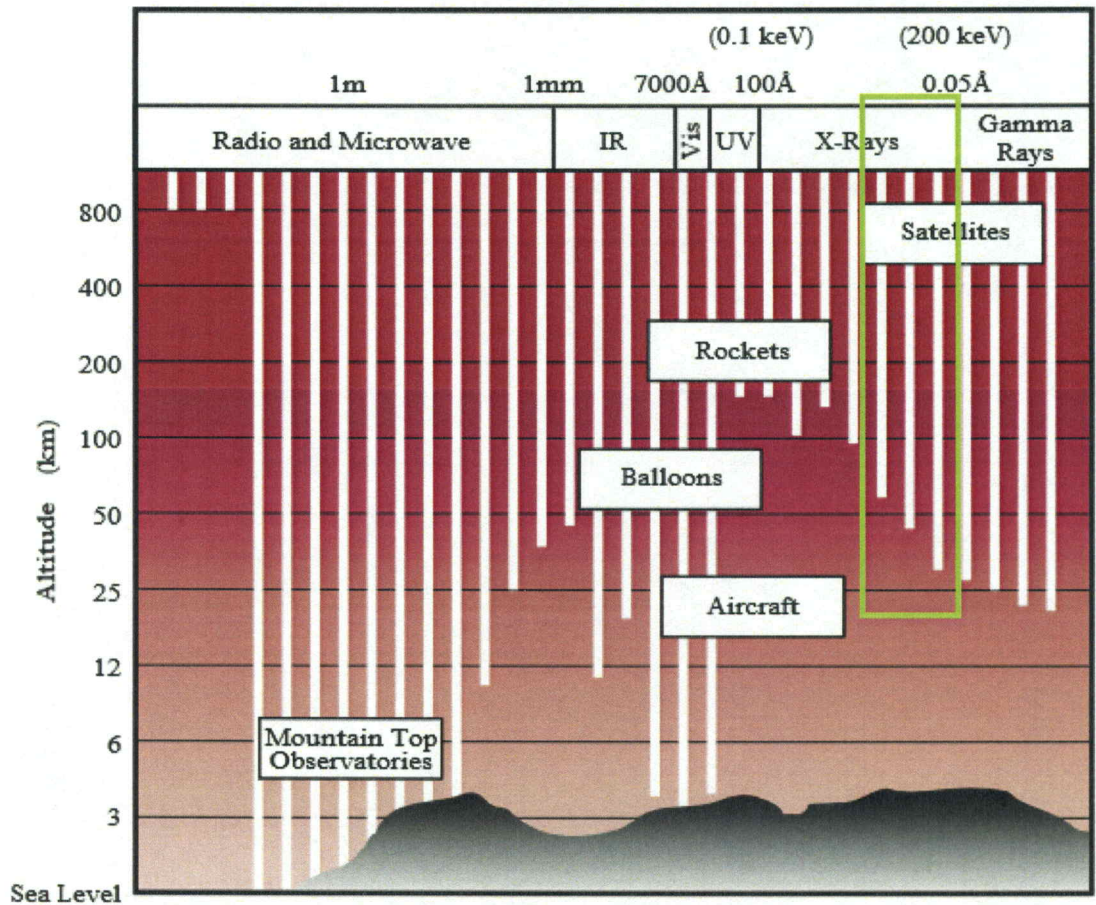
Figure 1.2: Electromagnetic spectrum absorption in the atmosphere with a green box drawn around the HXR portion. The hard X-rays do not appreciably penetrate farther than an altitude of 25 km. Image credit: Reproduced with permission of Stanford Linear Accelerator Center. [2]

1.1.1 X-ray Optics

HXRs require the use of grazing incidence optics for focusing because of their high energies. The most common HXR optic design uses the Wolter Type-I geometry as shown in Figure 1.3. This geometry consists of two reflections with the first being off a parabolic surface and the second off a hyperbolic surface [3].

4
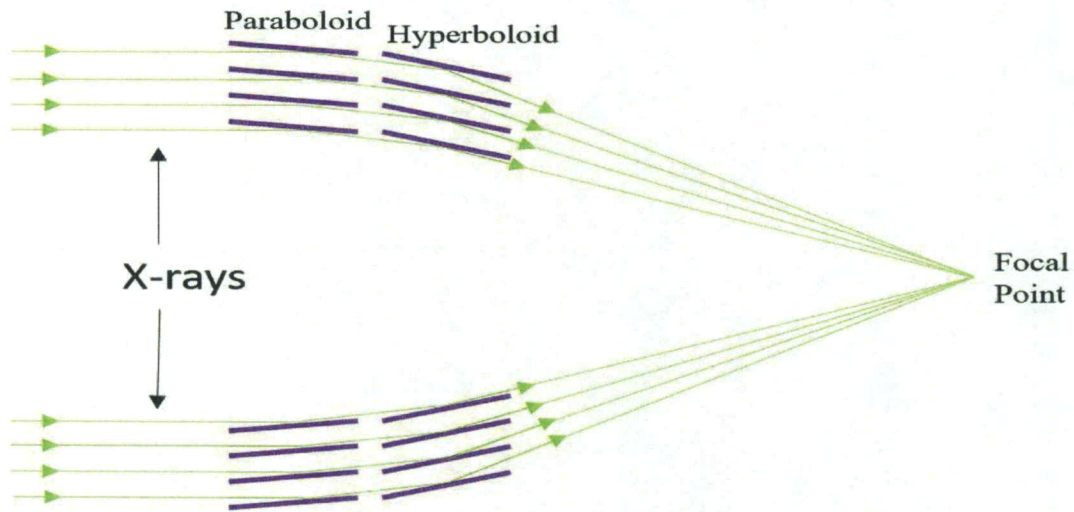
Figure 1.3: Wolter Type I geometry to focus X-rays. The image shows multiple of these grazing-incidence optic shells nested together and them focusing X-rays from an astrophysical source to a detector plane.

The desired angle for photons to strike these surfaces is known as the critical angle. The critical angle is the incident angle at which total external reflection occurs. When a photon strikes a surface at this angle or at any angle smaller than this, it will be reflected [4]. At these high energies, if the incidence angle of the HXR emission is larger than the critical angle, the X-ray will be absorbed, scattered or pass through the optic. The critical incidence angle is inversely proportional to the energy of the photon, so HXRs require extremely shallow angles to operate [5]. The critical angle can be derived from Snell's law

$$n_1 \cdot \cos(\theta_1) = n_2 \cdot \cos(\theta_2), \tag{1.1}$$

where θ_2 is 90° and $n_1 = 1$ since the photon comes from vacuum. This will yield the equation

$$\cos(\theta_{crit}) = n_2 \tag{1.2}$$

5

with $n_2 = 1 - \delta$ and θ_{crit} being the critical angle. For X-ray optics θ_{crit} will be much less than $1°$ so

$$\cos(\theta_{crit}) \approx 1 - (\cos(\theta_{crit}))^2 / 2 \qquad (1.3)$$

This yields

$$\theta_{crit} = \sqrt{(2\delta)}, \text{ where } \delta = (N \cdot Z \cdot r_e \cdot \rho \cdot \lambda^2) / (A \cdot 2 \cdot \pi) \qquad (1.4)$$

with N being Avogadro's number, Z is the atomic number of the surface element, r_e is the radius of an electron, ρ is the density of the material, A is the atomic weight, and λ is the wavelength of the incoming photon. Using Z/A of approximately 0.5 for heavy elements yields the following:

$$\theta_{crit} = 5.6 \left[\frac{\sqrt{cm}}{g*angstrom} \right] * \lambda * \sqrt{\rho} \text{ arcminutes} \qquad (1.5)$$

where λ is in Angstroms and ρ is in g/cm^3 [6]. Using this equation, Table 1.1 gives the critical angle for Iridium, which is typically used to coat the optics for improved reflectivity, for a few different photon energies.

Table 1.1: Critical angle of Iridium for various different energies.

Photon energy	Critical angle
20 keV	16 arcmin
40 keV	8.2 arcmin
60 keV	5.5 arcmin
75 keV	4.4 arcmin

6

To increase the effective photon gathering area of the telescope, many of these X-ray focusing optic shells are nested into a module. Some HXR telescope missions use multiple optics modules to further increase the collecting area. Having multiple optics modules requires multiple detectors, and alignment between each optics module and its detector. To account for any misalignment during flight, the alignment monitoring system must be sensitive enough to measure small deviations in the alignment of the optics modules to the detectors.

1.1.2 X-ray Detectors

HXR detectors are often designed to collect high energy photons for both imaging and spectroscopy. Two of the most common types of pixelated detectors for use on balloon-borne X-ray telescopes are solid-state detectors and gas based detectors. The type of detector used depends on the mission requirements for the energy range, energy resolution, imaging resolution, quantum efficiency, timing, etc.

Three HXR balloon flights from the last two decades are the High Energy Focusing Telescope (HEFT), the International Focusing Optics Collaboration for μCrab Sensitivity (InFOCμS), and the High Energy Replicated Optics (HERO). Both the HEFT and the InFOCμS missions used solid-state detectors, while the HERO mission used gas based detectors. Table 1.2 lists some of the characteristics from these three missions. All three have comparable energy ranges but different angular resolution requirements, with HERO being 0.25 arcminutes, HEFT with 1.5 arcminutes, and InFOCμS with 2.2 arcminutes [7].

Table 1.2: Characteristics for three different HXR balloon payloads which are HEFT, InFOCµS, and HERO. The table lists the energy range, angular resolution, effective collecting area and field of view for each mission. Table credit: Semiconductor radiation detection systems by INIEWSKI, KRZYSZTOF Reproduced with permission of TAYLOR & FRANCIS in the format Thesis/Dissertation via Copyright Clearance Center. [7]

Mission	HEFT	InFOCµS	HERO
Energy range (keV)	20-70	20-40	20-70
Angular resolution (arcmin)	1.5	2.2	0.25
Effective collecting area (cm^2)	108 at 30 keV 30 at 69 keV	42 at 30 keV	80 for 20-50 keV 20 at 70 keV
Field of view (arcmin)	12.6	9.6	9 at 40 keV 5 at 60 keV

1.1.3 Alignment Requirements for X-ray Telescopes

Monitoring the alignment between the optics and detectors is crucial when attempting to image HXRs from an astrophysical source. Any misalignment of the optics over the course of the flight must be taken into account when reconstructing the X-ray images from the detector data. Misalignments lead to decreased collecting area due to Wolter Type-I off-axis performance, which can lead to a loss of sensitivity. Figure 1.4 shows how the collecting area decreases versus energy as the relative angle between the source and optics goes farther off-axis. For low count sources, this decreased collecting area can lead to a target source not having enough counts to be distinguished above the background [4].
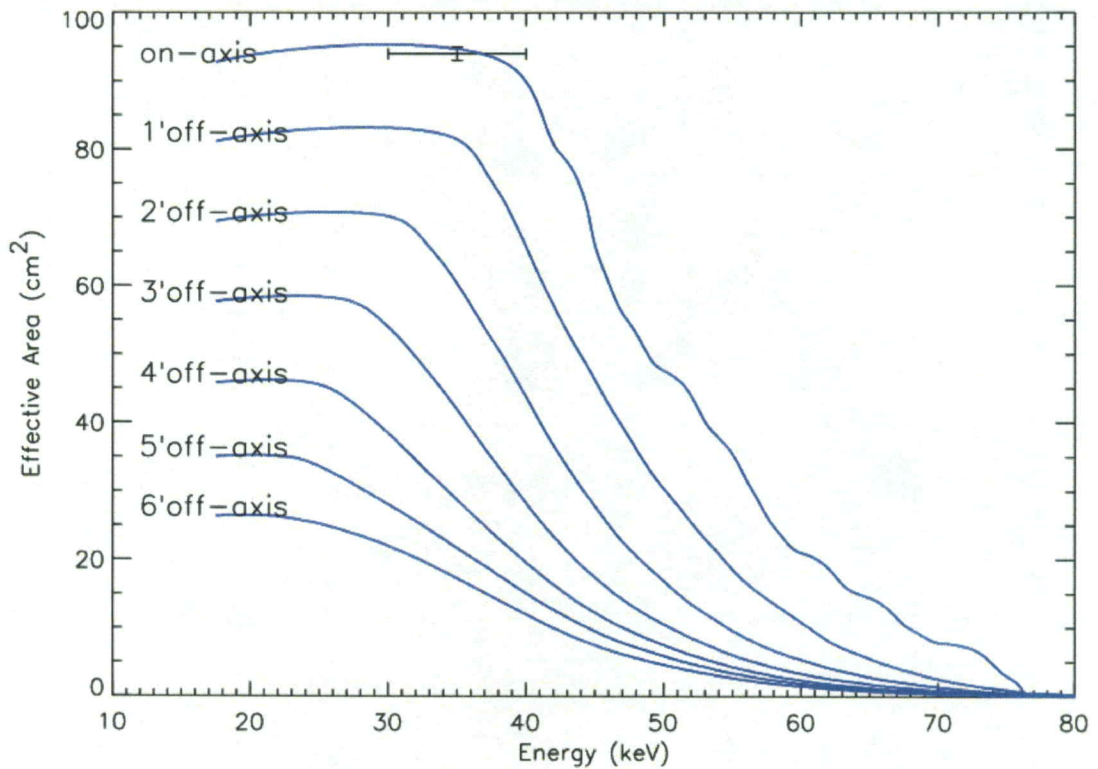
Figure 1.4: Collecting area in cm² vs photon energy in keV for off axis optical alignments ranging from on-axis to 6' off-axis for a Wolter-I configuration. Image credit: Journal of Astronomical Instrumentation by World Scientific Publishing. Reproduced with permission of World Scientific Publishing in the format Republish in a thesis/dissertation via Copyright Clearance Center. [4]

The relative angle between the source and optics module being off-axis also will induce aberrations and Figure 1.5 shows what happens to an image when the relative angle is off-axis by as little as 3 arcminutes. The left and right images have the optic module being shifted off-axis in the X-direction by -/+ 3 arcminutes respectively. The misalignment causes a "spidering" effect (or coma) to be present in the images and results in a loss of signal. This loss is due to incident photons striking the optic at an angle larger than the critical angle and either being absorbed or scattered [4].
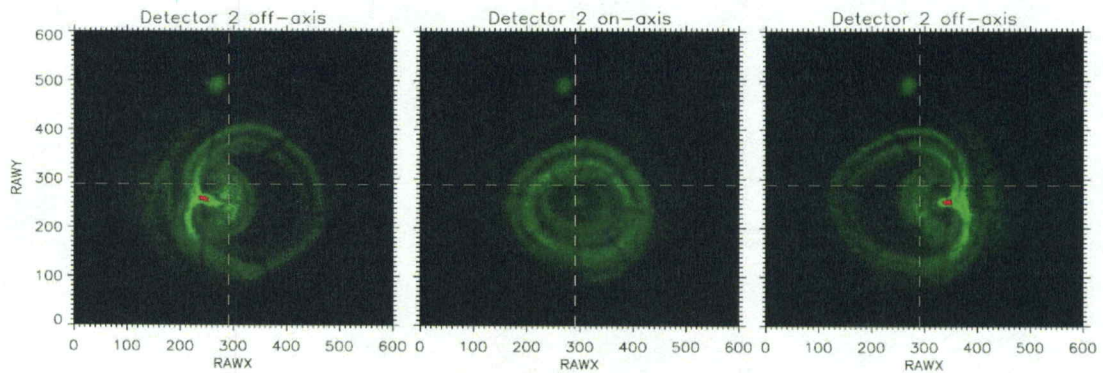
Figure 1.5: Images taken from an optics module that has three different alignment positions. The central image is on-axis with minimal distortions. The left and right images are taken when the optics module is off-axis +/- 3 arcminutes respectively. Image credit: Journal of Astronomical Instrumentation by World Scientific Publishing. Reproduced with permission of World Scientific Publishing in the format Republish in a thesis/dissertation via Copyright Clearance Center. [4]

There are many factors that can affect the alignment between the X-ray optics and their respective detectors during the duration of a balloon flight. Thermal gradients across the payload caused by the Sun's position relative to that of the telescope can result in flexure of the optical bench due to mismatched Coefficients of Thermal Expansion (CTEs) of the various components. During flight, the payload will also experience sag due to gravity. During launch and flight, the payload invariably experiences turbulence, which may cause shifts in components such as bolts, mounts, etc… which can potentially cause misalignments when compared to ground-calibration positions.

HXR telescope missions such as HEROES and HEFT have multiple optics modules and detectors that are intended to simultaneously view an astronomical X-ray source [7]. The data (energy and spatial information) from each detector is combined post-flight. Absolute knowledge of the alignment between the optics and their corresponding detectors is an essential piece of information needed to accurately

reconstruct the data into a single image. It is therefore imperative that any HXR flight have a system in place to monitor the alignment of the optics and detectors. This is especially true when observing faint astrophysical sources, when each photon collected is critical to resolving the source. The alignment of the optics to detectors should be at least consistent with the performance of the optics. For example, the HEROES alignment for optics that have a 33 arcsecond half power diameter (HPD) over a 6 m focal length would obviously need to be better than 33 arcseconds [4].

1.2 Comparison of Current Alignment Techniques and BAMS

To monitor misalignments that may occur during a flight, an alignment monitoring system is often installed. Having such a system allows for post-flight and perhaps real-time correction of off-axis distortions and reconstruction of the data obtained from an astronomical source. A few different X-ray telescope missions and their alignment monitoring systems are discussed and compared to BAMS in the following sections.

1.2.1 Chandra X-ray Observatory

The Chandra X-ray Observatory (Chandra) is a NASA X-ray telescope satellite mission that performs high-resolution (0.5 arcsec) imaging and spectroscopy of soft X-ray astrophysical sources such as supernova, matter around black holes and clusters of galaxies [8]. A drawing of the Chandra payload is shown in Figure 1.6 with the focusing optics at the front of the satellite and detectors (High Resolution Cameras) at the rear [9].
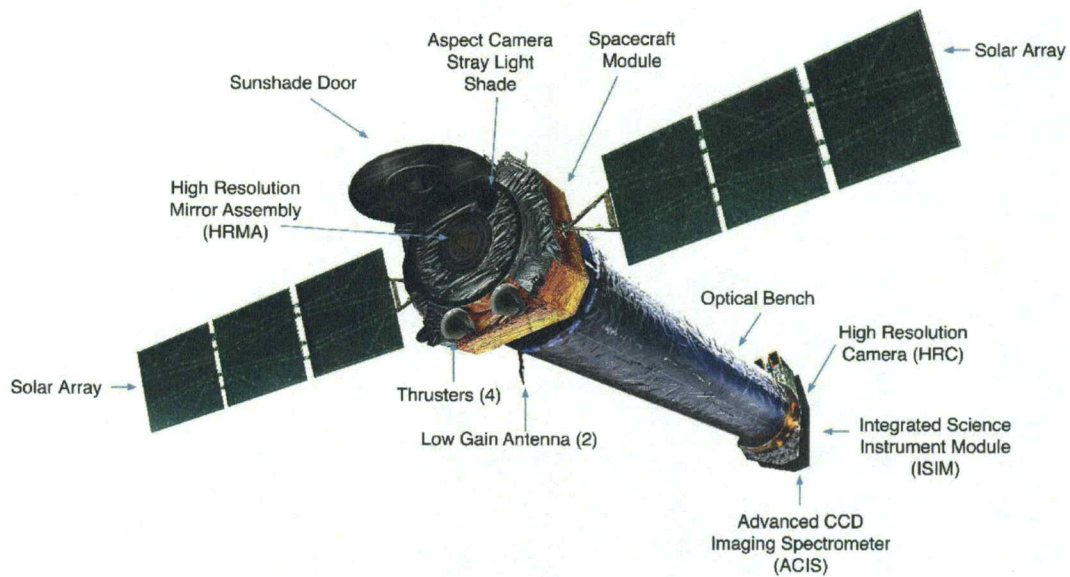
Figure 1.6: Model of the Chandra X-ray telescope with all of the components being shown. Image credit: NASA/CXC/SAO. Reprinted with permission. [9]

When Chandra achieved orbit, there was a rapid alignment shift of the optics relative to the detectors due to outgassing that had not been taken into account during ground calibration, which caused misalignments in the payload. There were initial concerns that thermal gradients on the payload could cause it to flex and therefore misalign the position of the optics to the detectors, which would create off-axis distortions in the reconstructed images obtained [10]. To monitor these misalignments an aspect alignment monitoring system was used.

The Chandra aspect alignment monitoring system uses a set of "fiducial lights" surrounding each of the detectors that emits light with a known wavelength of 635 nm toward the optics module as seen in Figure 1.7. This light is reflected down a periscope into the aspect camera assembly and then reflected into the aspect camera where lateral movement of the detector, with respect to the aspect system, can be determined [11]. This

system allows for monitoring of the alignment of the optic module to detector in the payload to a precision of better than an arcsecond for spatial resolution [11].
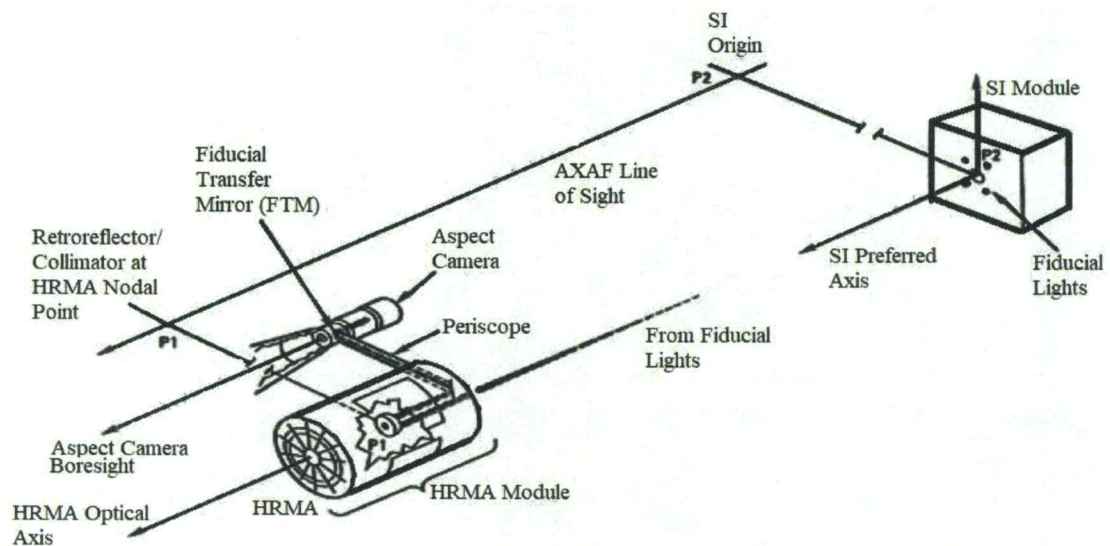
Figure 1.7: Chandra telescope internal structure showing the alignment monitoring system with the optics and detectors. Image credit: Chandra Proposers' Observatory Guide. Reprinted with permission. [11]

The alignment solution for the Chandra satellite only has one optics module with four nested optics shells. Unlike on the HEROES telescope, the Chandra alignment monitoring system was designed as Chandra was being designed. HEROES required such a system to be added after the telescope had already been built. Further, HEROES required that the alignment monitoring system not interfere with any of the existing science instruments, so installation of fiducial lights could not be done [11]. BAMS also has the ability to monitor multiple payload elements. In the case of HEROES, BAMS monitored multiple mirror modules independently without interfering with their primary functions.

1.2.2 Nuclear Spectroscopic Telescope Array (NuSTAR)

NuSTAR is an HXR satellite mission designed to image and perform spectroscopy of HXRs in the energy range 6 – 80 keV [12]. NuSTAR, shown in Figure 1.8, has optics at one end and detectors at the other end of the 10m long optical bench. NuSTAR uses a non-imaging alignment system of lasers mounted on the optical bench of the payload that shine onto a Position Sensitive Detector (PSD) at the other end of the Satellite [13].
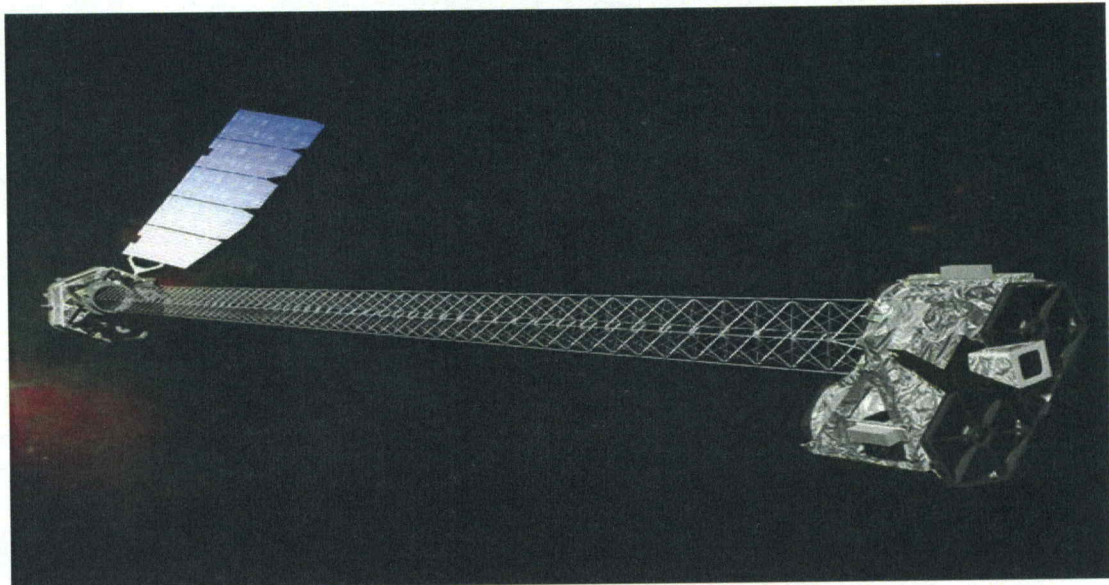
Figure 1.8: Model of the NuSTAR payload with optics at the right end and detectors at the left end of the Satellite. Image credit: NASA/JPL. [13]

The PSD operates by comparing differences in laser irradiance on the left and right extremes of the detector to determine horizontal alignment, and the top and bottom of the detector to determine vertical alignment. With this type of system being sensitive to stray light, a bandpass filter was mounted over the PSD to block out any wavelength that is not the specified wavelength of the laser used. Along with this filter, any remaining background was removed by turning the laser off 4 times a second, performing

a measurement of the background during this time, and subtracting it from the next laser position measurement. The NuSTAR alignment monitoring system is accurate to 2.68 arcseconds [14]. An alignment monitoring system like this was used on HERO but did not function as intended due to its small dynamic range. BAMS, on the other hand, has a field of view defined by the CCD and lens, which for the HEROES mission was 1 m at a distance of 3 m. BAMS is capable of subarcsecond accuracy as it uses a lens with a longer focal length and smaller CCD pixel size. BAMS also has the capability to determine angular misalignment while the laser and PSD system used on NuSTAR does not.

1.2.3 X-Calibur

X-Calibur is a balloon-borne polarimeter designed to observe HXRs in the 20-60 keV range. The X-Calibur payload is shown in Figure 1.9 with the optics and detectors 8 m away on the opposite end [15].

Figure 1.9: The X-Calibur payload in the Columbia Scientific Balloon Facility (CSBF) high bay in Ft. Sumner, New Mexico.

X-Calibur used an imaging system similar to BAMS to monitor the alignment of the optical bench. The AMS on X-Calibur used an LED ring similar to the one the BAMS system uses; however, there is a significant difference in how the alignment of the payload is determined (

Figure **1.10**). The X-Calibur AMS determines misalignment information by using an algorithm, designed by Fabian Kislat, which essentially determines each of the positions of the LEDS and does a centroid for each LED in the ring and determines movements from those centroids to determine misalignment information. An image of the LED ring used on the X-Calibur payload is shown in

Figure **1.10** [15].
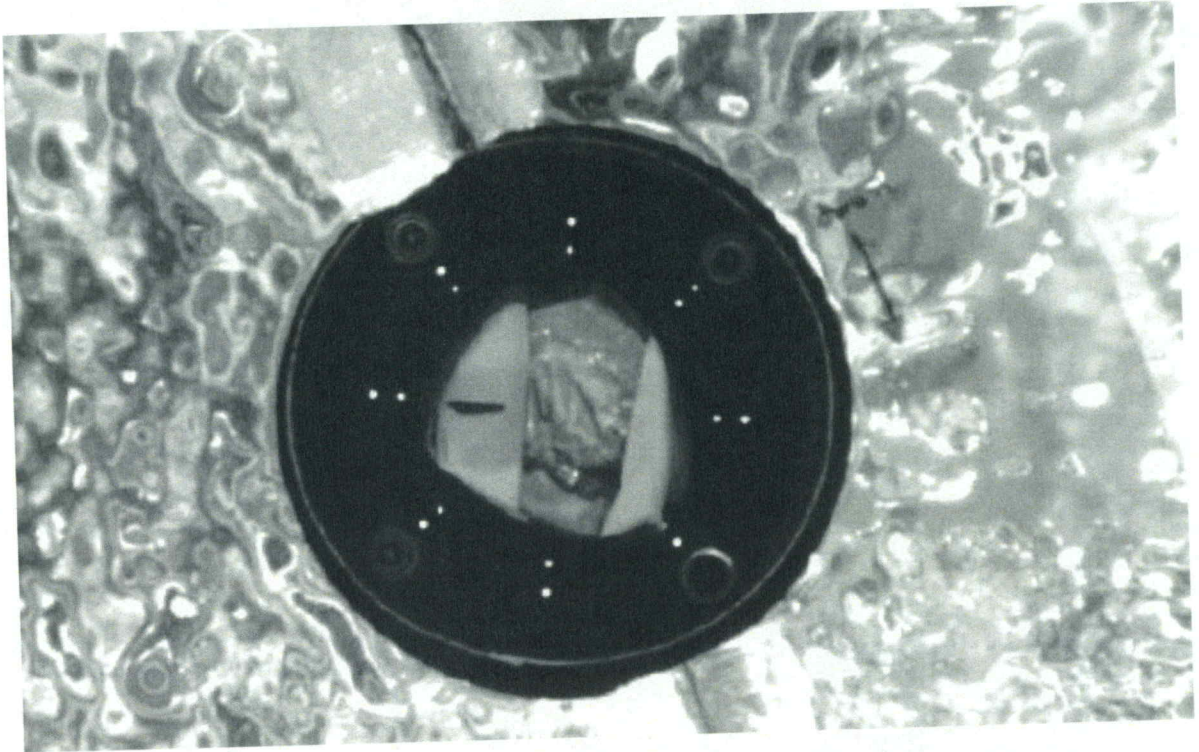
Figure 1.10: LED ring used on the X-Calibur payload for the alignment monitoring system.

While both BAMS and the X-Calibur AMS are imaging systems, there are stark contrasts in their performance and capabilities. The X-Calibur AMS, which met the system's requirements, is more sensitive to changes in LED brightness because of how the alignment is calculated. The X-Calibur AMS is also more sensitive to LEDs failing to illuminate because of how the algorithm determines misalignment. Alternatively, BAMS is not sensitive to changes in LED brightness and can operate with only three LEDs. Both systems have a large dynamic range and have the ability to determine angular and rotational misalignment [15].

1.2.4 HERO

The HERO telescope, precursor to the HEROES telescope, was a balloon borne X-ray telescope designed to view HXRs from astronomical sources. The HERO payload is shown in Figure 1.11, with optics at one end of the payload and detectors 6 m away on the opposite end. The goal was to image and perform spectroscopy of HXRs in the energy range 20 – 75 keV [16].

Figure 1.11: HERO payload post flight in Australia 2011. Image credit: NASA/MSFC. [17]

The alignment monitoring system on the HERO payload used a laser and a PSD that monitored the alignment between the optics and the detector mounting structure, henceforth referred to as the detector flange. The lasers were mounted on either side of the payload, one on the optics flange, the structure that the optics modules were mounted to, and one on the detector flange, with a PSD mounted on both the optics and detector flange, aligned with the laser from the other opposite end of the payload. This alignment

monitoring system proved to be ineffective and the problem was believed to be a mismatching of materials with different CTEs which caused the mounts to flex and the laser spot to wander off the detector. An attempt was made to correct this on the next flight by adding heaters to the mounts, but this did not solve the problem. The current theory as to why this alignment system failed to function is that stray light may have interfered with the PSD and corrupted any alignment data collected. For future flights, an alignment monitoring system that would have a large dynamic range along with minimal sensitivity to stray light was required. BAMS was designed because the laser and PSD system used on HERO did not function as intended [16].

1.3 HEROES Alignment Solution

The HEROES telescope (described in greater detail in Chapter 2) is a modification of the HERO payload which allows for observations of the Sun as well as astrophysical sources. HEROES required an alignment monitoring system that would be able to function in the harsh environments that are experienced during a balloon flight. The alignment monitoring system requirements include an accuracy better than 35 arcseconds and a large dynamic range. These requirements were met with the Bench-top Alignment Monitoring System (BAMS), which can monitor the movement of both the optics and the detectors relative to one another. BAMS uses a novel new imaging system to monitor the alignment of the HEROES optical bench. Unlike the example alignment monitoring systems in the previous sections, there were additional challenges associated with retrofitting such a system onto the existing payload. Applying alignment measurements generated by this new system to the X-ray data collected during the first HEROES flight

is one of goals of this work [18]. Figure 1.12 shows a CAD model of the BAMS system

mounted on the HEROES payload [19]. LED rings are placed on both the detector and

optics flanges with CCD cameras (attached to the central elevation flange) that take an

image every three seconds. Attached to each of the cameras are 16-mm focal-length

lenses, which are focused onto the 1/2" square CCD array that has a pixel size of

4.65x4.65 μm [19].
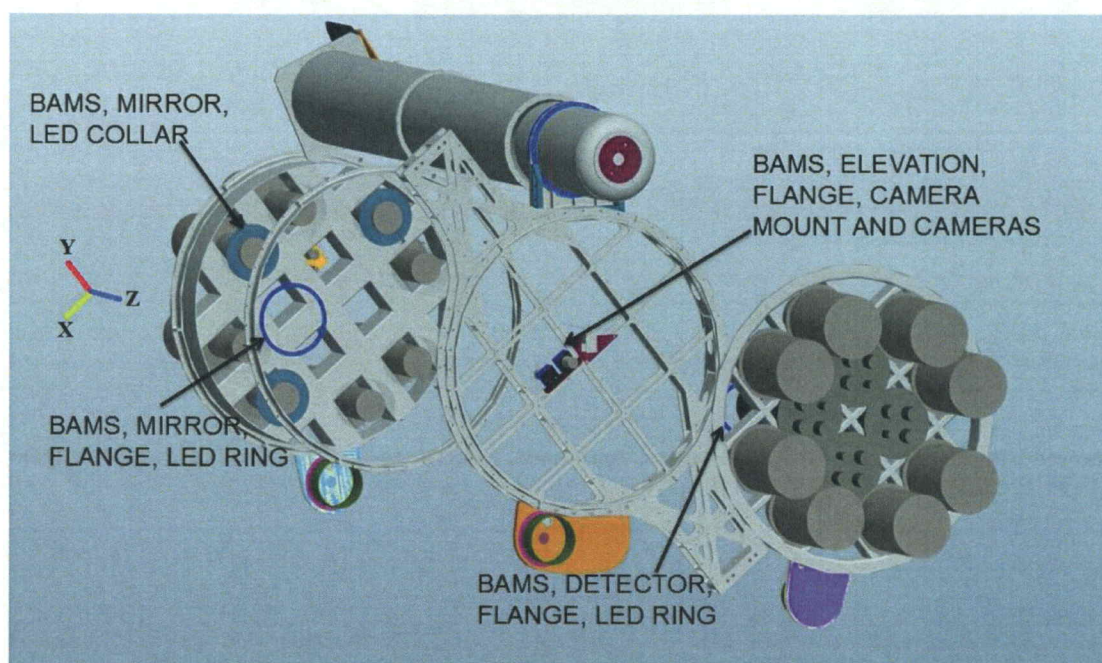
Figure 1.12: CAD model of the bench-top alignment monitoring system mounted to the
HEROES payload. There are two cameras on the center elevation flange pointed at both
ends of the payload, to image the LED rings mounted there. Three LED rings are
attached to optics modules and one ring on the optics flange. There is one LED ring
attached to the detector flange. Image credit: Alex Sobey NASA/MSFC. [19]

The images obtained from the CCD cameras were analyzed post-flight using software developed to determine any movement that may have occurred in the LED rings. BAMS makes use of a Fourier optical technique known as the Joint Transform Correlator (JTC) to continuously compare images [19]. The JTC is discussed in greater detail in Chapter 3 of this dissertation.

1.4 Chapter Summary

The HEROES balloon-borne telescope is designed to examine the hard X-ray regime of the EMS, which is still not very well explored at high angular resolution. HEROES makes use of X-ray optics to focus the high-energy photons onto complimentary detectors. These optics require the use of shallow angles to focus the photons, making them very sensitive to misalignments. These misalignments can greatly impact the scientific data collected by the detectors. X-ray missions such as Chandra, NuSTAR, and HERO employ the use of alignment monitoring systems to monitor the movement of the payload. However, these alignment monitoring systems are not practical for the HEROES payload due to small dynamic range or interference with heritage hardware. The BAMS system used for HEROES was designed to accurately report alignment information and it is described later in this dissertation.

Chapter 2

HEROES Mission

2.1 Scientific Balloon Flights and Environment

Scientific balloon flights endure extreme environments during the duration of their missions. The payload will experience large changes in temperature, low pressure environments and possibly turbulent winds that can shake the payload. During flight, it is possible for the payload to be caught in a wind current that can carry it over multiple states before the payload and balloon are brought back to the ground.

2.1.1 Balloon Environment

X-rays from astrophysical sources are absorbed in the atmosphere well before reaching the ground, which is why HXR payloads need to be flown on a high-altitude balloon, sounding rocket or satellite. Scientific balloons typically fly at an altitude between 30 and 42 km, which puts the balloon above 99% of the atmosphere. As shown in the top graph of Figure 2.1, the column density of air is inversely proportional to altitude. The bottom graph of Figure 2.1 shows how the fraction of X-rays decreases in the atmosphere for increasing photon energy at various altitudes [20].
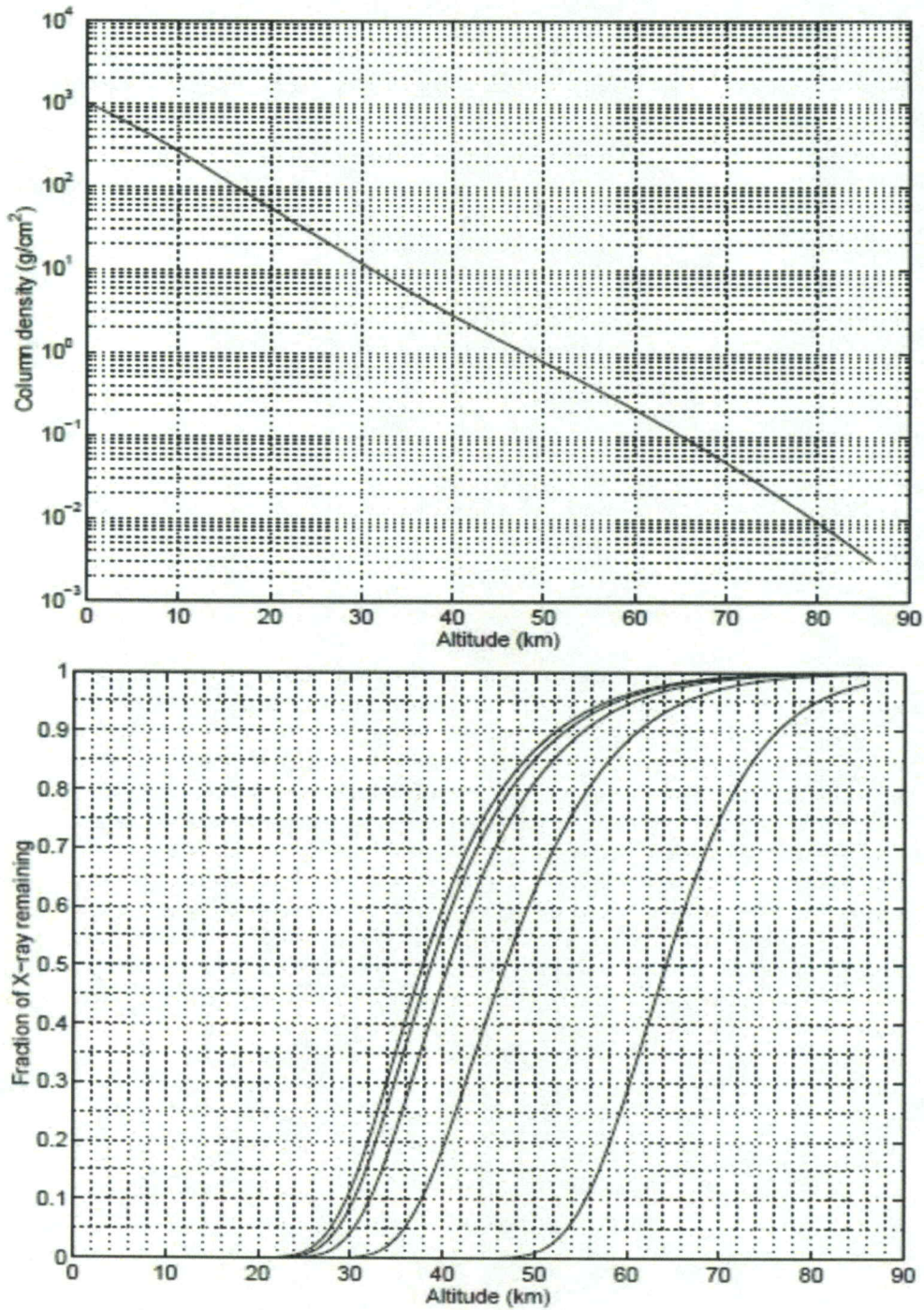
Figure 2.1: Density of the atmosphere versus altitude is shown in the upper chart. The lower graph shows the fraction of X-rays that penetrate through the atmosphere as a function of altitude. The curves from right to left are X-rays with energies 10, 25, 40, 55, and 70 keV respectively. Image credit: Chi Ming Hubert Chen. [20]

23

Balloon payloads face extreme variations in temperature during their ascent, as shown in Figure 2.2 [21]. The payload can experience temperatures as low as -55 °C while at 10 to 20 km altitude. The temperature increases to around -20 °C when the payload reaches a float altitude of approximately 38 km, the point at which the payload is no longer ascending [21,29]. It takes approximately 3 hours for a balloon borne payload to reach float altitude [29]. The payload must be able to withstand these large temperature fluctuations or be heated. As the payload increases in altitude the pressure the payload experiences decreases and can reach a pressure as low as 0.3 kPa [22].
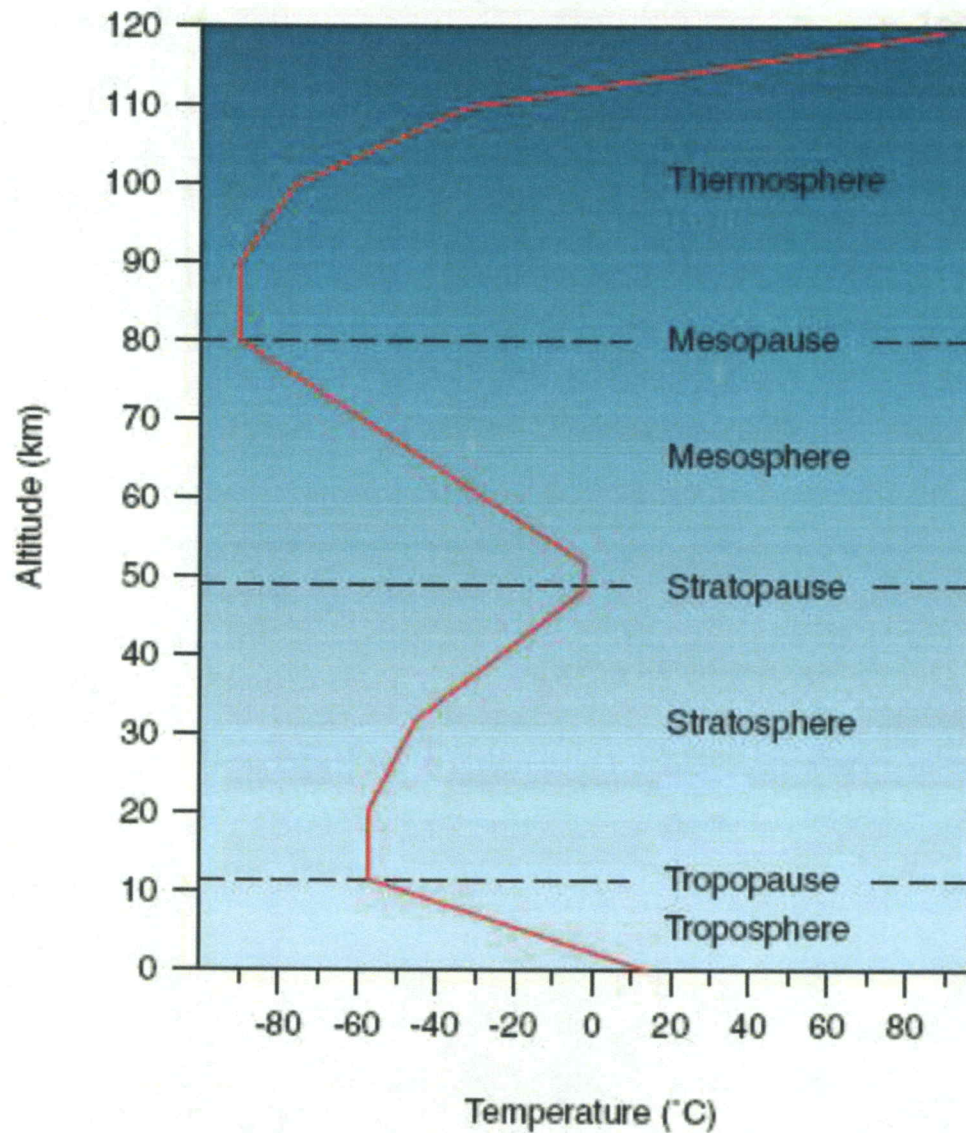
Figure 2.2: Temperature versus altitude graph with different layers of the atmosphere labeled. Image credit: The source of this material is the COMET® Website at http://meted.ucar.edu/ of the University Corporation for Atmospheric Research (UCAR), sponsored in part through cooperative agreement(s) with the National Oceanic and Atmospheric Administration (NOAA), U.S. Department of Commerce (DOC). ©1997-2017 University Corporation for Atmospheric Research. All Rights Reserved. [23]

2.1.2 Scientific Balloons and CSBF

The Columbia Scientific Balloon Facility (CSBF) is an organization that specializes in launching scientific balloon payloads and supports many balloon missions every year. CSBF has several facilities that are used for different types of balloon flights such as conventional flights (which can last a couple of days), Long Duration Balloon (LDB) flights (which can last a few weeks) and Ultra Long Duration Balloon (ULDB) flights (which can last up to 100 days) [24,27]. Although sounding rockets go to a higher altitude, their flight times are much shorter and typically last 5-20 minutes [25]. Flying a payload on a balloon is a relatively cheap way to lift a payload above the bulk of the atmosphere. The other option for longer duration flights would be a satellite, which can cost hundreds of millions of dollars versus millions of dollars for a balloon flight [20].

HEROES was flown on a conventional balloon from Ft. Sumner, New Mexico. Conventional balloon payloads are flown on zero-pressure balloons, which can expand to 39.57 million cubic-feet in volume and are comprised of a polyethylene film that is only 0.002 cm thick [18,27]. An image of what a zero-pressure balloon looks like can be seen in Figure 2.3 [26]. These balloons are designed to slowly leak out excess helium to balance the pressure inside the balloon that of to the outside environment. These balloons can carry up to 3,600 kg (or 8000 lbs), and typically float at an altitude of approximately 24-26 miles [27]. The HEROES payload weighed approximately 5500 lbs [18]. Conventional flights are typically flown out of Fort Sumner, New Mexico during the fall and spring [28].

Figure 2.3: Image of a zero pressure balloon right before launch. Image credit: NASA/MSFC. [26]

2.2 HEROES Background

HEROES was a balloon-borne flight mission designed to view the Crab Nebula, GRS 1915+105 and the Sun in the 20-75 keV photon range. HEROES was funded through the NASA Hands On Project Experience (HOPE) training opportunity that provided NASA Civil Servants experience with flight missions, and included training in standard NASA mission procedures. The HEROES telescope was a follow-on to the HERO balloon payload, with the added capability to observe the Sun as well as astronomical X-ray sources [18]. HERO was the first mission to obtain focused images of the Crab Nebula in the HXR energy range of 20-75 keV with an angular resolution of approximately 26 arcseconds [29]. The HERO payload was designed at the Marshall Space Flight Center (MSFC) in Huntsville, Alabama and flew four times during 2001 to 2011, with the most recent flight launching from Alice Springs, Australia. The majority

of the hardware on the HEROES payload was heritage hardware from the HERO flight. However, there were multiple upgrades that were added to the HEROES payload. Some of these upgrades included hardware added to give HEROES the ability to observe the Sun as well as astrophysical sources and the new BAMS alignment monitoring system [18].

2.3 Gondola Structure, Star Camera, and SAS

The HEROES gondola and payload are shown in Figure 2.4 with several of the key components labeled. The aluminum frame surrounding the optical bench, as seen in Figure 2.4, is known as the gondola [18]. The gondola has multiple components that are used to point the telescope. The magnetometer backed differential GPS system provides details required for course pointing in azimuth to +/- 30 arcminutes. Along with a shaft angle encoder and inclinometer to provide course elevation movement to within +/- 10 arcminutes. After the course pointing has been determined, a gyroscopically-controlled inertial-mode system with a day/night star camera then determines the fine pointing and gyro drift compensation of the payload [18].
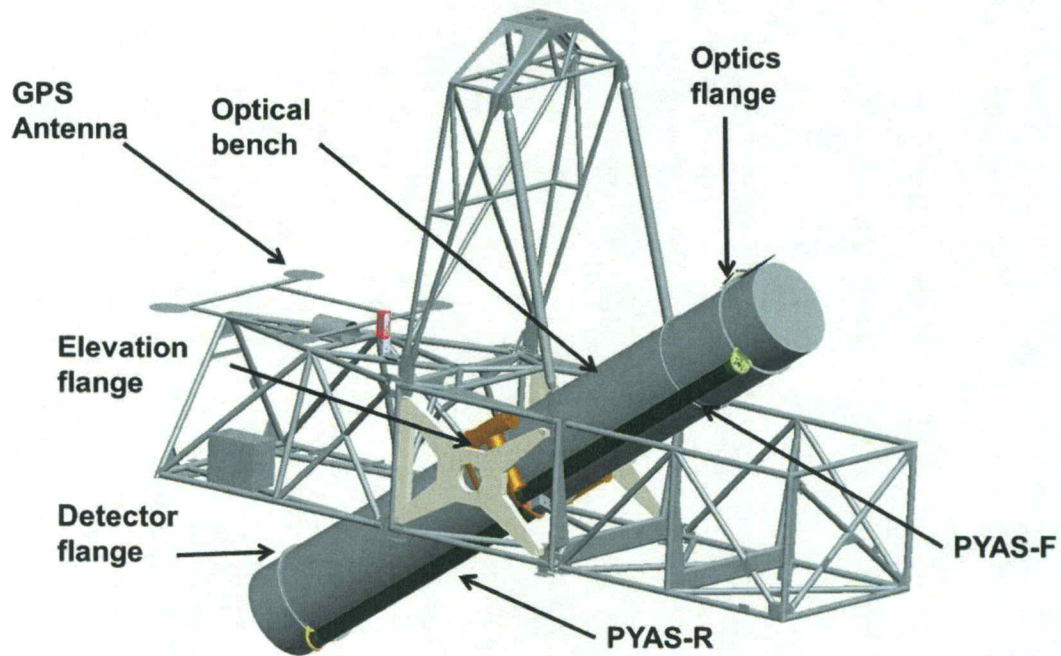
Figure 2.4: The HEROES gondola and payload with several components listed. Image credit: NASA/MSFC.

The optical bench provides structure for mounting the optics flange and detector flange and is divided into two separate 1-m diameter cylinders connected to the elevation flange. The portion of the optical bench that supports the detectors is made of aluminum and the portion of the optical bench that supports the optics modules is made of carbon fiber wound with an appropriate matching coefficient of thermal expansion (CTE). The optical bench and gondola were painted a bright white to help minimize the amount of solar radiation absorbed during flight, aiding in thermal regulation across the observatory [18].

In addition to BAMS, there is another alignment monitoring system attached to the optical bench. This system is the Solar Aspect System (SAS) as seen in Figure 2.5 [30,18]. The SAS was designed to determine alignment between the optics and detectors

during solar observations. The SAS comprises two components: the Pitch/Yaw Aspect System (PYAS) and the Roll Aspect System (RAS). PYAS consists of two subsystems the PYAS-F and PYAS-R, where F and R stand for front and rear respectively. These systems are attached to the elevation flange and record images of the Sun on 1 megapixel CCD cameras with each pixel corresponding to approximately 10 arcseconds [30].
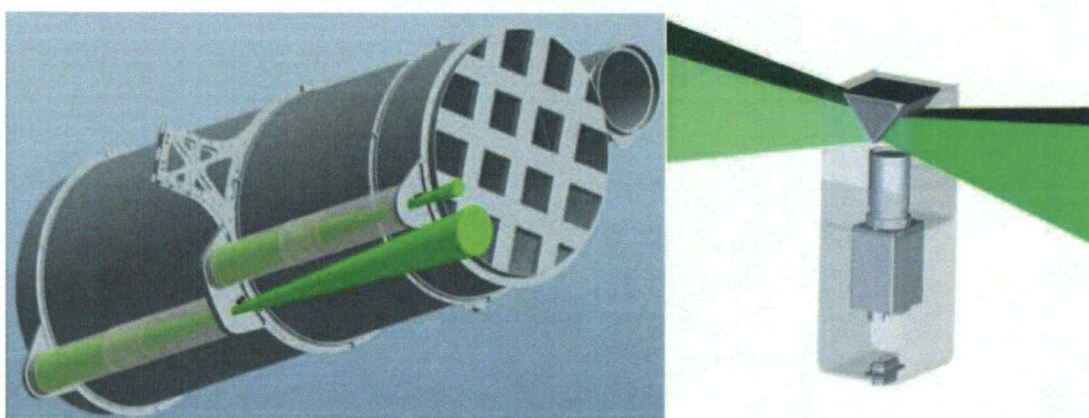
Figure 2.5: The two components of the SAS with PYAS on the left and RAS on the right. Image credit: reproduced with permission of IEEE. © [2013] IEEE. [18]

Not shown in Figure 2.4 is the Star camera with stay light baffle, which is attached to the other side of the elevation flange and is co-aligned with the optics modules. The star camera was used to determine the fine position of the payload while observing astronomical sources during the night. The Star Camera is an Apogee U9 Alta series camera that has a sensor size of 3072 x 2048 pixels attached to a Takahashi FSQ-106ED lens. The Star camera has a shutter attached that was used during solar observations to protect the sensor from solar radiation damage [18].

2.4 HEROES Optics and Detectors

The HEROES telescope includes 8 optics modules, each aligned to a detector 6 m away. The optics modules and detectors are the same as those used during the HERO flights [18]. In this section, the characteristics of the optics and detectors are described.

2.4.1 HEROES Optics

The optics in the HEROES payload were developed and fabricated in house at the Marshall Space Flight Center (MSFC). The optics are conical approximations of a Wolter Type I geometry that are formed using an electroformed nickel replication process and then sputter coated with iridium. As shown in Figure 2.6 there are eight optics modules inside the HEROES payload with 5 of the modules containing 14 optic shells and the other 3 modules containing 13 optic shells [18]. Each module is mounted with a tip/tilt mechanism so that they can be aligned to the detectors and then locked in place prior to flight [18].
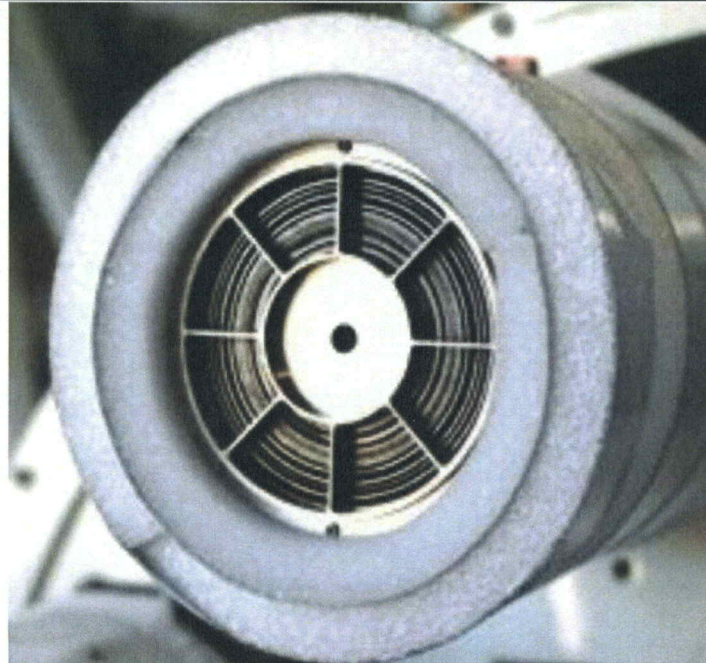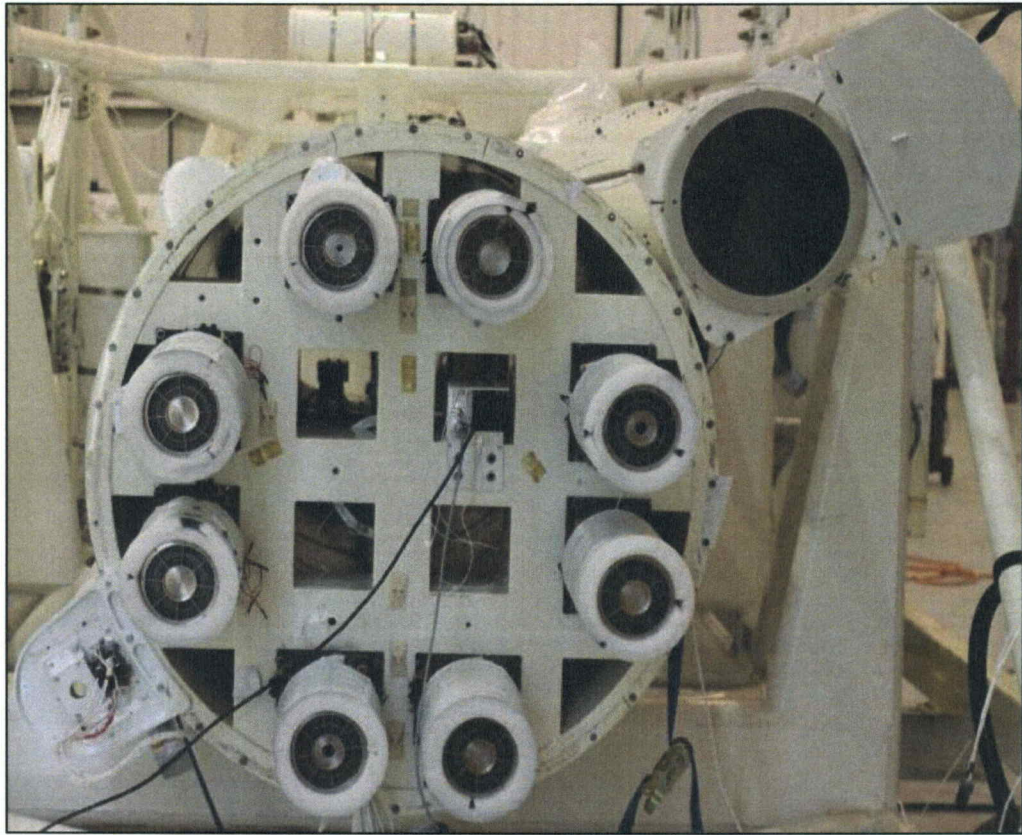
Figure 2.6: The top image shows the Optics flange with the 8 optics modules installed. The image on the bottom shows the nesting of optics shells inside one of the optics modules. Image credit: NASA/MSFC.

Table 2.1 lists the main characteristics of the HEROES optics modules [18]. The optics modules have an average angular resolution of approximately 13 arcseconds at Full Width Half Maximum (FWHM). Individually, the optics have better angular resolution, but due to slight alignment errors during mounting, the module angular resolution is degraded [18].

Table 2.1: Key features of the HEROES optics modules. Table credit: reproduced with permission of IEEE. © [2013] IEEE. [18]

Characteristic	Value
Optics shells per module	14 (in 5 of the modules) 13 (in 3 of the modules)
Inner, outer shell diameters	50, 94 mm
Total shell length	610 mm
Coating	Sputtered iridium, ~ 20 nm thick
On-axis geometric effective Area	~ 90 cm^2 at 40 keV ~ 21 cm^2 at 60 keV
Angular resolution (module)	~13 arcsec FWHM ~26 arcsec HPD
Field of View	9 arcmin at 40 keV 5 arcmin at 60 keV

2.4.2 HEROES Detectors

The detectors used were also designed and fabricated in house at MSFC. The detectors are Gas Scintillation Proportional Counters (GSPCs) and are shown in Figure 2.7 mounted to the HEROES payload. The operation of GSPCs starts with an incident X-ray photon passing through a beryllium window [18]. This photon is converted into ultraviolet (UV) light, which then passes through a 7-mm thick window and is detected by a position sensitive photomultiplier tube (PMT). These PMTs are multi-anode (X-Y

position) with an effective pixel size of 100 μm, which allows for position information to be determined [4]. A 60 keV photon will produce 10^4 UV photons, detected and centroided to determine the location for each event on the focal plane [31]. The detectors employ the use of taps which are readout channels within the detector that are used to determine the energy and position of X-ray events [4].
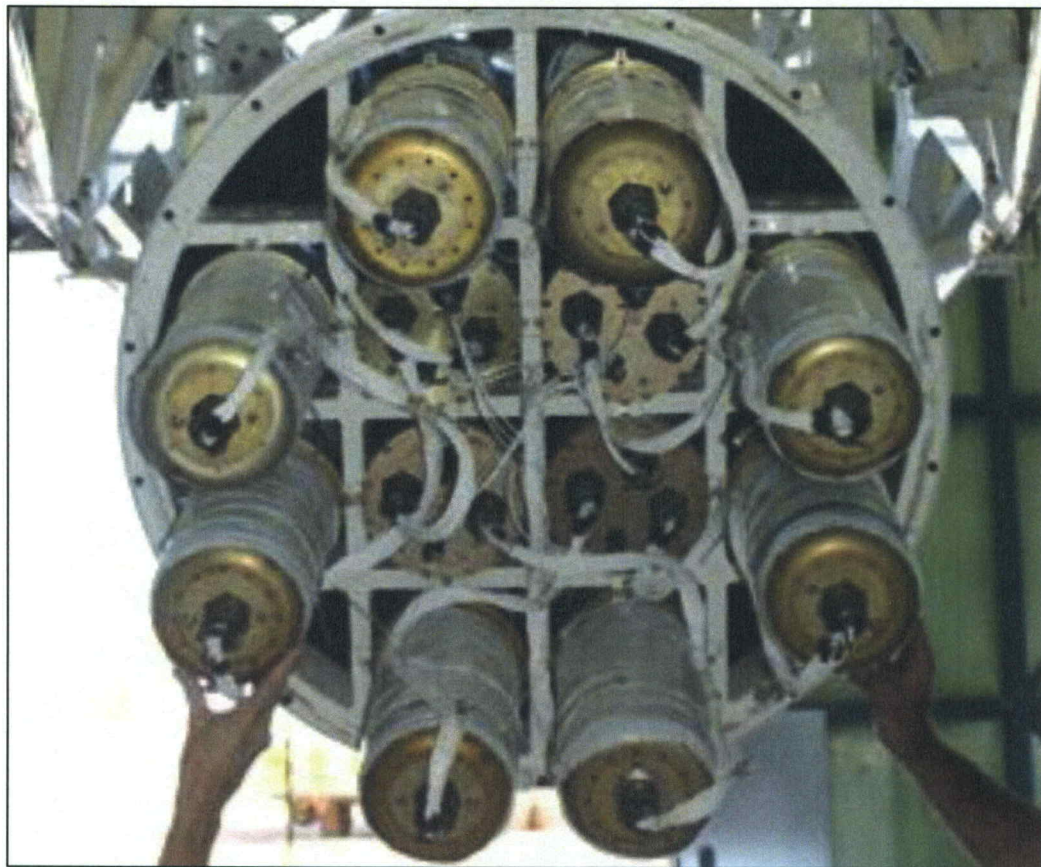
Figure 2.7: Eight GSPC detectors mounted in the HEROES payload. The payload is 1 m in diameter for scale. Image credit: reproduced with permission of IEEE. © [2013] IEEE. [18]

Table 2.2 lists the key characteristics of the HEROES detectors [18]. The detectors have a FWHM energy resolution of 6% at 30 keV and 4.5% at 60 keV. They

are filled with a mixture of Xenon and Helium gas at a mix ratio of 96% and 4% respectively. The detector entrance window is made of thin beryllium that allows 6 keV and higher energy photons to pass through [18]. Each detector has roughly 20 cm^2 of collecting area with a spatial resolution of approximately 350 μm [31].

Table 2.2: Key characteristics of the HEROES detectors. Image credit: reproduced with permission of IEEE. © [2013] IEEE. [18]

Characteristic	Value
Number of detectors	8
Fill Gas	56 mm of Xe + Helium (96/4) @ 106 pa
Light emitting region	4 mm deep
Exit window	7 mm Suprasil
Position resolution	330 μm (25-35 keV)
	400 μm (35-45 keV)
Energy resolution (FWHM)	6% @ 30 keV
	4.5% @ 60 keV
Quantum Efficiency	99% (40 keV)
	89% (60 keV)
Entrance Window	3.2 mm Beryllium
Measured Spatial Resolution (FWHM)	420 μm (15-25 keV)
	330 μm (25-35 keV)
	400 μm (35-35 keV)
Sensitive Area	~20 cm^2

2.5 Alignment of the HEROES Optics and Detectors

After the optics and detectors are installed, the optics modules are aligned to the detectors using a laser and then an X-ray source mounted to the alignment fixture as shown in Figure 2.8 [29]. The gondola and the fixture are separated by 100 ft and then leveled to better than 1°. The gondola and fixture are aligned to each other using a collimated laser placed in the "Gondola" mounting hole in the fixture and then adjusted

until the laser light passes through two calibration apertures on the optical bench. The first hole is at the optics flange and the second is located at the elevation flange.

The optics are then roughly aligned by mounting a laser in the "Optics Modules" mounting holes shown in Figure 2.8. The tip/tilt mount of the optics module is used to align the optics modules to the detectors. This step is then repeated for the remaining optics. The detectors are bolted into place; their positions are not adjustable. The optics modules are then finely aligned by placing an X-ray source into each of the corresponding optics module alignment holes on the fixture and analyzing the images taken by the corresponding detectors. The resulting alignment between the optics and detectors is approximately 30 arcseconds [29].

Figure 2.8: Alignment fixture used to alignment the optics modules of the HEROES payload. Image credit: reproduced with permission of IEEE. © [2014] IEEE. [29]

During flight, there are several factors that could cause misalignment between the optics modules and detectors. Misalignment can be a shift in the vertical, horizontal, and/or a twisting of the optical bench. The worst misalignment experienced is twisting of the payload; the optics and detector flanges being angularly misaligned with one another, while a horizontal or vertical shift simply shifts the position of the source on the detector. If the optics module mounts are not sufficiently locked into place and the payload experiences turbulence during launch, it is possible that the alignment can be disturbed. The payload also will experience gravitational sag which is a function of the elevation of the optical bench. Thermal flexing was also a concern due to fact that thermal gradients on the optical bench will cause flexing. This is most apparent when the payload is at an angle to the Sun and a single side is exposed to the solar radiation. With all of these possible misalignments during flight, a system was needed to monitor the movement of the payload. The solution for monitoring the alignment of the HEROES payload was BAMS, an imaging alignment monitoring system that can track the relative movement between the optics and detectors to an accuracy of 35 arcseconds [19].

2.6 Chapter Summary

Balloon-borne payloads have been used to fly numerous scientific flight payloads over the years and have the ability to fly for multiple days. Balloon-borne scientific payloads experience harsh environments during flight such as extreme temperatures and low pressures. Due to the fact that HXR photons are attenuated by the atmosphere, balloon-borne payloads need to be able to observe sources for multiple hours to capture enough photons to obtain an image of a source, and because of this, multiday flights are

37

required to observe multiple sources. The HEROES mission was a balloon-borne scientific payload to obtain high resolution HXR images from astrophysical sources and the Sun. The HEROES payload was the successor to the HERO payload and used heritage hardware along with several hardware upgrades such as the SAS, BAMS, etc... The HEROES telescope has 8 optics modules with a total of 114 optics used on the HEROES payload, designed to work in the 20-75 keV energy range. The detectors used were multianode GSPCs with an effective pixel size of 350 μm and having the ability to centroid the HXR photon events to obtain position information. The BAMS system was specifically designed for the HEROES payload to satisfy science requirements of the mission for accurate alignment monitoring information of the optical bench without interfering with scientific operations.

Chapter 3

BAMS Overview

Preamble: This majority of this chapter is taken directly from

T. Lis, J. Gaskin, J. Jasper and D. A. Gregory, Opt. Eng. **57** (1), 013104 (2018).

https://doi.org/10.1117/1.OE.57.1.013104

3.1 BAMS Overview and Hardware

BAMS was designed to detect misalignments between the optics and detectors on the HEROES payload. The BAMS system required hardware that could be integrated into the existing observatory and be able to withstand the harsh environments faced during a high-altitude balloon mission. To meet the HEROES science requirements, BAMS had to be able to:

1. Survive at temperatures between -50°C to 30°C and tolerate a low-pressure environment of a few Torr

2. Track movement of any alignment ring to within 35 arcseconds accuracy (discussed later)

3. Fit onto the existing optical bench without interfering with telescope operation

The BAMS system, as mounted on the HEROES payload, is shown in Figure 1.12 [19]. This system consists of two CCD cameras attached to the elevation flange on the optical bench. One camera is facing the optics flange and one is facing the detectors. As part of the BAMS system, a ring of LEDs is attached to the optics module mounting flange and three additional LED rings are attached directly to the optics modules themselves. The flange that the detectors are mounted on also has an LED ring attached to it. BAMS measures misalignments by tracking the movement of LED rings mounted to both the optics and detector flanges and the optics modules.

The BAMS cameras are model DMK41BU02 and have a pixel size of 4.65 µm x 4.65 µm, filling a total sensor size of ½ inch diagonal [32]. Attached to the cameras are 16 mm fixed focal length lenses from Edmund Optics, model NT67-714, with a diameter of 33.0 mm [33]. This camera-lens system provides a field of view that is 22.7 degrees [33,32]. Attached to the lens is a UV/visible cutoff filter, model NT65-796, also from Edmund Optics. Figure 3.1 below shows the transmission percentage versus wavelength of various filters from Edmund optics [34]. The R-72 filter used transmits approximately 90% at wavelengths above 750 nm. This was selected because the LEDs used for the system have a wavelength of 950nm [35].

Infrared Filters
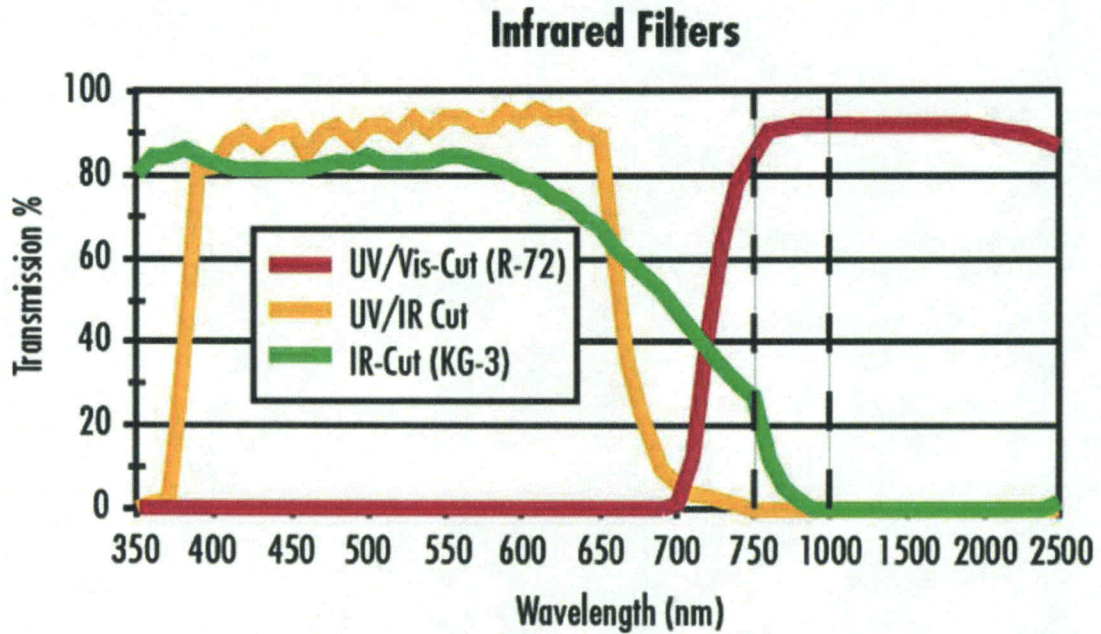
Figure 3.1: A chart showing the transmission % versus the wavelength of three different filters from Edmund Optics. The red UV/vis-Cut (R-72) line corresponds the filter used for the mission. Image credit: Image courtesy of Edmund Optics. All rights reserved. [34]

This camera-lens-filter combination was designed to withstand the environments faced during flight, for the large field of view enabling all of the LED rings attached to the optics and detector flanges to be imaged at once, to limit sensitivity to scattered light through use of a filter, and for its ability to achieve 1 arcminute resolution. The resolution (or plate scale) of BAMS in the HEROES configuration is calculated using:

$$Arcsec\ per\ pixel\ =\ \frac{pixel\ size\ [mm/pixel]}{Focal\ Length\ Lens\ [mm]} * \left(\frac{180°}{\pi}\right) * 3600\ [arcsec/degree] \qquad (3.1)$$

A pixel size of 4.65 μm and a focal length of 16 mm yields a plate scale that is 59.95 arcsec/pixel (~ 1 arcmin/pixel) for the BAMS cameras [36]. A method was used for

locating the centroid of the correlation signal (described later) to provide sub-pixel resolution to 0.06 arcseconds (0.001 arcminutes).

The LEDs were selected to have a peak wavelength of 950 nm (to be distinguished from stray visible light from outside sources) and a relatively small diameter of 1.8 mm, and then inserted into an LED ring in an irregular circular pattern. This small diameter yields a correspondingly small image on the CCDs, providing good alignment position sensitivity via the Joint Transform Correlator (JTC) [35]. The LEDs were arranged in an asymmetric and nonrepeating pattern on the rings to allow the BAMS software to determine the rotational alignment of the ring.

The LED rings shown in Figure 3.2 were fabricated in-house at MSFC using a 3-D printer, model Stratasys Fortus 360. The LEDs were wired to provide continued operation even if one (or more) LEDs failed. This was done by wiring a small circuit board with a shunt and LED in parallel so that the voltage would pass through the shunt if the LED failed and not change the voltage in the system. These LED-shunt boards were wired in series along the LED ring and to keep the voltage constant a current driver board was used.
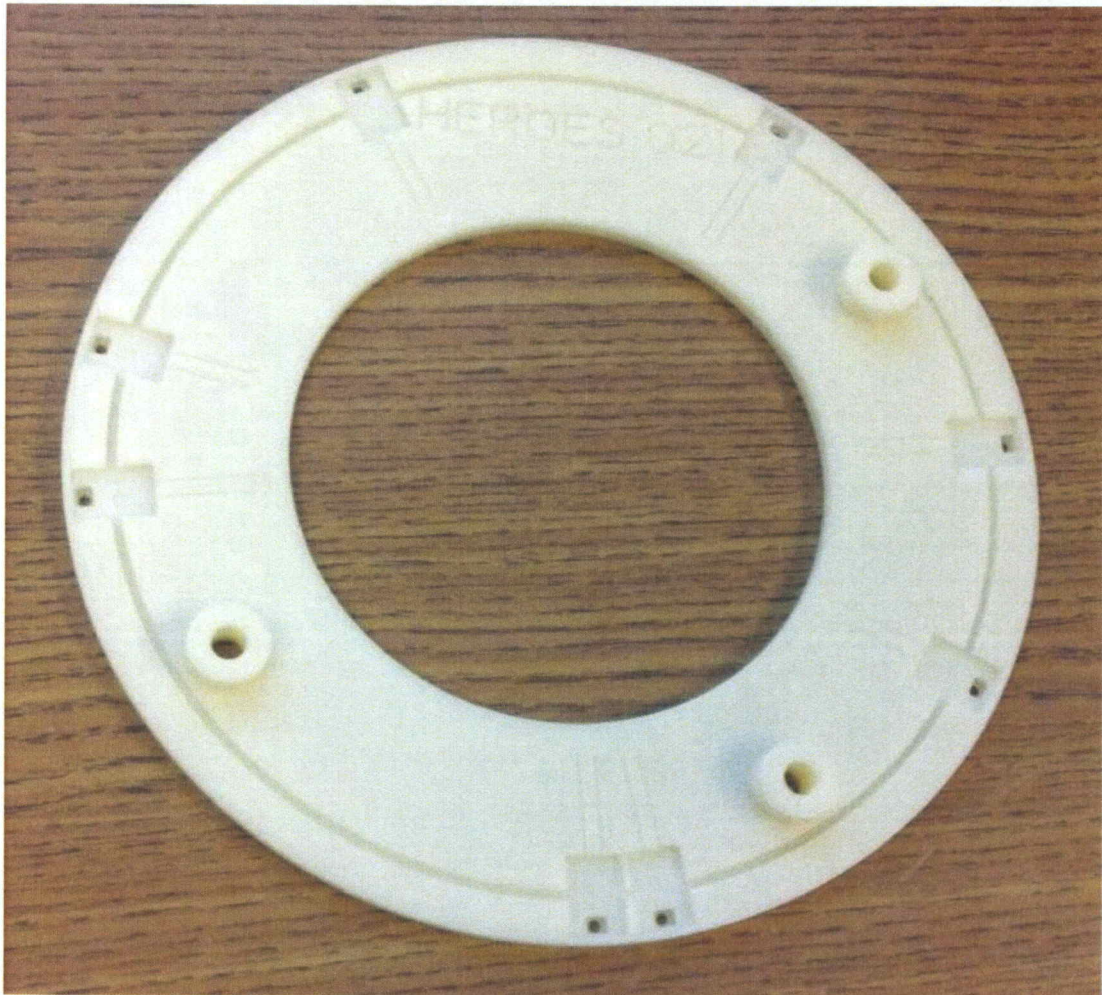
Figure 3.2: A BAMS optics-flange LED ring after fabrication and before any of the LEDs or circuit boards were mounted. The LEDs are mounted at a radius of 11 cm from the center of the ring.

The onboard HEROES computer recorded an image from the BAMS cameras every three seconds. This image acquisition time was chosen given the fact that alignment changes within across the payload are not expected to happen on short timescales, and also to prevent the onboard hard drive from running out of space. These images were processed by the BAMS software post-HEROES flight to determine if any movement of the LED rings occurred. Real-time operation (with real-time alignment correction) is possible, but has not yet been implemented due to challenges presented by

the additional onboard processing requirements such as having a full sized Video card on the payload. Figure 3.3 is an image of the LEDs (on 4 separate rings) mounted on the optics module flange and 3 optics modules taken by one of the on-board cameras during the HEROES flight. Each of the LED rings was clocked to a different orientation to allow for differentiation. This ensures that BAMS is able to track any specific ring without interference from the other rings in the camera's field of view.
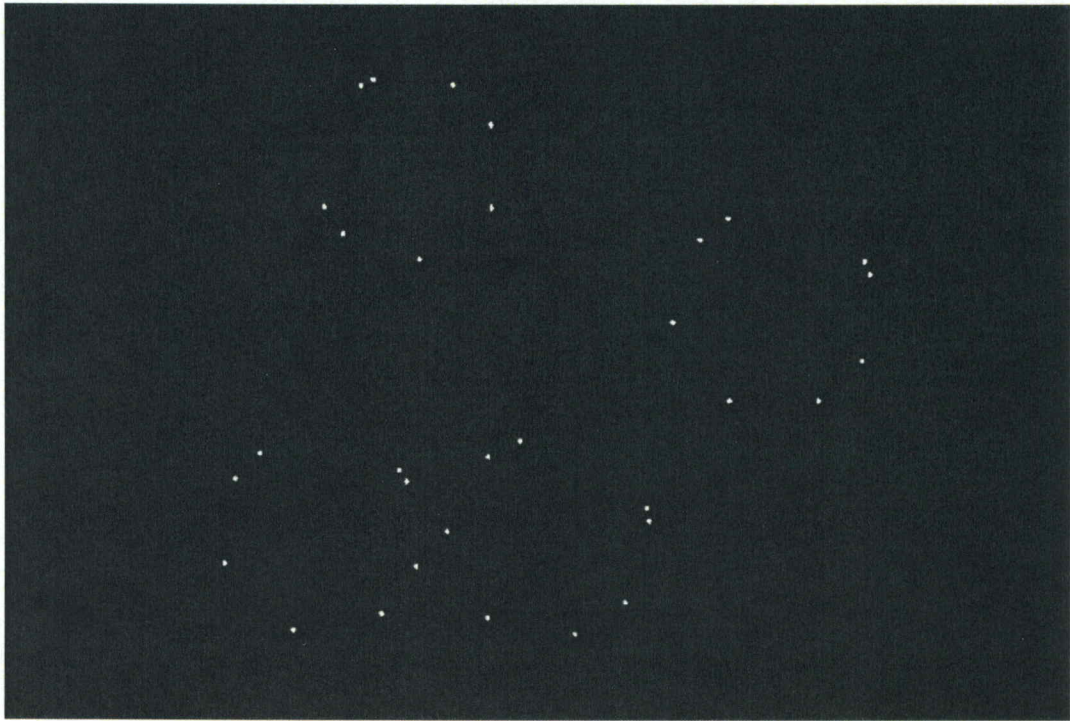
Figure 3.3: FITS file image (taken in flight) of the LED rings affixed to the HEROES optics flange. The LED rings are easily distinguishable from one another due to their respective orientations and location on the optics flange. Credit to NASA/MSFC.

3.2 Physics Overview

The BAMS software works by using the JTC to be able to track the misalignment of a payload. BAMS is a digital adaptation of the optical JTC, which is described in detail in this section. The full complex (amplitude and phase) digital optical correlator takes advantage of a number of mathematical operations, but specifically the Fourier transform. The total information contained in the original function (scene) being transformed is still contained in the transformed version; it is simply redistributed. It is this redistribution that allows a more efficient interrogation by another function through a simple multiply. In this case, the multiply is complex, containing real and imaginary terms representing the individual amplitude and phase components.

The purely optical JTC works by transforming a test scene using a lens and then taking the magnitude square on a detector and then making this the new test scene. This new test scene is then Fourier transformed again and the result produces a correlation signal along with a DC term. In the purely optical JTC shown in Figure 3.4 and Figure 3.5 both the known and test scenes are displayed in the same plane and encoded in coherent light, usually with the use of a spatial light modulator (SLM). This can be seen in the input plane at P_1 illuminated by coherent light with targets centered at $(0, b/2)$ and $(0, -b/2)$ and is represented by the equation:

$$U_1(x, y) = g(x, y + b/2) + h(x, y - b/2) \tag{3.2}$$

A single lens (at P_2) Fourier transforms the sum of the two scenes, and is represented by the following equation:

$$U_2(f_x, f_y) = G(f_x, f_y)\, e^{-i\pi f_y b} + H(f_x, f_y)\, e^{+i\pi f_y b} \tag{3.3}$$

45

This coherent sum of the transforms is detected (magnitude squared) by a camera at P_3

and represented in the following equation:

$$I(f_x, f_y) = \begin{bmatrix} |G(f_x, f_y)|^2 + |H(f_x, f_y)|^2 \\ + G(f_x, f_y)H^*(f_x, f_y)e^{-i2\pi f_y b} \\ + G^*(f_x, f_y)H(f_x, f_y)e^{+i2\pi f_y b} \end{bmatrix} \qquad (3.4)$$
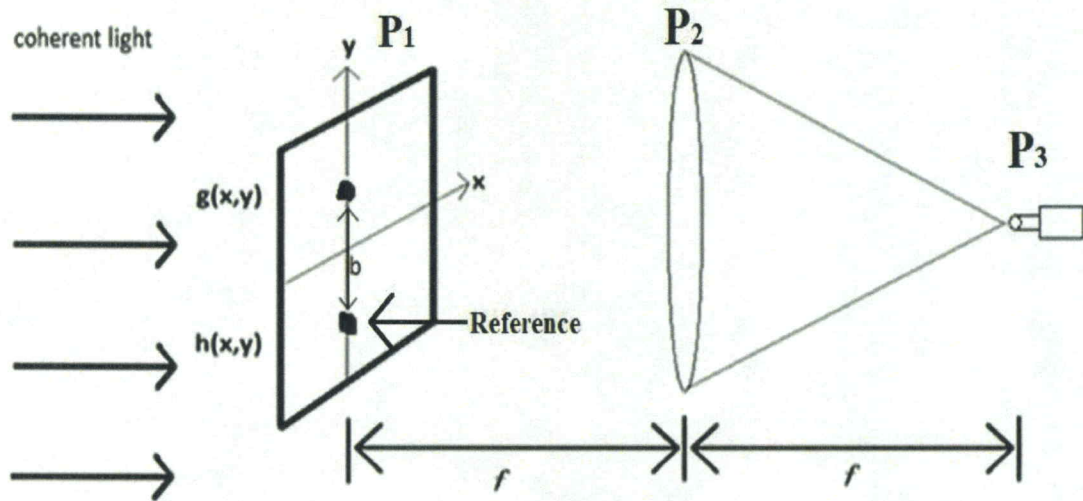
Figure 3.4: First part of purely optical JTC is a test scene at P_1 being illuminated by coherent light which is then Fourier transformed by a lens at P_2. This is then imaged by a detector at P_3 and the magnitude square is taken.

The image from P_3 is then displayed on a second SLM which is also illuminated

at P_4 with coherent light and represented by the equation:

$$U_3(x, y) = \begin{bmatrix} g(x, y) \otimes g^*(-x, -y) + h(x, y) \otimes h^*(-x, -y) \\ + g(x, y) \otimes h^*(-x, -y) \otimes \delta(x, y - b) \\ + g^*(-x, -y) \otimes h(x, y) \otimes \delta(x, y + b) \end{bmatrix} \qquad (3.5)$$

46

After being Fourier transformed by another lens at P_5, two identical diffraction orders

result and each one corresponds to the correlation between the two scenes [37].

$$g(x, y) \otimes h(-x, -y) \otimes \delta(x, y - b) = \iint_{-\infty}^{\infty} g(\xi, \eta) h(\xi - x, \eta - y + b) d\xi d\eta \qquad (3.6)$$

$$g(-x, -y) \otimes h(x, y) \otimes \delta(x, y + b) = \iint_{-\infty}^{\infty} h(\xi, \eta) g(\xi - x, \eta - y - b) d\xi d\eta \qquad (3.7)$$

The result of the second Fourier Transform is then displayed in the output plane of P_6.
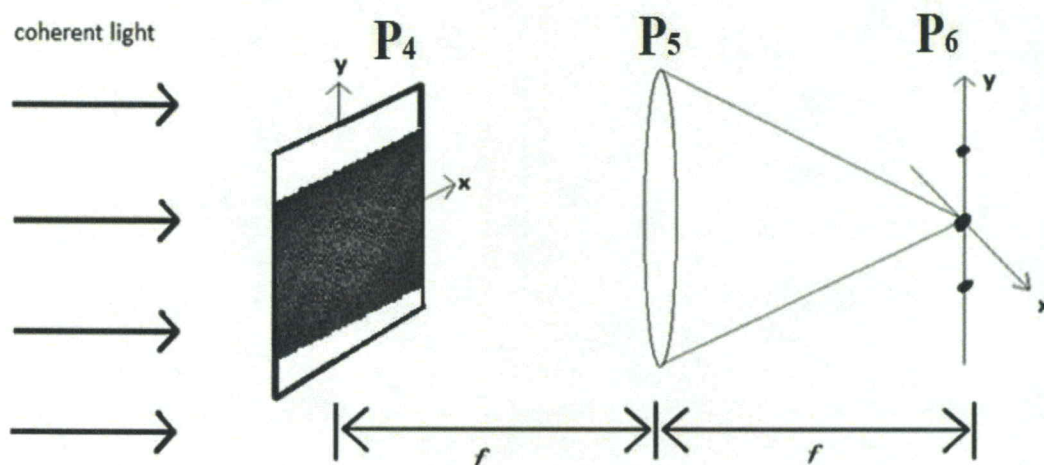
Figure 3.5: Second half of purely optical JTC. The new test scene (the joint transform pattern) is taken from the detector at P_3 and is the new test scene at P_4 being illuminated by coherent light which is then Fourier transformed by a lens at P_5. This is then imaged by a detector at P_6 and the magnitude square is taken. This results in the cross-correlation and DC term detected at P_6.

The BAMS software performs the Fourier transforms digitally, making the present JTC implementation more rugged and controllable. The JTC preserves the translation-invariant property of the Fourier transform, but the architecture has an inherent high-sensitivity to other factors such as scale and rotation [38]. The fact that the JTC is not rotation-invariant is useful for detecting the rotational alignment of the test image with respect to the reference image. The JTC also has a strong dependence on the illumination of (or light emitted by) the test object and the reference object. The joint transform correlation signal (I_J) will vary with the intensity ratio of the test scene (I_T) and reference scene (I_R) as described by the following equation:

$$I_J \propto \frac{\frac{I_R}{I_T}}{\left(\sqrt{\frac{I_R}{I_T}} + 1\right)^4} \tag{3.8}$$

This illustrates the importance of maintaining the ratio in the equation as close to unity as possible [39]. In the digital implementation presented here, the intensity (pixel values) of the reference (template) can be adjusted to closely match that of the live scene (target) captured by the camera. Another factor that can affect the performance of the JTC is an inherent nonlinearity in the system due to a flat, rather than curved, CCD sensor. If the test image wanders off axis, there will be an error present (analogous to curvature of field). With only small deviations being observed in the HEROES system, the error from this nonlinearity is minimal [40].

3.3 BAMS Software

The initial BAMS software was written by John Jasper, who made corrections to the BAMS software when required. BAMS analysis software was developed to digitally mimic the optical JTC technique described in section 3.2. A BAMS Graphical User Interface (GUI) was created, and a screen shot is shown in Figure 3.6. The black area outlined by a white box in the figure is the Area of Interest (AOI) and contains the optical Target Image (TI), which the user can also choose as a template (the reference image). The JTC uses the template and the TI to determine relative misalignment. The user can manually select a different template in the software and display the relative displacements of the TI in both arcminutes and millimeters. A history file is utilized so that the movement of the TI can be recorded.
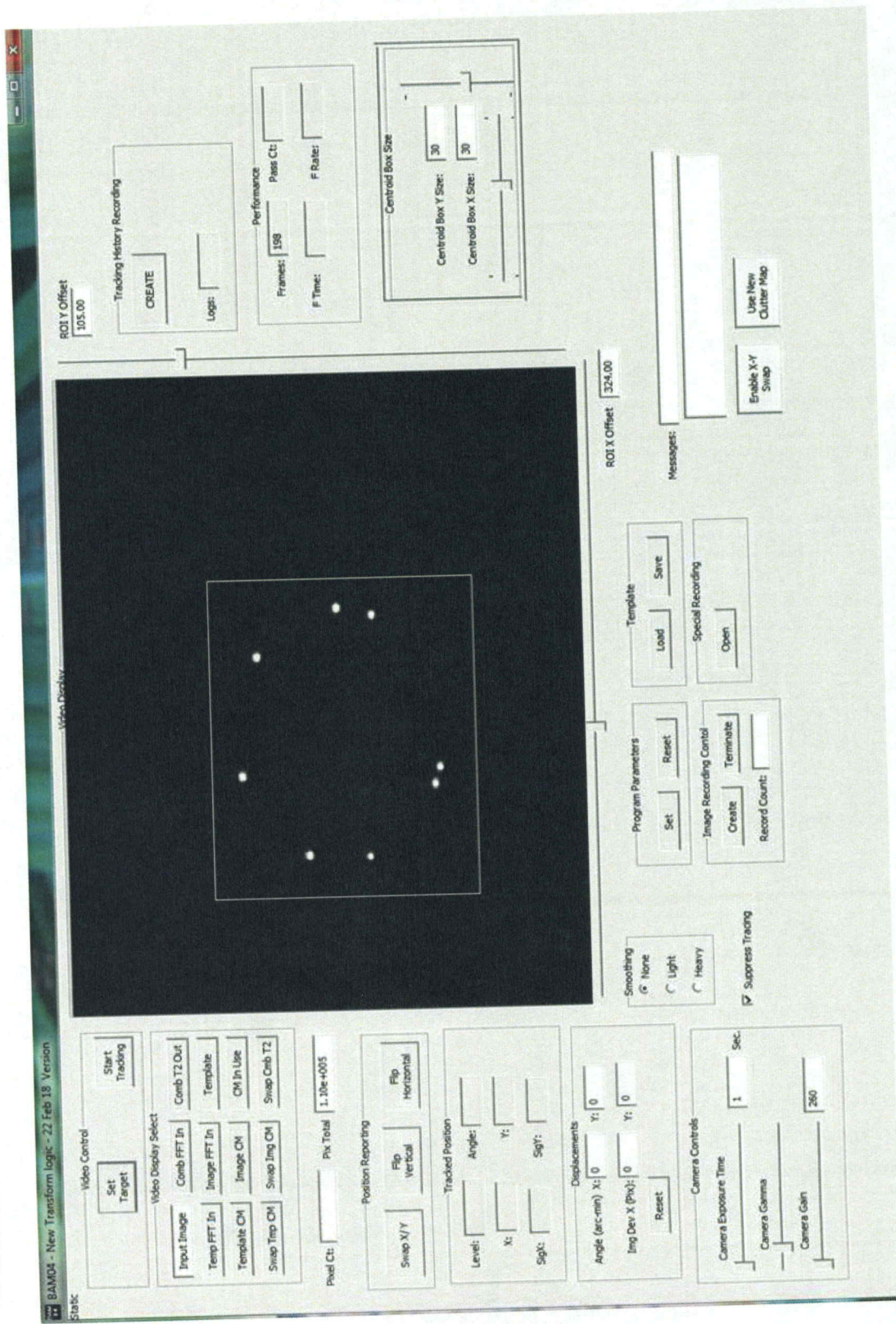
Figure 3.6: The BAMS Graphical User Interface with an LED ring target image displayed.

The operation of the software starts with a user selecting a video source, which can be a live IC camera, recorded video, or FITS file images. A window appears as in Figure 3.7 that allows the user to select which video source will be used.
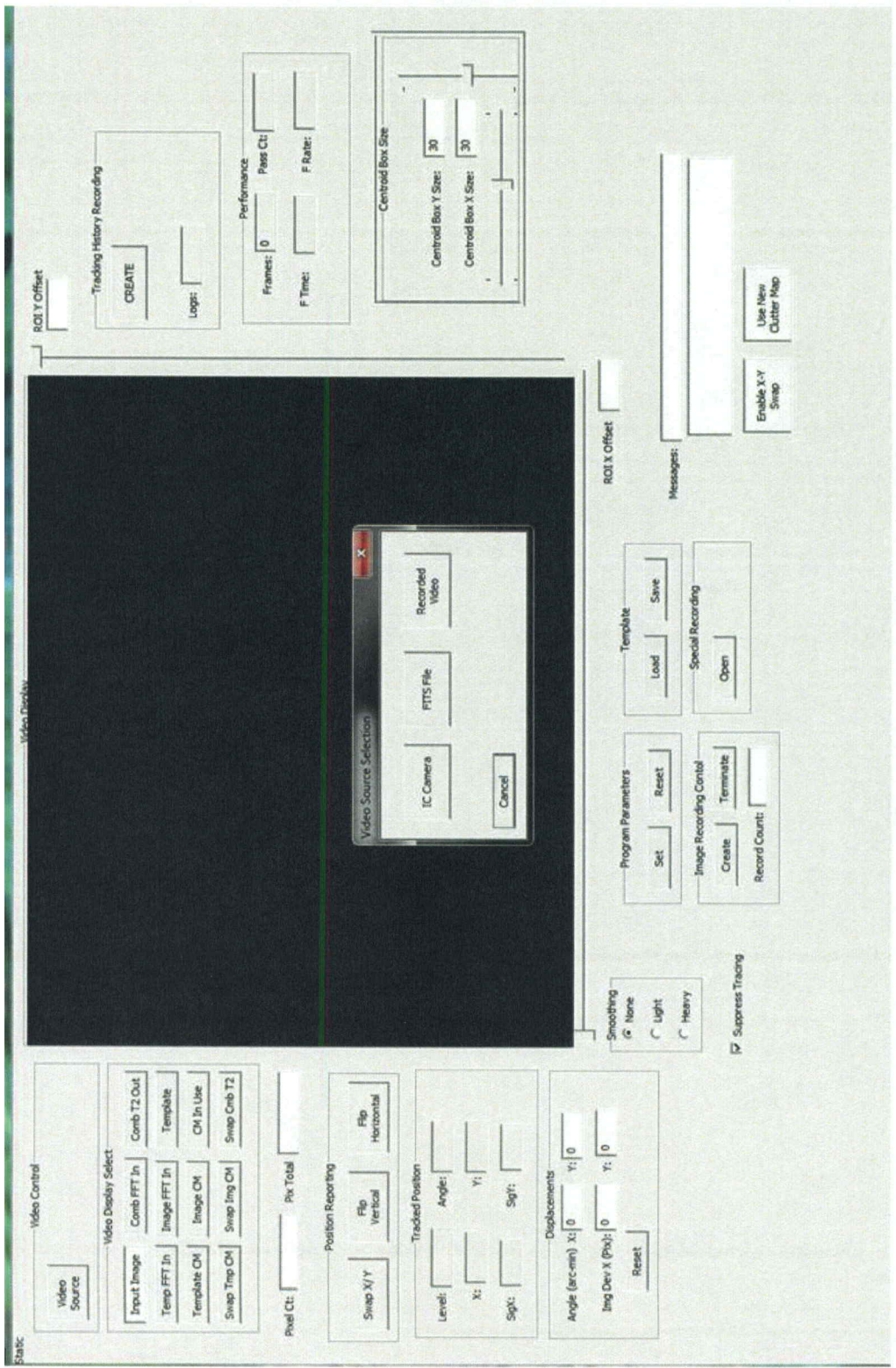
7: BAMS software video source select window which allows the user to select which urce is to be used.

When a FITS file is selected, another window seen in Figure 3.8 below appears and allows the user to select a folder with the FITS files that need to be processed. The user can select whether process "BAM Fwd" or "BAM Aft."
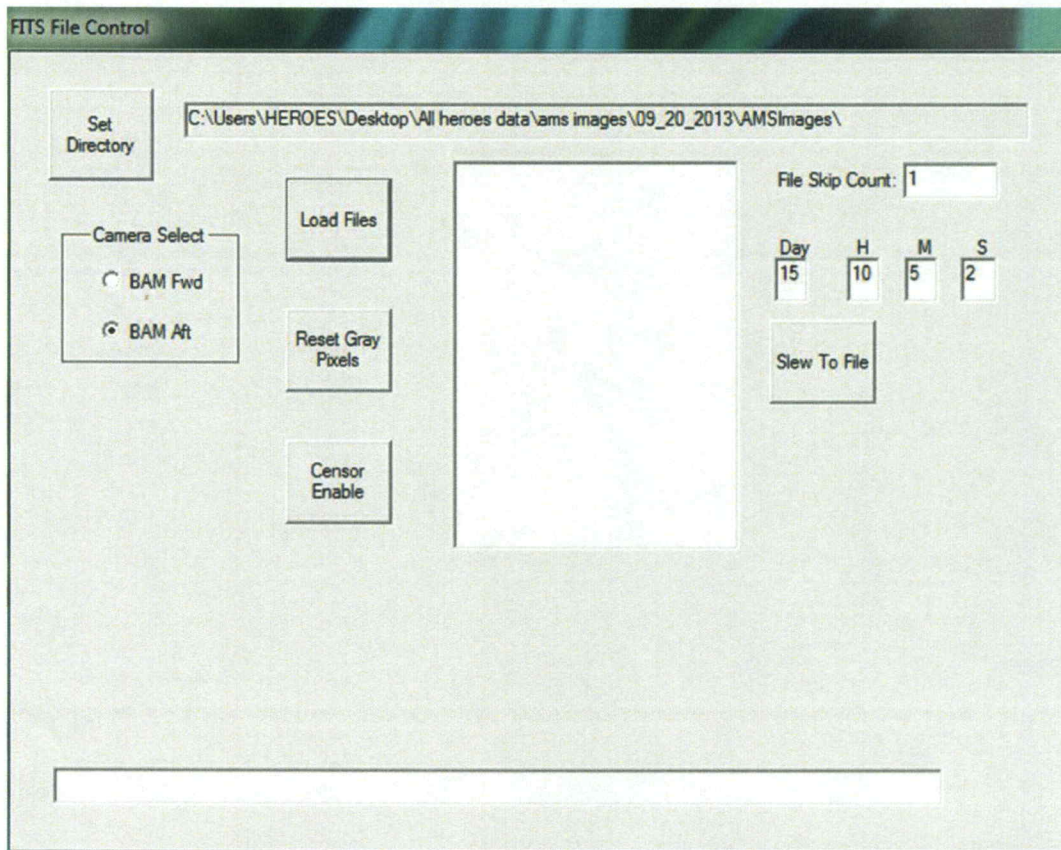
Figure 3.8: FITS file select window from the BAMS software.

Once the directory has been selected and the 'Load Files' button has been chosen, the BAMS FITS files in that folder will appear just as in Figure 3.9. The software allows for the files to be processed manually or they can be auto processed. There is an option to

edit out the region around the target. This can be used to zero out any stray light that may

appear outside the area of interest.
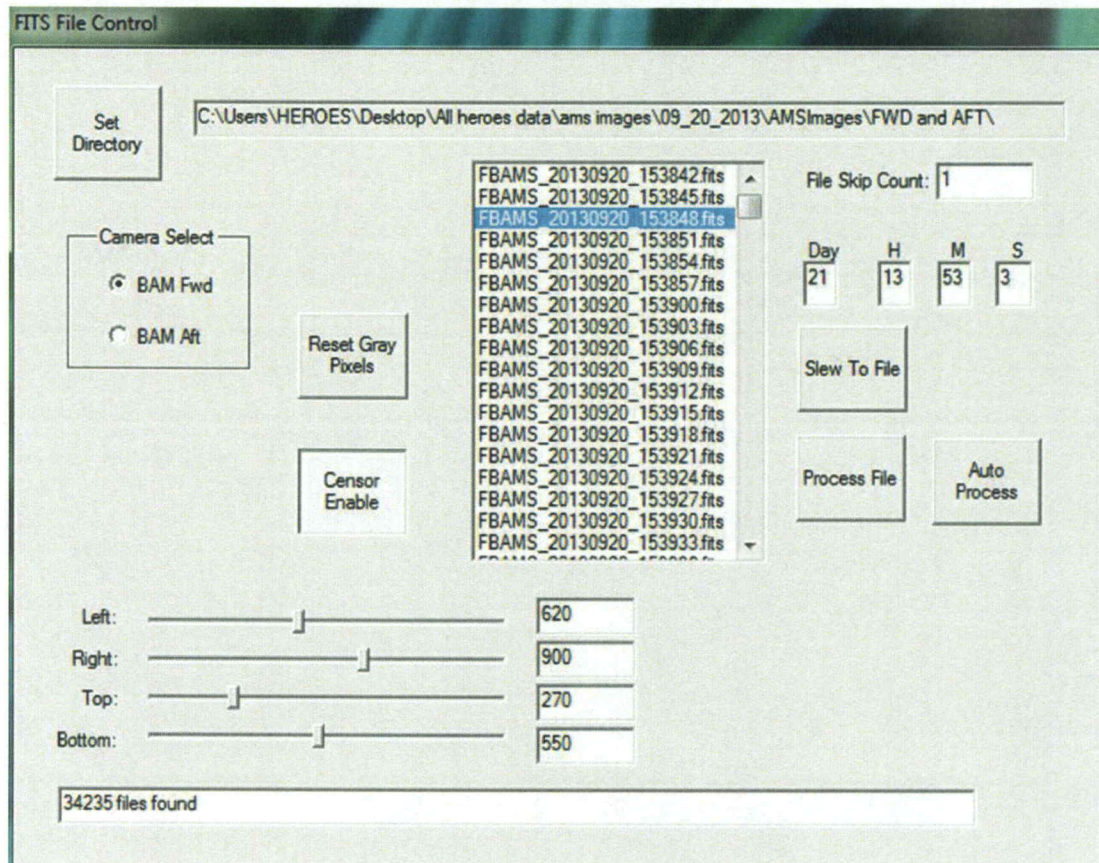
Figure 3.9: FITS image window with the FITS file folder selected and all the files from the folder loaded. Once loaded several options appear such as "Process File", "Auto Process" and "Censor Enable".

Once the video source has been selected and the 'Start Tracking' button has been

chosen, the software will switch to the screen seen in Figure 3.10. After tracking has been

initiated, the displacement values will update for each processed image.
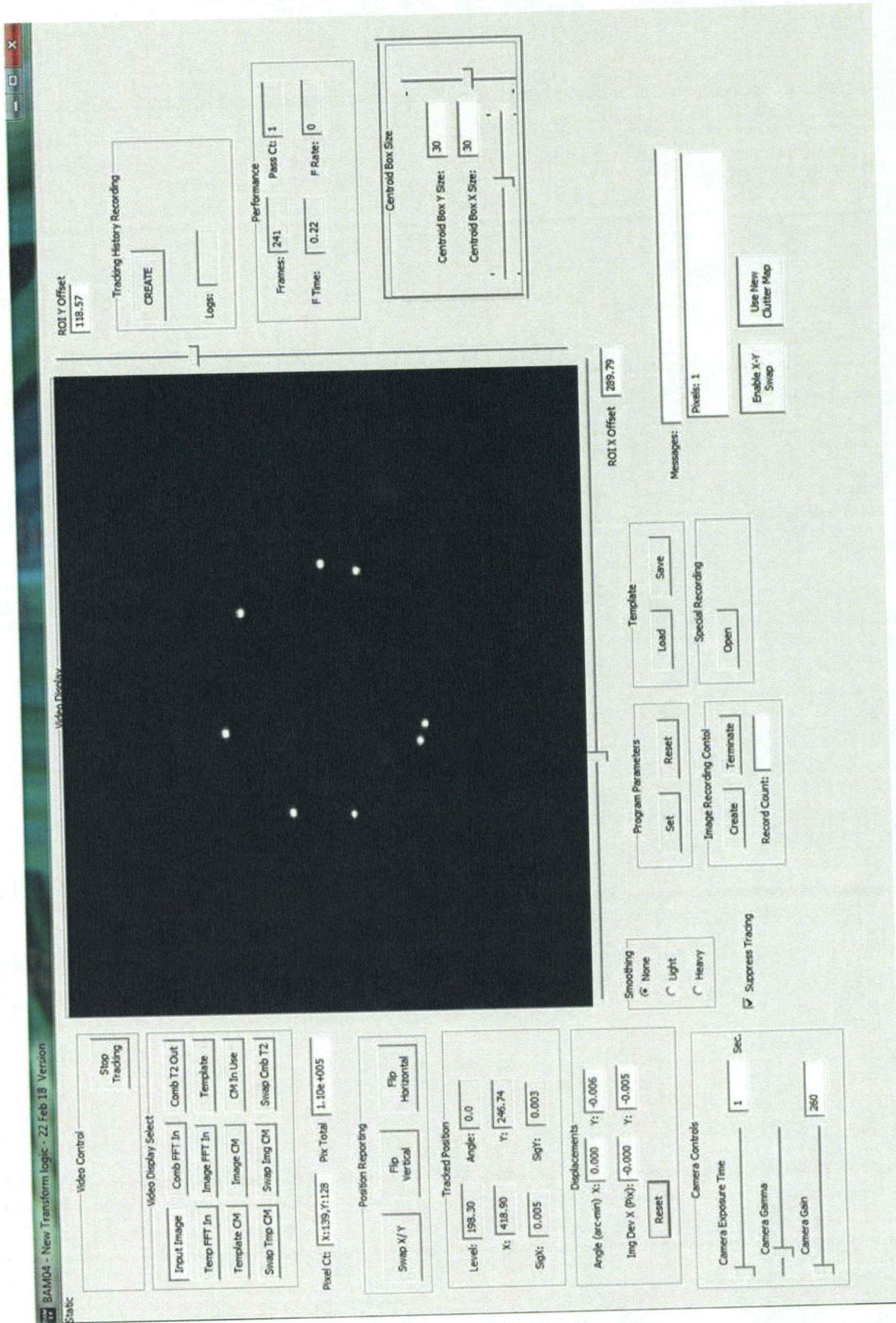
Figure 3.10: BAMS software once start tracking has been clicked by the user.

Figure 3.11 shows the clutter map which corresponds to the autocorrelations of each ring with itself. A clutter map is made for each of the LED rings and is simply the autocorrelation of each of the rings. This is done so that the autocorrelations can be removed from the final JTC. The clutter map is subtracted from the second transform of the two rings which only leaves the cross-correlation of the two rings.
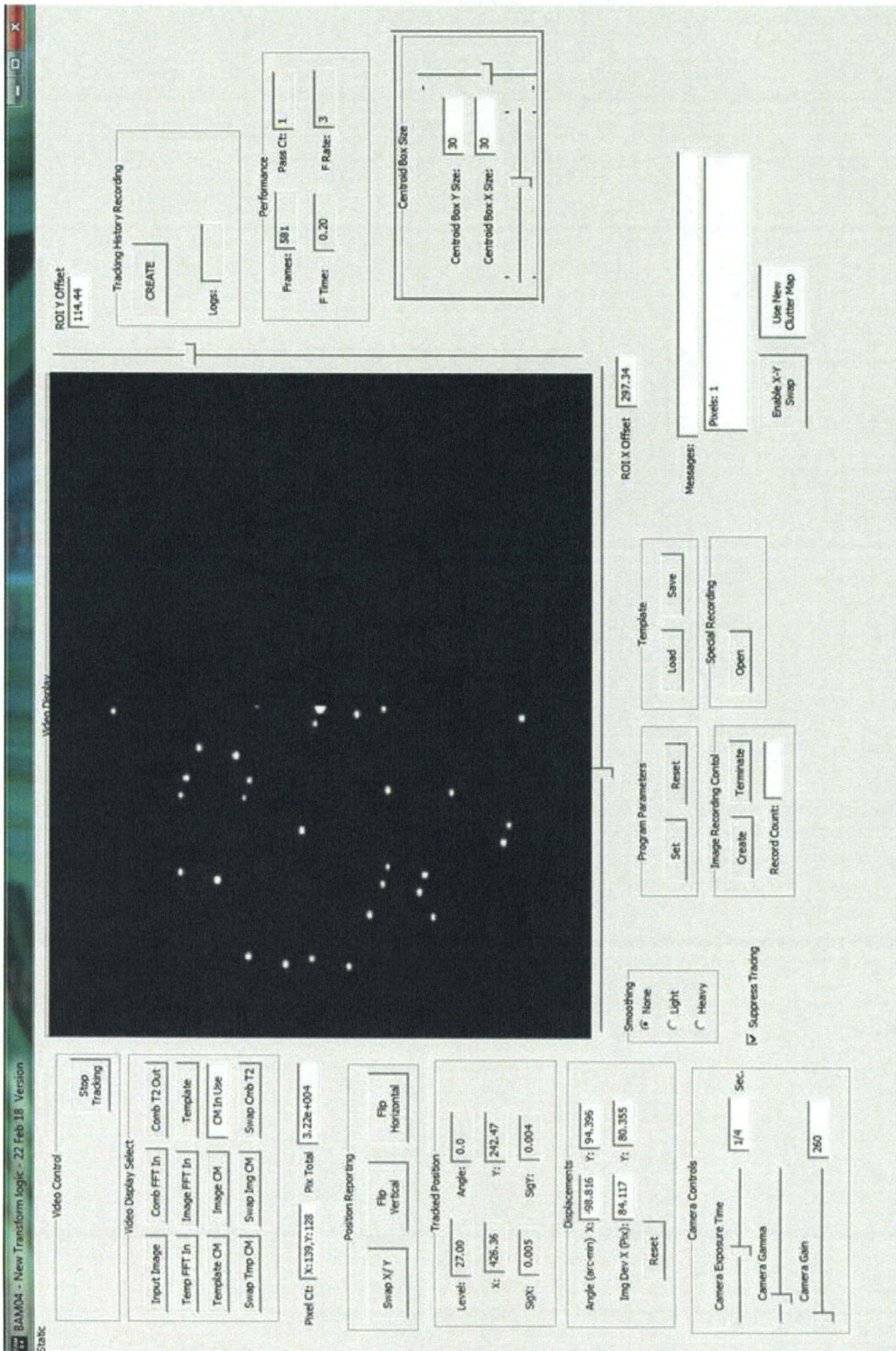
Figure 3.11: Image of the clutter map from the BAMS software. This is a combination of the autocorrelations of the two rings.

The JTC software includes, besides two Fast Fourier Transforms (FFTs), other pixel-level processes which can be run with the parallel processing capabilities offered by an NVidia Graphics Processing Unit (GPU) [41]. This parallel processing capability drastically decreases the processing time for each image. A flow chart of the correlation operation as implemented in the GPU is shown in Figure 3.12 and is described below.
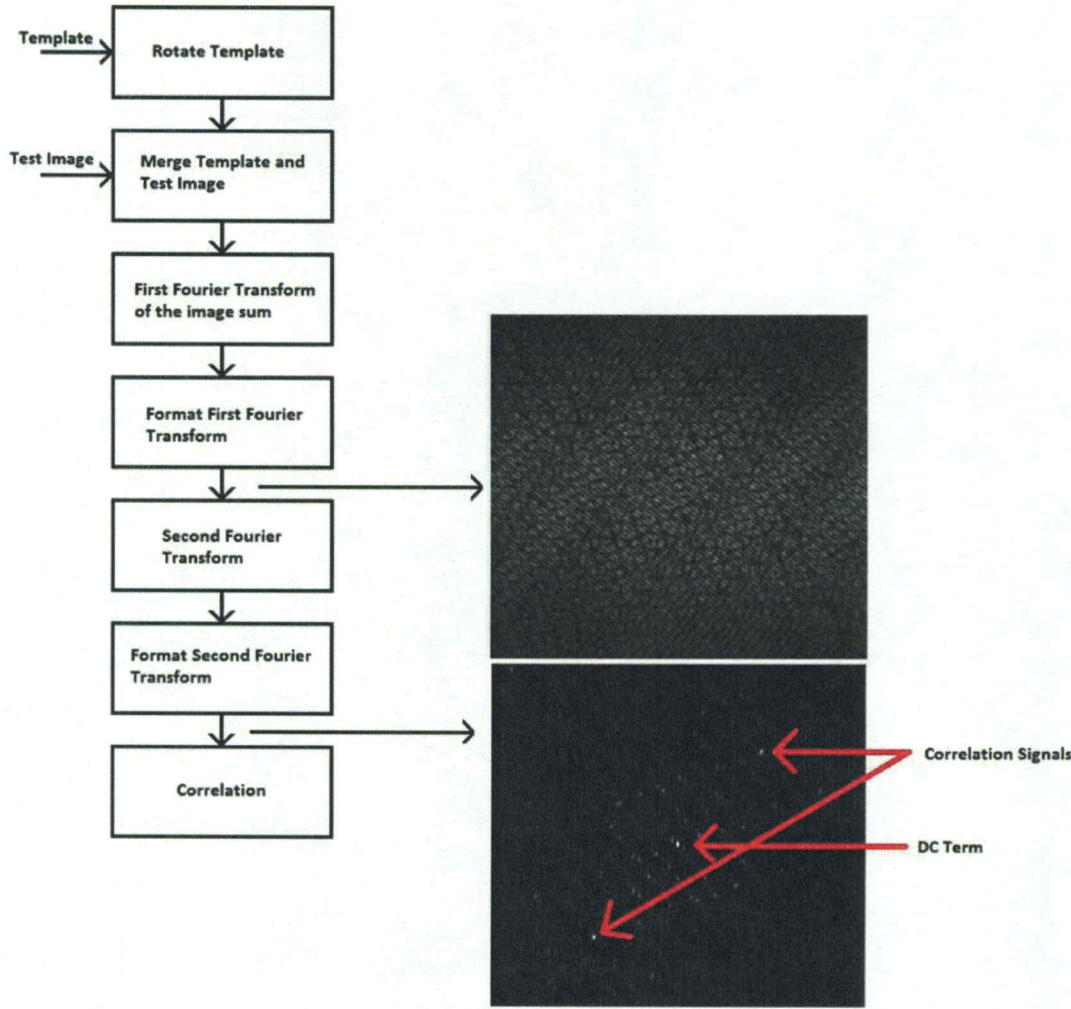
Figure 3.12: Flow chart GPU implementation of the correlation operation.

A static copy of the reference image of interest (the Template) is introduced into the GPU then merged into the current camera scene that contains the TI by means of an operation. The pixels of the Template (after rotation) are merged with the current camera scene and the resulting pair of images is Fourier transformed using commercial off-the-shelf software known as the Fastest Fourier Transform in the West (FFTW), which is available from NVidia [42]. The results of the transform are manipulated so that the low spatial frequencies are in the center of the transform rather than at the corners where the FFTW leaves them. This change has no effect on the results of the software but is done due to legacy operations of the software which are too time consuming to change and this provides a visual confirmation of the structure of the transform. The results of a typical first transform can be seen in the topmost image given in Figure 3.12. In this image, interference fringes (or rather their digital analog) can be seen. After testing the JTC in matlab it was discovered that using the real to complex FFTW was not producing the correct results. For the first transform, the complex to complex FFTW and not the real to complex FFTW must be used due to the fact that the result of the first transform is not Hermetian. The real to complex FFTW only produces half of a transform [44].

The result of the first complex (joint) transform is then Fourier transformed and the result of the second transform is formatted to ensure that the low spatial frequencies are again in the center of the transform. The reformatted result of the second transform consists of three groups of bright pixels (typically the brightest pixels in the transform) surrounded by pixels of lower amplitude such as shown in the lower image in Figure 3.12. One of the identical (off-axis) cross-correlations, after suitable filtering, is used to determine alignment of the two scenes. The unused on-axis (DC) bright pixels

correspond to autocorrelations. A 3D map of a typical cross-correlation is shown in Figure 3.13.
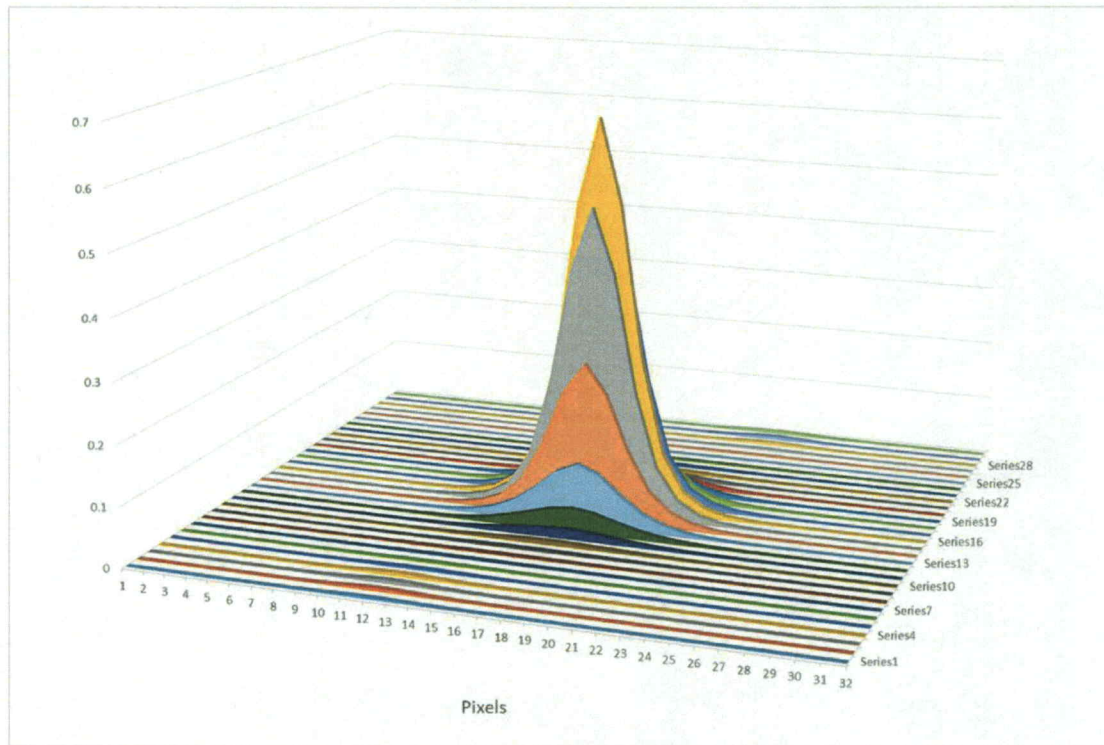
Figure 3.13: Cross-correlation obtained for a single HEROES LED ring.

The BAMS software uses the correlation procedure described above for both angle and linear X-Y alignment. When the Template and the TI approach angular alignment, the grey scale value of the correlation peak increases. This angular alignment approach can be done because only scale and rotation can decrease the signal and here the scale is fixed. The distance between the Template and the TI determines the relative separation between the Template (reference) and the target. As the the distance between

the two goes to zero, the correlation will move to the center of the second transform. The

flow diagram for this process is shown in Figure 3.14.
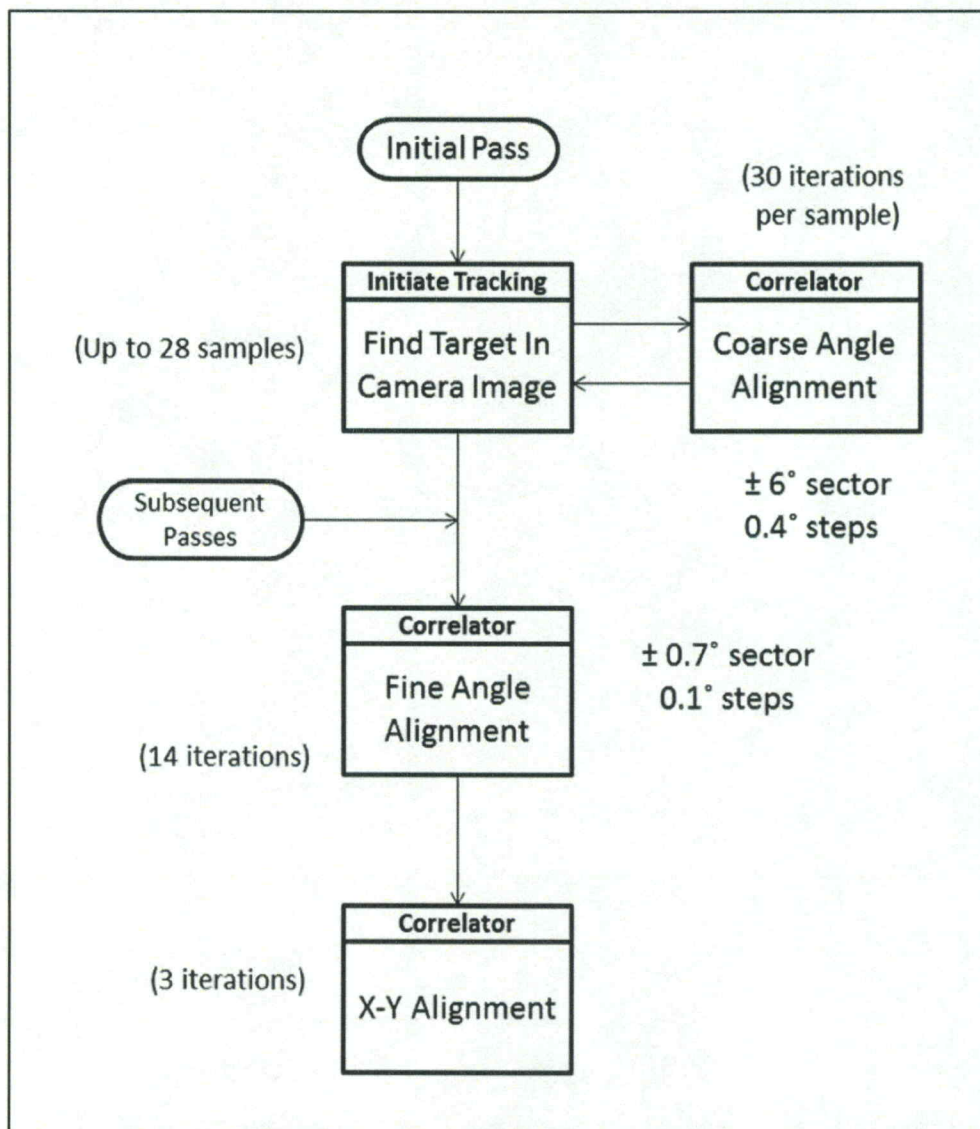
Figure 3.14: BAMS procedure for finding the second transform correlation signal (relative) angle and position.

The BAMS program is designed to measure differential deviations referenced to

an initial alignment. When the BAMS program is initiated, the initial pass searches for

the TI within the camera frame, sampling overlapping areas 512 pixels square. The initial

pass will search the entire CCD array for the target. For each sampling region, the

correlation operation is excuted for a series of rotation angle steps, with the rotation angle

sector step having the brightest pixel being saved. The initial Tracking function

determines both the 512 pixel square portion of the camera image containing the TI and

the user determined coarse (typically ± 0.4 degrees) rotation angle.

Once the location and the coarse rotation angle of the TI is known, BAMS

performs a fine angle alignment, rotating the Template in 0.1 degree steps. The changes

in pixel amplitude as the Template is rotated in these small steps, yielding a TI angle with

an precision on the order of ±0.1 degrees.

X-Y Alignment is performed by moving the AOI to obtain a precise separation

between the Template and the TI in both the X and Y directions. The algorithm does not

attempt to superimpose the Template onto the target image. The system is unable to

determine whether the TI is to the right or the left of the Template, so two executions of

the program are required to determine the polarity of the separation in the X direction.

The offset between the Template and the TI in the Y direction is also determined at this

time.

Finally, the JTC operation is executed once more, and the centroid of the

correlation function is determined. The centroid positions $\hat{x}_c$ and $\hat{y}_c$ are calculated using

the following equations:

$$\hat{x}_c = \frac{\Sigma_{m,n} x_{mn} I_{mn}}{\Sigma_{mn} I_{mn}} \tag{3.9}$$

$$\hat{y}_c = \frac{\Sigma_{m,n} y_{mn} I_{mn}}{\Sigma_{mn} I_{mn}} \tag{3.10}$$

62

Where I_{mn} is the grey scale value of the pixel at the corresponding x and y positions on the CCD [43]. The correlation signal in the second transform extends over several pixels, so the computed centroid of the signal yields a "center of mass" pixel position. The results for the second transform are squared, so that the central peaks will contribute much more to the centroid and any small fluctuations will not significantly add to the reported position. This position is not reported in integer pixels but rather in fractions of a pixel (of the correct position) which is the subpixel resolution referred to earlier. By comparing the rotation angle and correlation centroid position with the rotation angle and correlation centroid saved as a baseline, a precise deviation in both angle and position of the TI is obtained.

3.4 Chapter Summary

BAMS was a system designed specifically for the HEROES flight mission. The system consisted of two cameras mounted on the elevation flange that monitor LED rings attached to the optics flange, three optics modules and the detector flange. The BAMS software operates by applying the purely optical JTC in digital form so that alignment of the LED rings could be monitored and provide accurate misalignment information post flight. The software uses a test scene comprised of a reference ring and a test ring to track movement between the two. The JTC is calculated using NVidia's GPU processing capability which allows for faster processing of images compared to conventional means. The JTC produces a cross-correlation spot which is monitored for movement to provide misalignment information. The cross-correlation spot is then centroided to provide subpixel alignment information.

Chapter 4

Preflight Testing and Results

4.1 MATLAB Simulations and BAMS Software Development and Debugging

The BAMS benchtop testing described in Chapter 3 is discussed in detail in this chapter. Experimental benchtop tests were performed to ensure that the software operated as intended. These tests include MATLAB simulations that were done to evaluate the second Fourier transform (cross-correlation) for an LED ring target.

4.1.1 MATLAB Simulations of BAMS

MATLAB simulations of the JTC were executed to predict/confirm the correct second Fourier transform (cross-correlation signal) for an LED ring target. The simulation used a replica composite scene identical to the one intended for use during the HEROES flight. The composite scene consisted of two LED rings separated by a predetermined, calculated distance, which ensured the cross-correlation signal would not overlap the autocorrelation signal of the rings (Figure 4.1). The two LED rings were created with an image capture of a single LED ring. The final composite scene image was therefore two copies of this ring summed into a single image.

64
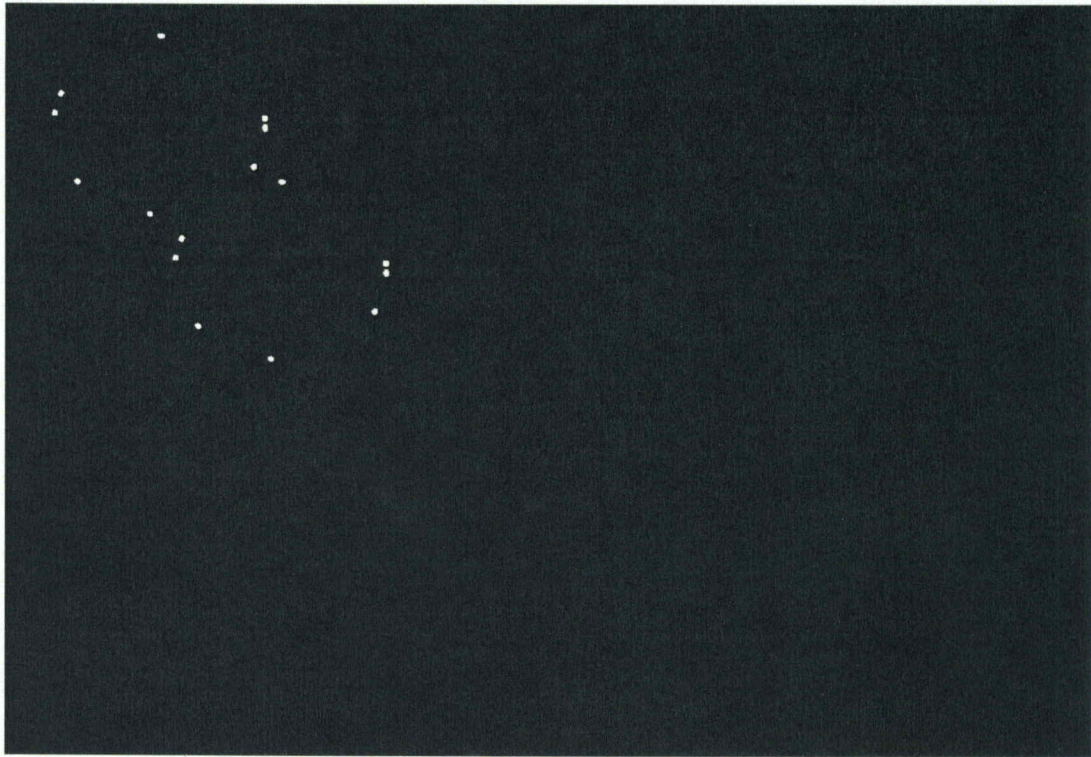
Figure 4.1: Composite scene comprised of two LED rings to be used in MATLAB simulation.

The composite scene image was imported into MATLAB for processing by the MATLAB software then Fourier transformed using the built-in Fast Fourier Transform (FFT) function. The magnitude squared of the result was used to simulate the JTC by producing an image with only real terms (Figure 4.2). The result of the first Fourier transform was recursively set as the new scene to be processed in the next step of the JTC.
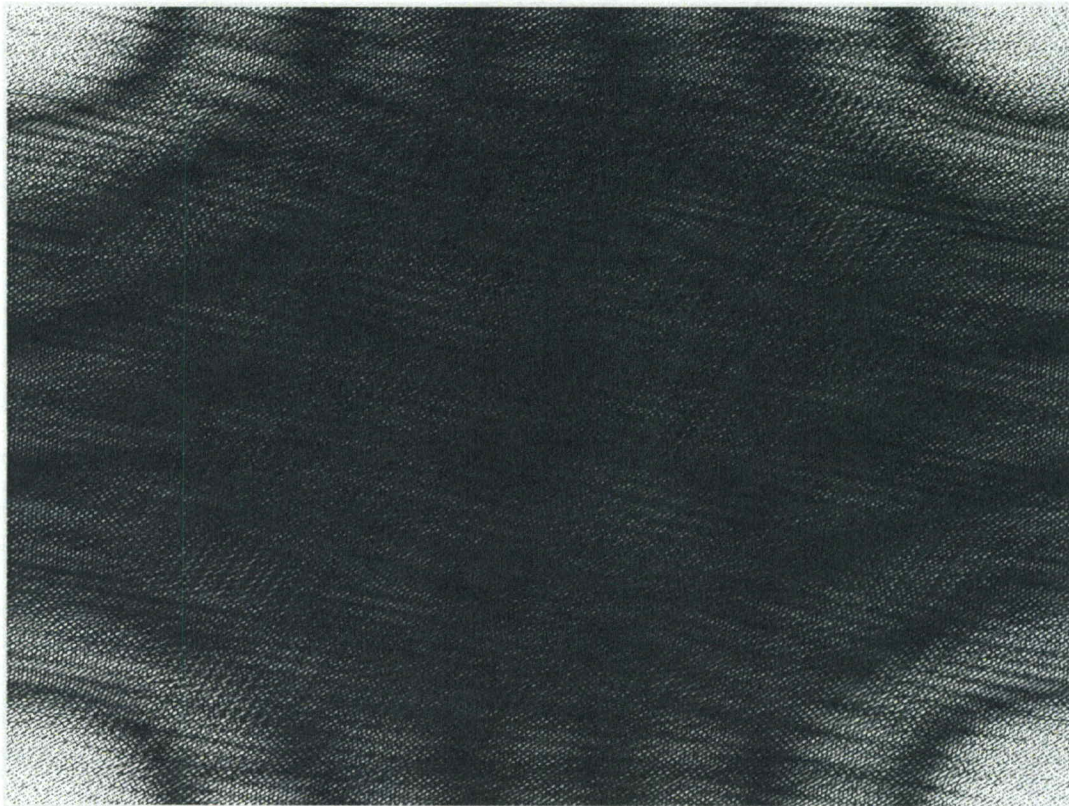
Figure 4.2: MATLAB produced result of the first Fourier transform of the composite scene (magnitude squared), which recursively becomes the new scene used in the next part of the JTC.

The new scene was then processed in the same way to produce the second Fourier transform (cross-correlation) result of the JTC. In an optical JTC system the DC term (autocorrelation) of the reference LED ring and the object is found in the center of the image, but due to the nature of the Nvidia FFT, the DC term is placed in the corner of the image [19]. The new placement of the DC term did not affect the results of the BAMS system. The result shown in Figure 4.3 is significantly different from the second transform originally produced by BAMS, which indicated an error had occurred in the BAMS software code.

66
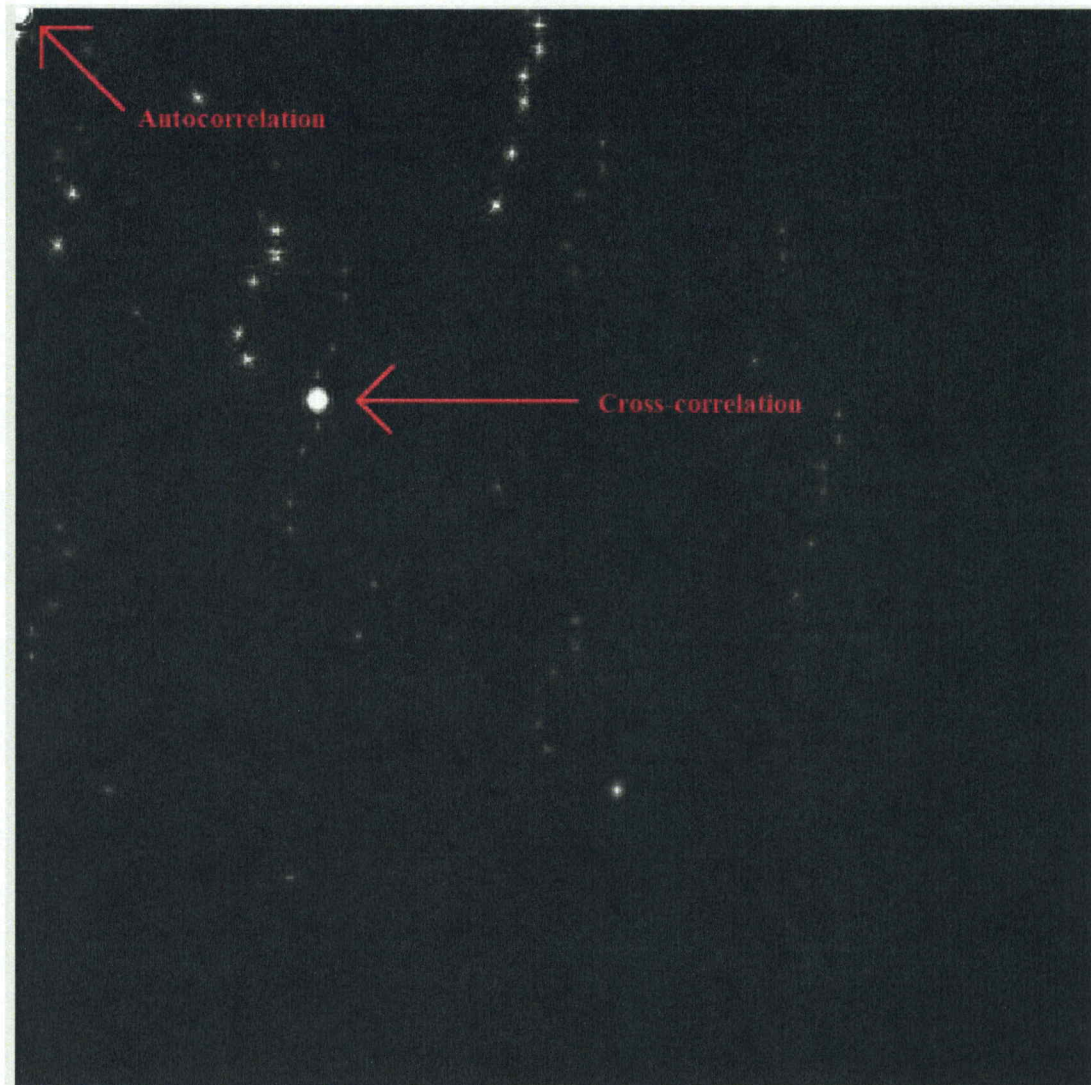
Figure 4.3: MATLAB image of the final correlation signal plane after the last Fourier transform. In this simulation the Complex-to-Complex (C2C) FFT was used for the first Fourier transform which provided a full FFT unlike the Real-to-Complex FFT which only provided a half transform. The bright spot in the upper left corner is the autocorrelation (DC term) and the other bright spot is the cross-correlation signal of the reference and object. The small dim spots around the LED ring cross-correlation signal are due to cross-correlations of the individual LEDs both inside each LED ring and for the opposing ring.

The C2C simulation produced a final result that was much different from the second transform produced by the BAMS software. This was due to BAMS's use of the Nvidia Real-to-Complex (R2C) Fast Fourier Transform (FFT). The R2C FFT produces only half of the transform, unlike the previously discussed Complex-to-Complex (C2C) FFT (see Chapter 3) that produces a full transform. The R2C FFT was executed in BAMS originally under the assumption that the result of the first transform was Hermitian, so only half of the matrix needed to be produced. The two halves would be identical. This, however, was not the case for the BAMS results; the first transform matrix was not Hermitian, so the software suffered a loss of half the data from the first transform. The asymmetry in the FFT is attributed to the Nvidia software's approximation technique for Fourier transform calculations. A MATLAB simulation that enlisted the R2C FFT for the first Fourier transform yielded identical results to those seen in the original BAMS software (Figure 4.4) [44].
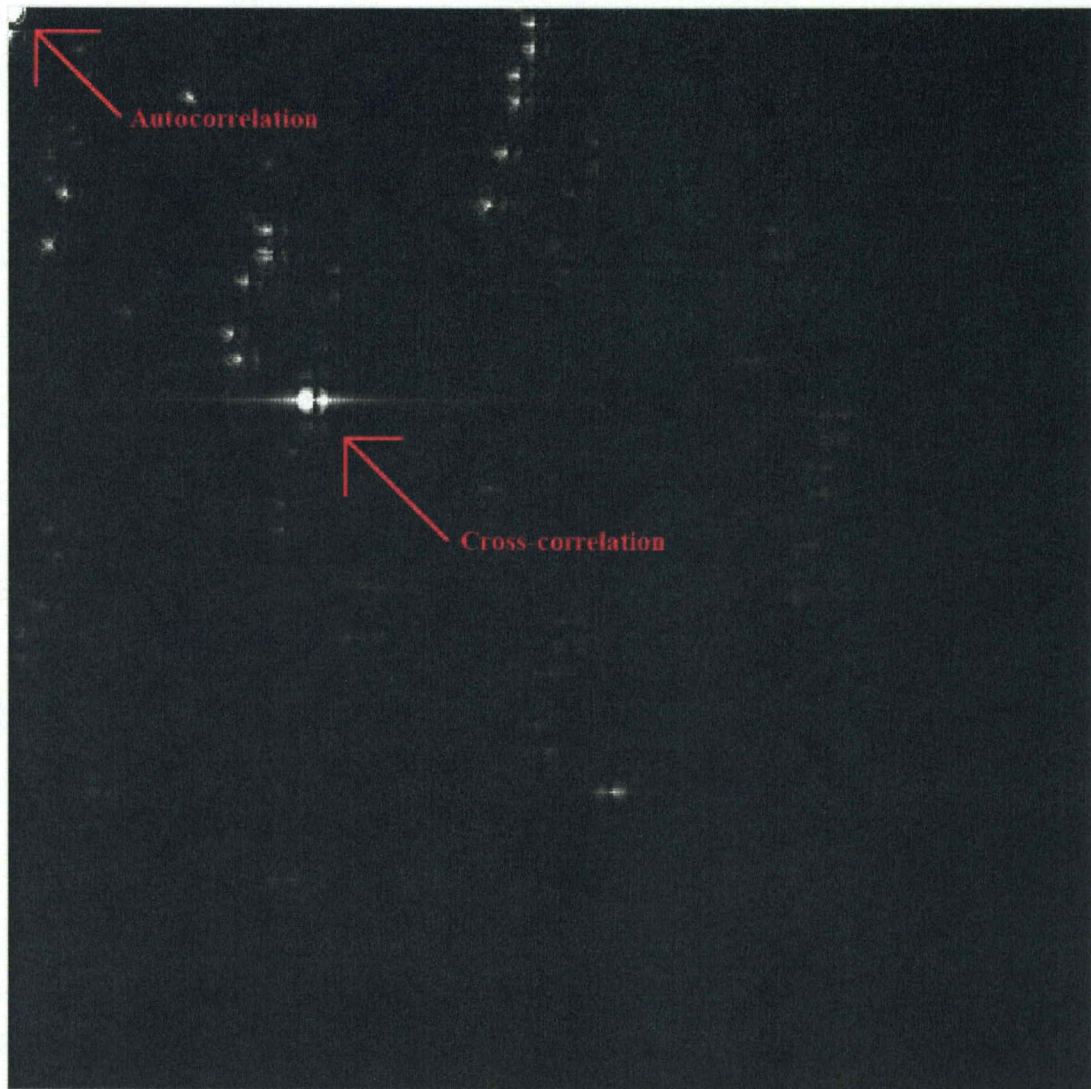
Figure 4.4: MATLAB image plot of the end result for the composite scene shown in Figure 1 after the JTC process had been applied. This result was replicated using the R2C FFT used in the BAMS software for the first Fourier transform. The bright spot in the corner is the autocorrelation (DC term) while the other bright spot is the cross-correlation signal of the reference and object LED rings. The cross-correlation has an extraneous bright line on either side of the signal that is not in the C2C FFT simulation.

Since BAMS's use of the R2C FFT did not produce perfectly correct results for the JTC, a new FFTW function was implemented. Research into the Nvidia cuFFT toolkit documentation yielded that it was best to use the Complex-to-Complex (C2C) FFT, for the return of a full transform [44]. After implementation of the C2C into the BAMS software was completed, the BAMS results for the JTC matched the results of the C2C MATLAB simulation, confirming BAMS was ready for benchtop testing.

4.1.2 BAMS Software Development and Debugging

BAMS software has evolved from a previous version, written and designed by John Jasper, an independent contractor of K-Sciences of Huntsville that employed the use of the JTC as a star tracker. Mr. Jasper was added to the HEROES team to assist in further development of the BAMS software as a contractor through the University of Alabama in Huntsville (UAH).

Benchtop tests were performed to ensure the software operated as intended using a prototype LED ring set up in a long inner hallway at UAH. The benchtop test used a camera and laser mounted on a manual rotation stage that was attached to a tripod 3 m away from a prototype LED ring (Figure 4.5). The camera was mounted such that it could observe the LED ring. Simultaneously, the laser propagated 130 ft down to the opposite end of the hallway onto a sheet of one inch grid paper (Figure 4.6).

70
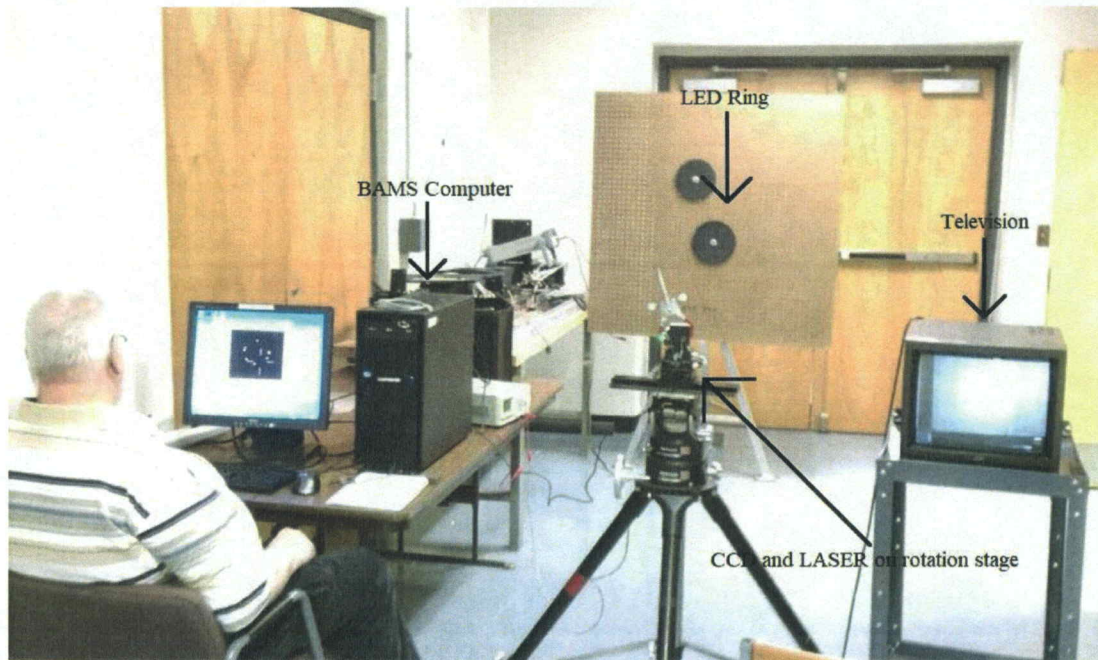
Figure 4.5: BAMS benchtop test setup at UAH with prototype LED rings and tripod mounted with laser and camera. The television used to watch the laser move on the grid paper is positioned on a cart to the right of the tripod. John Jasper is pictured sitting at the computer ready to make changes to the software if needed.

The grid paper was observed by a second camera connected (via a long BNC cable) to a monitor positioned next to the computer with the BAMS software installed. The initial experimental test involved rotating the stage. Doing so allowed the laser spot to be translated across the grid paper in 1 inch steps (which equated to 2.2 arcminute movements of the camera). This translation exercise was to confirm that the software could easily track the laser position on the paper. The test was repeated dozens of times during the debugging process. Further benchtop tests were completed using motorized stages that provided much more accurate movement of the LED ring. This is discussed in further detail in Section 4.2.
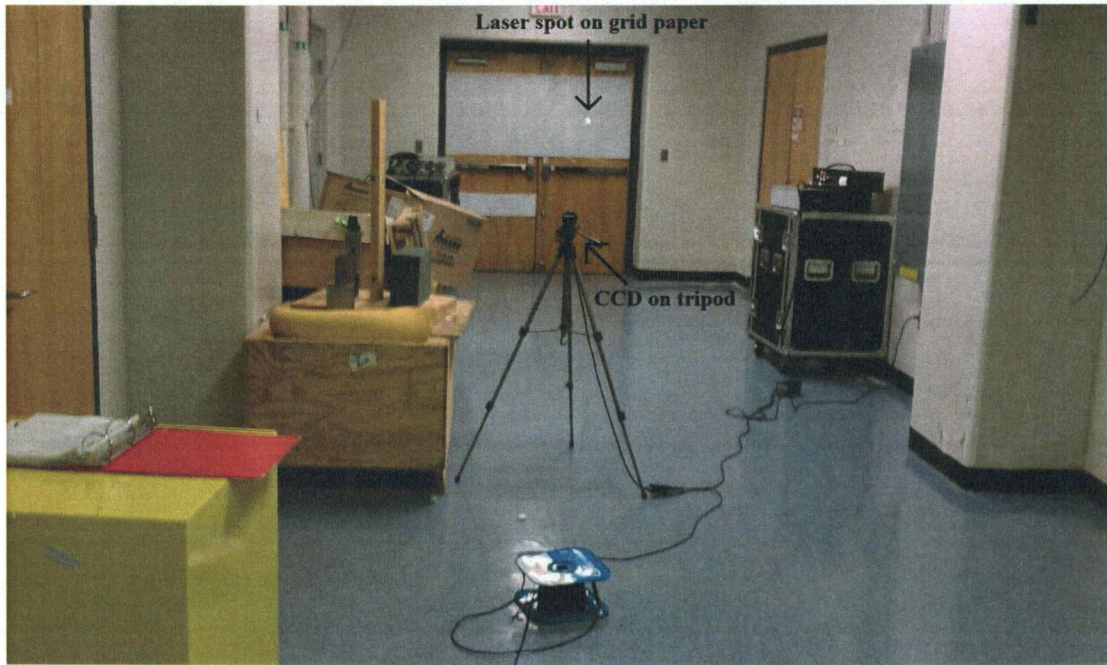
Figure 4.6: Image of the CCD camera used to monitor the laser spot on the grid paper during BAMS initial benchtop testing at UAH. The cable spool seen behind the camera was a BNC cable that connected to the monitor positioned next to the BAMS computer at the other end of the hallway.

4.2 BAMS Benchtop Testing and Analysis

The BAMS software was validated experimentally in a controlled laboratory environment prior to the HEROES launch. All of the BAMS tests were performed on an air supported table to further characterize the error present in the BAMS hardware and software. The systematic error that could potentially affect the BAMS flight results was calculated for different components of the hardware and software. The following sections provide the results of these tests.

4.2.1 LED Scale Invariance of the JTC

During balloon flights, payloads can experience temperatures as low as -40 Celsius; such temperatures can alter the current through the ring's LEDs and therefore change the optical intensity. If the intensity increases, the apparent size of the LED as seen by the CCD also increases [45]. This directly proportional relationship results in an increased correlation spot size, which potentially adversely affects the precision of the BAMS recorded position.

The voltage to the test LED ring was incrementally increased from 8.6 V to 11.80 V in steps of 0.4 V, which resulted in an increased apparent size of each LED as detected by the camera. A nominal voltage of 8.6 V was considered the 'zero-point' against which higher voltage apparent LED spot sizes were compared. Typical LED spot size changes seen in the HEROES flight BAMS images correspond to a fluctuation of 0.4 volts, which is equivalent to a change in position of less than .005 arcminutes (Table 4.1).

Table 4.1: Change in BAMS displacement data with increasing LED voltage. The position as a function of voltage in step sizes of 0.4 V up to 11.80 V was recorded. BAMS tracking was started and "zeroed" at 8.60 V. As the voltage increased, the spot size of the LEDs as seen by the CCD increased in diameter.

Voltage (volts)	BAMS Recorded X Position (arcminute)	BAMS Recorded Y Position (arcminute)
8.60	0.002	0.001
9.00	0.002	0.004
9.40	0.030	-0.028
9.80	0.060	-0.061
10.20	0.130	-0.102
10.60	0.205	-0.152
11.00	0.280	-0.185
11.40	0.370	-0.205
11.80	1.345	-0.205

4.2.2 LED Stability

Slight variations in the LED intensity over time naturally occur due to changes in temperature, which could be another source of error in the BAMS software recorded position [46]. To test this source of error, the LEDs' optical power output was recorded over a period of approximately 14.5 hours while the displacement data produced by BAMS was recorded. The LEDs' output did fluctuate slowly over time, causing the BAMS alignment position to vary between +/- .01 arcminutes for the majority of the test period. This is shown in Figure 4.7. The standard deviation for this stability test data is 0.005 arcminutes.
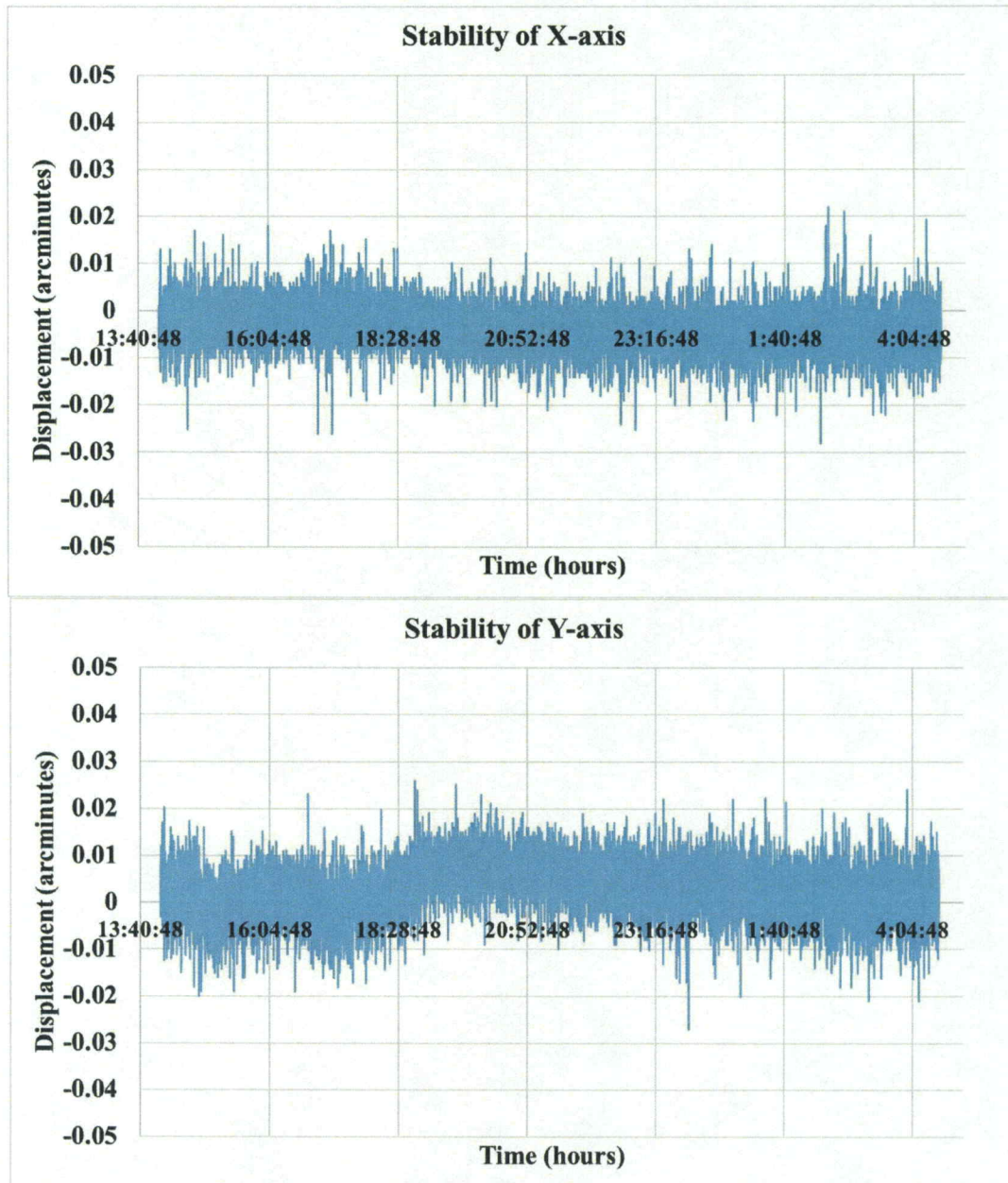
Figure 4.7: LED stability test data for the X-axis and Y-axis over a period of 14.5 hours. The environmental conditions were regulated to ensure no temperature fluctuations. The hardware was also positioned on an air supported table to minimize vibrations. The BAMS position data was zeroed at the beginning of the test immediately before recording began.

4.2.3 Linear Displacement

Benchtop tests were performed to determine BAMS's ability to report accurate displacement information. Tests involving controlled linear movement of an LED ring were carried out using BAMS to independently determine displacement (Figure 4.8). A CCD camera (the same model used on the HEROES payload) was mounted on an optical mount 120.453 +/- .25 inches away from the LED ring. The ring was moved using a Newport (model esp301) motion controller stage with a motorized linear actuator in steps of 0.890 mm (1 arcminute).
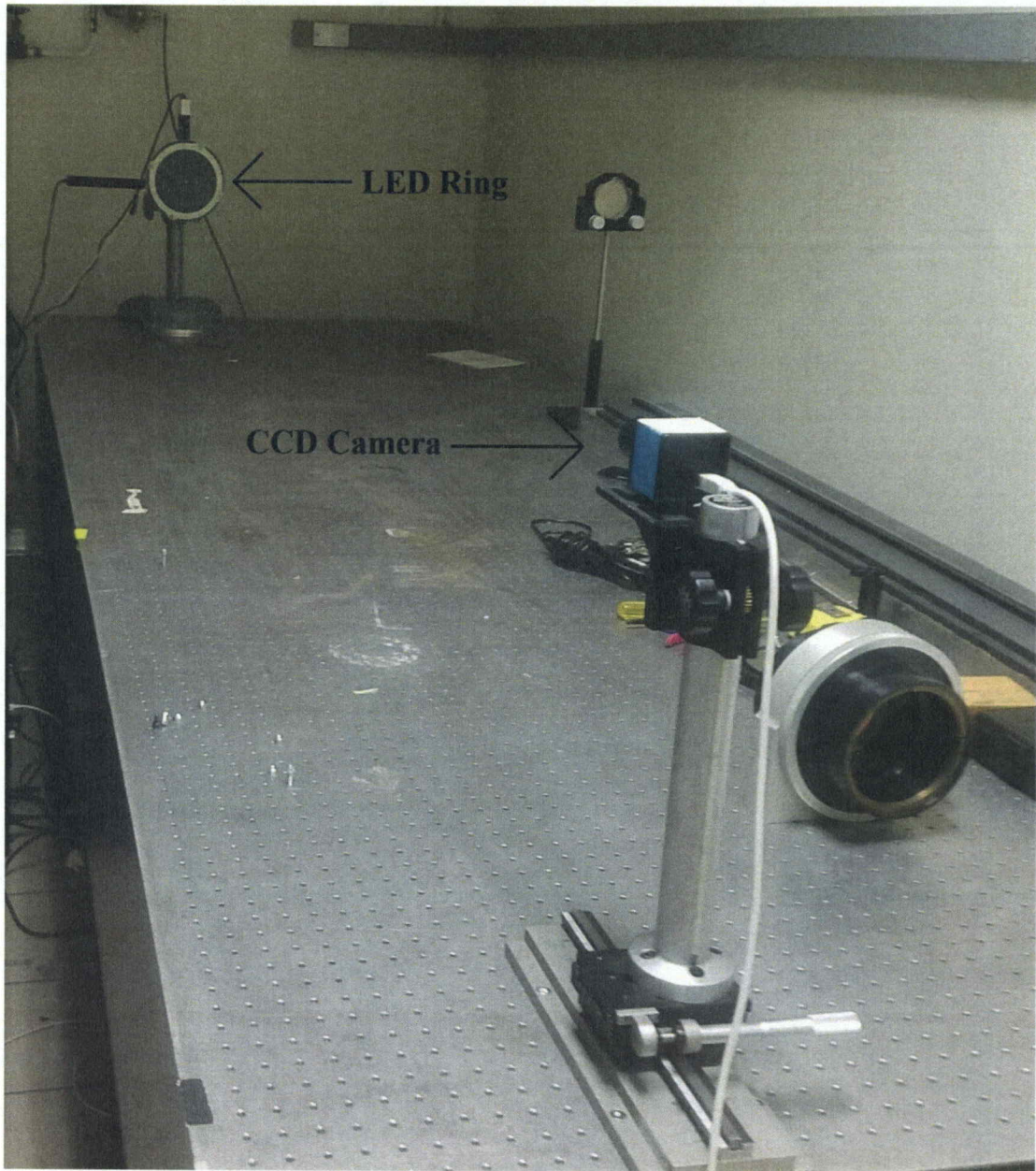
Figure 4.8: BAMS benchtop setup on an air supported table at the MSFC. The CCD camera is on one end of the table while the LED ring was mounted on a translation stage at the other end of the table.

The BAMS reported displacement position of the LED ring for each movement of the linear stage was recorded and then compared to the linear actuator displacement position. The BAMS software outputs for each LED ring position and position error, measured in values for X-axis and Y-axis movement, were recorded and are shown in Table 4.2 and Table 4.3.

Table 4.2: BAMS results for LED ring movement on the motorized linear displacement stage for a movement in the X-axis. The LED ring was moved in increments of 0.8900 mm in the X-axis which equated to 1 arcminute steps.

X-axis position on stage (mm)	Intended X-axis position (arcminute)	X-axis displacement (arcminute)	Difference between intended position and actual position (arcminute)
0.0000	+0.000	+0.002	0.002
+0.8900	+1.000	+1.002	0.002
+1.7800	+2.000	+2.001	0.001
+2.6700	+3.000	+3.004	0.004
+3.5600	+4.000	+4.004	0.004
+4.4500	+5.000	+5.005	0.005

Table 4.3: BAMS results for LED ring movement on the motorized linear displacement stage for a movement in the Y-axis. The LED ring was moved in increments of 0.8900 mm in the Y-axis which equated to 1 arcminute steps.

Y-axis position on stage (mm)	Intended Y-axis position (arcminute)	Y-axis displacement (arcminute)	Difference between intended position and actual position (arcminute)
0.0000	0.000	+0.001	0.001
+0.8900	-1.000	-1.001	-0.001
+1.7800	-2.000	-2.000	0.000
+2.6700	-3.000	-3.004	-0.004
+3.5600	-4.000	-4.000	0.000
+4.4500	-5.000	-5.000	0.000

The average error in position for the BAMS movement position from Table 4.2 and Table 4.3 was 0.002 arcminutes. This uncertainty in position included: systematic errors in the actuator, the distance measurement from the camera to the LED ring, as well as error associated with LED stability and centroiding calculations.

4.2.4 Conclusion of Tests

The aforementioned tests proved that the systematic error in BAMS was within the tolerance required for the BAMS system to be used on the HEROES flight. The sum of the systematic errors determined above totals ~ 0.017 arcminutes (or 1.02 arcseconds). This is well below the BAMS requirement of 35 arcsecond accuracy needed for the HEROES flight mission. After the BAMS systematic error was verified, the BAMS hardware was integrated into the payload.

4.3 Payload Integrated Pre-flight Tests

Once the HEROES payload arrived at the Columbia Scientific Balloon Facility (CSBF) in Fort Sumner, N.M. the integration and alignment of the hardware for flight began. Prior to the flight, hang tests were performed in which the HEROES payload was suspended by a crane in a high bay. This allowed measurements at full elevation to ensure all components of the payload would still operate correctly (Figure 4.9) [29].

Figure 4.9: Image of the HEROES payload elevated off the ground using a crane for a hang test at Fort Sumner, N.M. Image credit: NASA/MSFC.

BAMS detected the changes in alignment of the HEROES payload due to gravitational sag in the 6 m long optical bench as a function of elevation angle. Two such tests were performed; results are discussed in the following two subsections.

4.3.1 Hang Test 09/05/2013

The hang test was performed pre-flight in the Columbia Scientific Balloon Facility (CSBF) high bay at Fort Sumner, NM [29]. The HEROES payload was lifted off the floor using a crane until it was fully suspended. The BAMS hardware integrated into the payload was then tested by slowly increasing the elevation of the payload, then cycling through the full elevation angles (0° to 68°) three times. The displacement measurements of the BAMS LED rings are from nominal starting positions for the optics and detector flanges. The cycled payload data is shown in Figure 4.10. Large optical systems are prone to stresses in the mechanical components that ultimately affect performance until relieved. This was seen in the Y-axis as the payload was cycled through the full elevation. A downward trend in the optics half and an upward trend in the detector half of the data was detected due to these stresses being relieved. Although the payload was only moved in elevation, there was also movement in the X-axis, which was most likely due to an offset in the center of mass. The BAMS results for the detector half of the payload reflected tracking in the X-axis via elevation change. Nevertheless, the Y-axis shifted in position and then stayed at the offset even with elevation change [19].
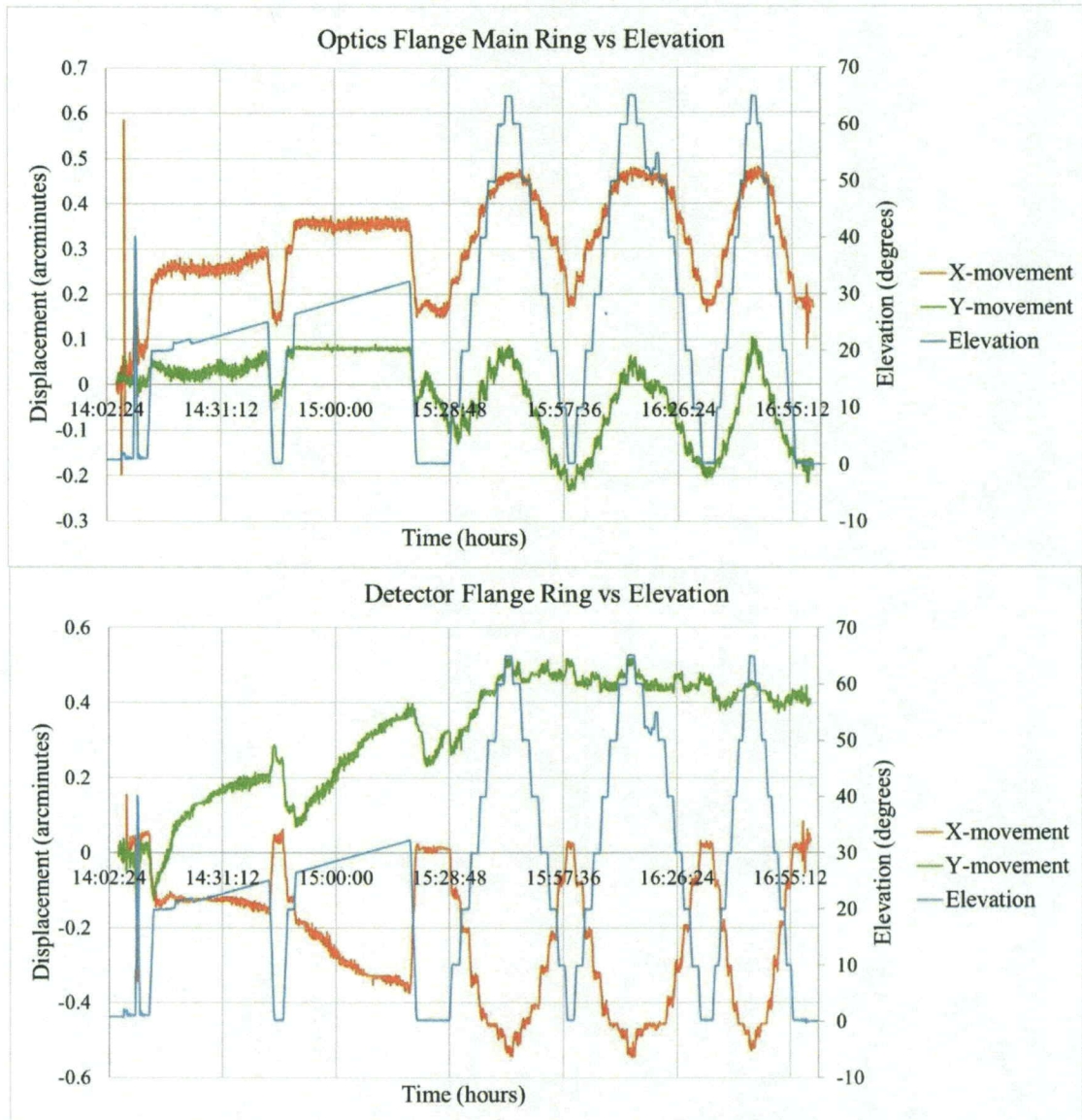
Figure 4.10: Results for the Fort Sumner optics and detector flange hang tests done on September 5, 2013. The payload was cycled through the full elevation three times after an initial elevation increase was done.

4.3.2 Hang Test 09/06/2013

A second hang test was performed in the CSBF high bay at Fort Sumner, N.M. the next day. Mimicking test one, the second test required the payload be raised off the ground by a crane. The payload was then cycled through the full range of elevation angles three times with the elevation held at 60 degrees for the third cycle. The results of this test are shown in Figure 4.11 below. Similar to the first hang test, the X-axis tracked the change in elevation in the detector half of the payload without much change in the Y-axis during the full elevation test. In the optics flange the X-axis followed the elevation change as did the Y-axis but it had a linear shift in position [19].
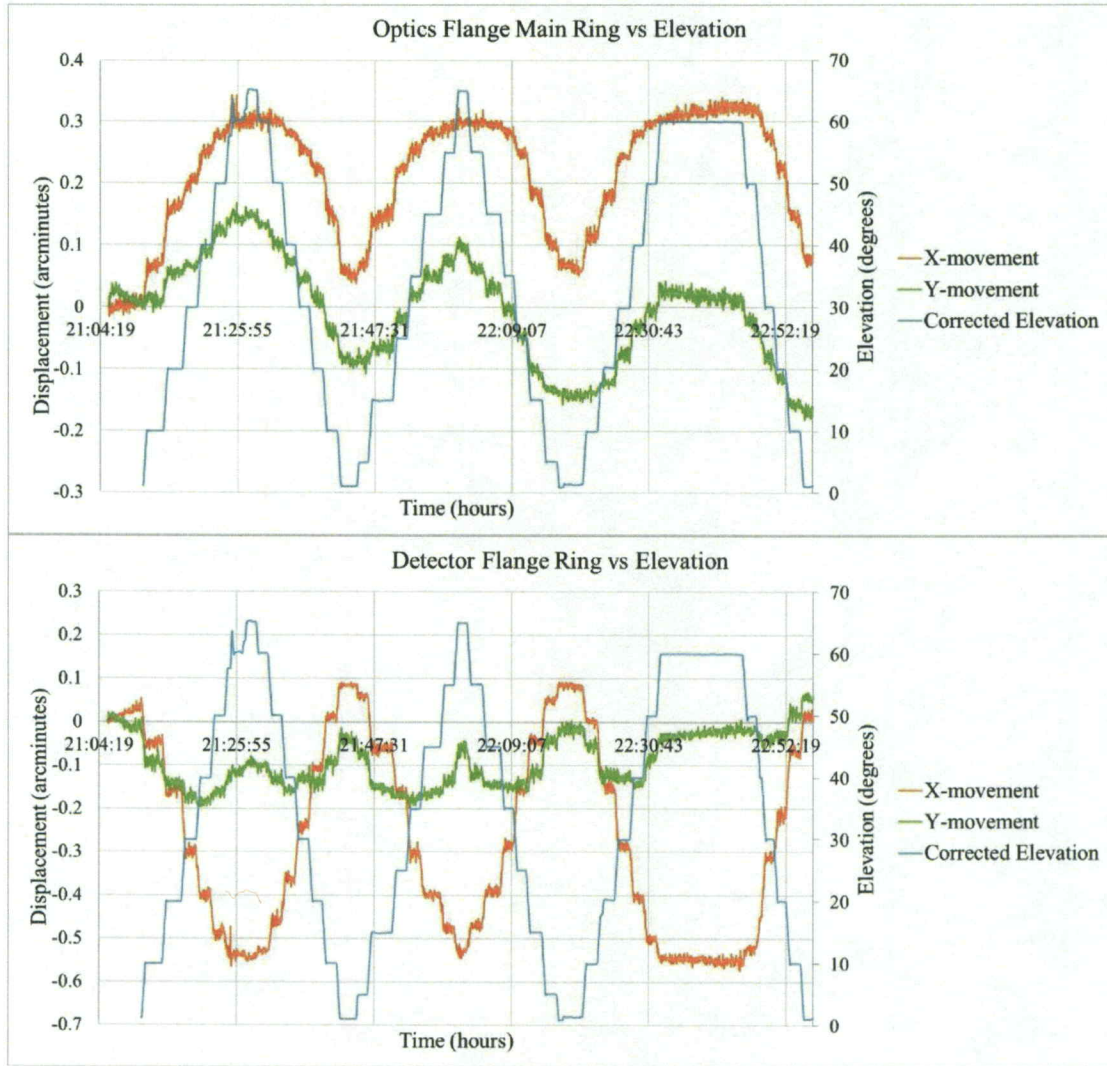
Figure 4.11: Results for the Fort Sumner optics and detector flange hang tests performed on September 6, 2013. The payload was cycled through the full elevation two times and then held at 60 degrees for the third cycle for this test.

84

4.3.3 Results from Hang Tests

The BAMS software was able to track the movement of the LED rings integrated onto the HEROES payload as it experienced elevation changes during both hang tests. The Y-axis produced unusual BAMS results for the detector half of the payload by not tracking with the elevation of the payload; however, the optics half of the payload results tracked the elevation of the payload for both the X-axis and Y-axis. The movement of the X-axis seen during the hang tests comes from one of two possible sources. The first possibility is that the movement recorded by BAMS is actual movement of the two halves of the optical bench. The other possibility is that the elevation flange support bars twisted in such a way that there is X-axis movement which would be why there is a recorded movement in opposite directions between the optics and detector BAMS data. Calculations for the estimated Y-axis deflection that would be seen by the aluminum half of the optical bench are estimated to be ~7 arcseconds, which matches what was seen during the hang test. These tests showed that the BAMS software was able to track the movement of the LED rings due to sag of the payload as the elevation was varied.

4.4 Chapter Summary

The BAMS software was tested by doing a simulation in MATLAB which yielded that an incorrect Nvidia transform was used. This was promptly corrected. The BAMS system was then further tested to characterize the error present in the system; shown to be 1.02 arcseconds, which was well below the 35 arcsecond HEROES requirement for the BAMS software. Prior to flight, BAMS was integrated onto the HEROES payload and two hang tests were executed at the CSBF in Ft. Sumner, NM,

where the payload was elevated using a crane and cycled through the full elevation three times. The BAMS results for the hang tests showed that the system was able to track the change in elevation for both the X-axis and Y-axis of the payload. The results of the completed tests discussed in this chapter proved that BAMS was ready to be used during the HEROES flight.

Chapter 5

HEROES Flight and Results

5.1 Background Flight Information

The HEROES payload was declared ready for flight on September 10th and launched from Fort Sumner, NM on September 21, 2013. See Figure 5.1 [29]. The Columbia Scientific Balloon Facility (CSBF) handled launch preparations, including inflation of the 39 million cubic feet (mcf) balloon, integration of the flight train, operation of the launch vehicle as well as monitoring weather conditions to determine if they were favorable for a launch. The HEROES team handled the payload operations during this time and performed a final power-on check of all of the systems. BAMS software operation was directed at the MSFC. The flight path, seen in Figure 5.2, shows HEROES launching from Fort Sumner, terminating roughly 26 hours later, and landing in a field southeast of the launchpad [29].

Figure 5.1: HEROES payload right before launch. The balloon is inflated in the background with the payload attached to the flight train and launch vehicle. Image credit: reproduced with permission of IEEE. © [2014] IEEE. [29]
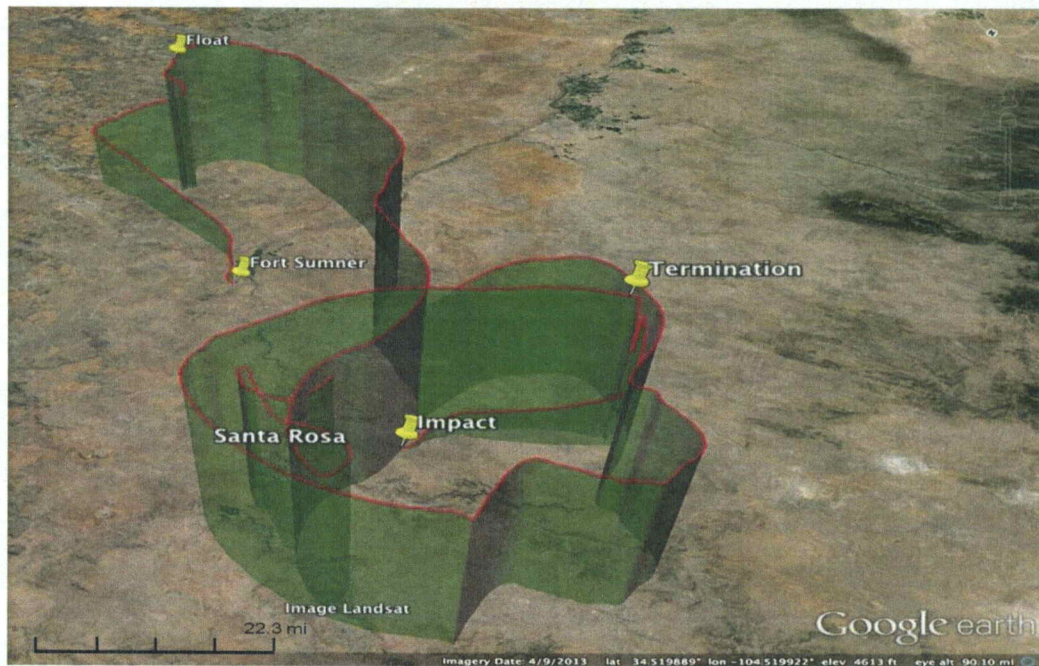
Figure 5.2: Image showing the path that the balloon took during flight. Each pin indicates a significant event of the flight including launch at Fort Sumner, where float altitude was reached, flight termination and impact site. The height of the green path indicates the relative altitude of the payload. Image credit: reproduced with permission of IEEE. © [2014] IEEE. [29]

The Concept of Operations (Con-Ops) is shown in Figure 5.3 [18]. Following launch, ascent to a float altitude of 38 km took approximately 3 hours. Once at this altitude, HEROES was pointed toward the Sun. HEROES observed the Sun for ~7 hours and then slewed to GRS 1915+105, observing it for ~7 hours followed by ~1 hour of system checks, then a 3 hour-long observation of the Crab Nebula until the flight was terminated. The mission lasted for ~26 hours in total [29].
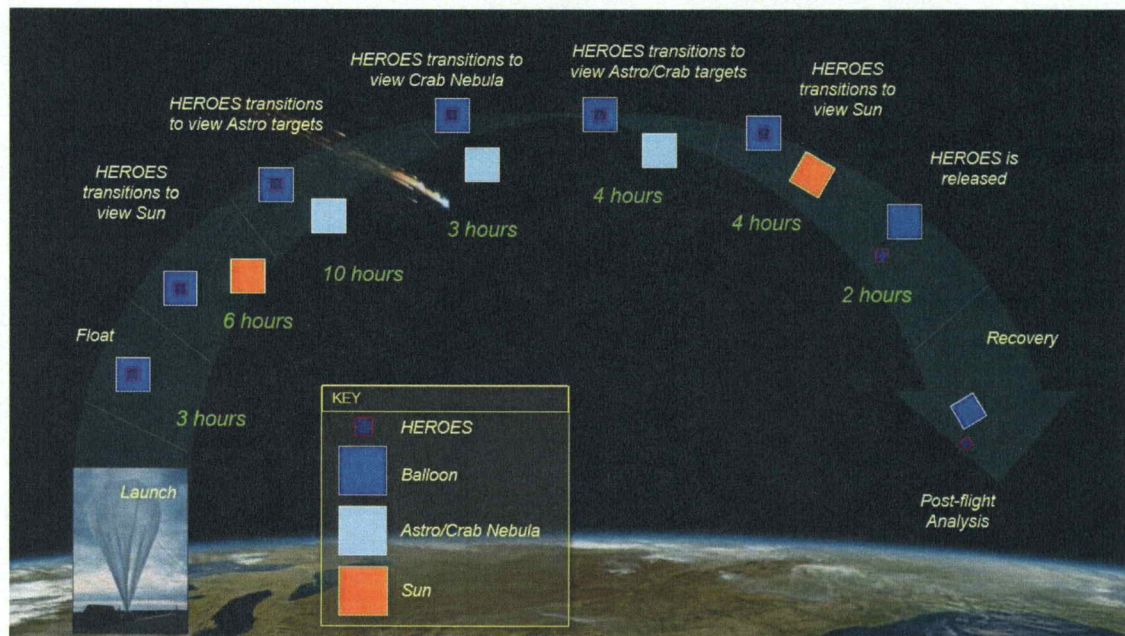
Figure 5.3: Concept of Operation for flight of events split up by time for the duration of the flight. Image credit: reproduced with permission of IEEE. © [2013] IEEE. [18]

During the solar observation, the payload altitude was stable at ~38 km (Figure 5.4 and Figure 5.5). During the GRS 1915+105 observation, the altitude varied between 34-38 km, with the payload decreasing in altitude from 38 km to 34 km in the first 3.5 hours and then staying fairly stable at 34 km for the last 4 hours of the observation. During the Crab Nebula observation, the float altitude varied between 34-36 km with the payload slowly increasing in altitude during the observation [29]. These variations in altitude are expected for high-altitude zero-pressure balloons primarily due to thermal variations in the balloon related to the Sun rising and setting. Vent ducts in the balloon vent helium during the day to prevent pressurizing. During the evening, the balloon cools and has less lift. Ballast is dropped to limit the subsequent drop in altitude [47].
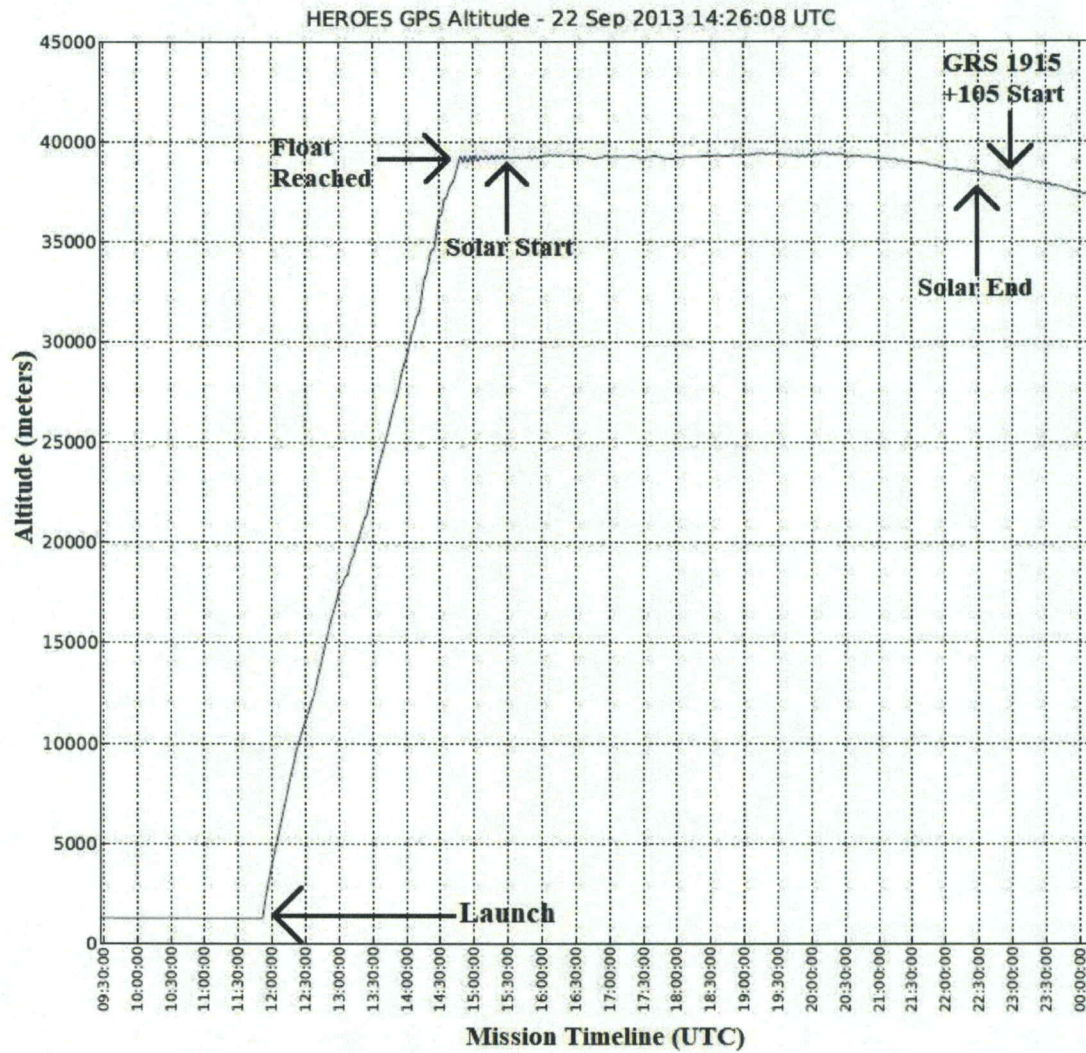
Figure 5.4: HEROES payload altitude from launch to flight termination. Major occurrences during mission are labeled such as launch, float being reached, solar observation start and end, and GRS 1915+105 observation start. Image credit: NASA/MSFC.
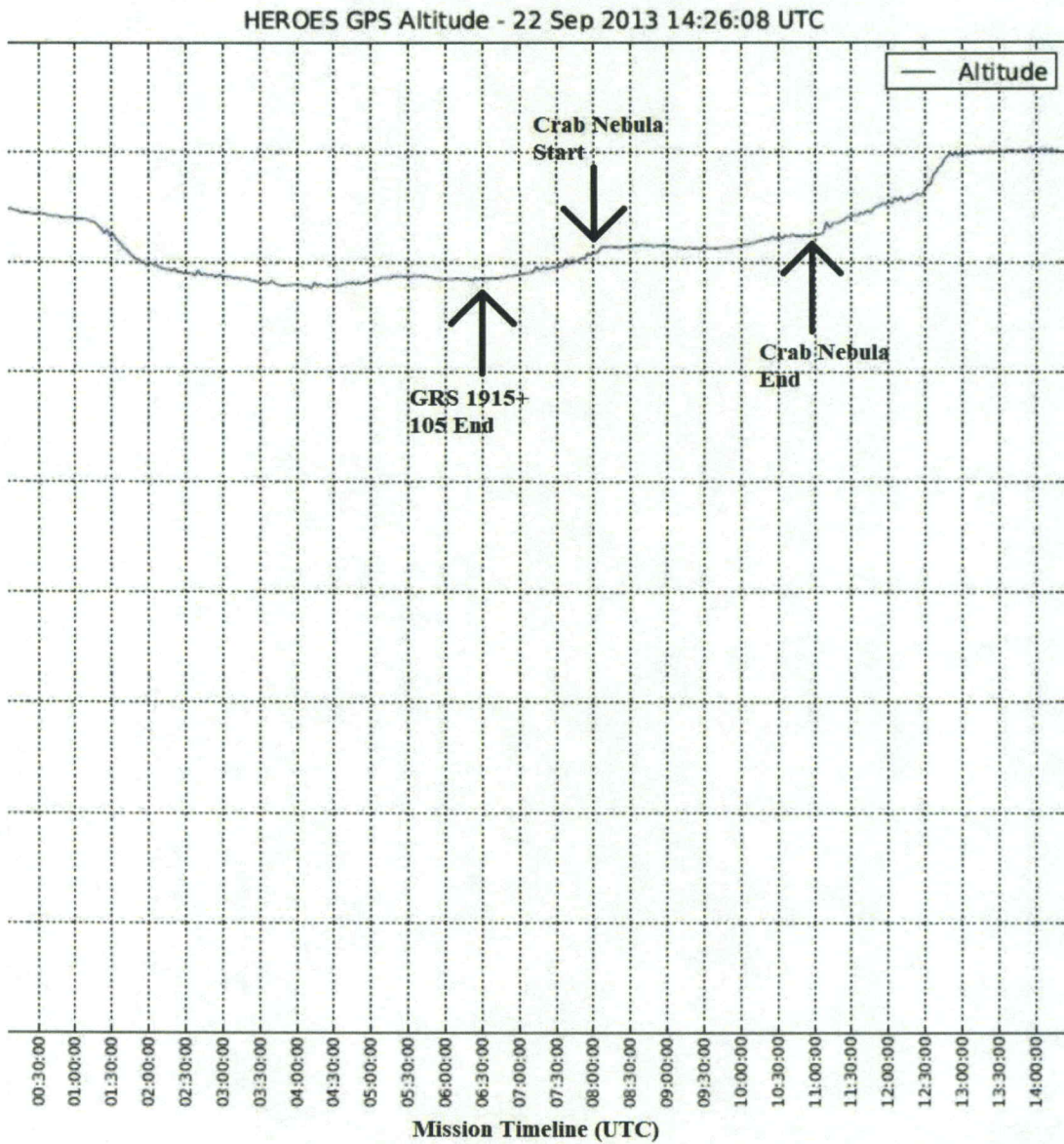
Figure 5.5: Continuation of Figure 5.4. GRS 1915+105 obervation end and Crab Nebula start and end are labeled. Image credit: NASA/MSFC.

5.2 BAMS Flight Analysis

The BAMS flight displacement data was processed post-flight and used to determine how the HEROES payload moved. The displacement data for all of the optics flange rings is shown, along with the rings' relative movement. The BAMS data was also compared to the HEROES payload's elevation and thermal data that were recorded by the HEROES computer. Both are discussed in detail in the following sections.

5.2.1 BAMS Comparison of Optics Flange Rings

The four BAMS LED rings that were mounted to the optics flange and optics modules during flight are shown in Figure 1.12[19]. Three of the LED rings were attached to optics modules and one was attached to the optics flange and the detector flange [19].

The three BAMS LED rings attached to the HEROES optics modules moved independently of the LED ring mounted on the optics flange (Figure 5.6). The difference in the movement of the optics flange rings was most likely due to the optics modules adjustable mounts shifting during launch. These mounts are equipped with adjustable fittings that allow for alignment of the mirror modules to the detectors and use locking screws to 'lock' the modules in place once they have been aligned. It is possible that, based on BAMS results, the locking screws failed and some of the mirror modules shifted slightly during launch. The BAMS LED rings were bolted into place so there was little chance that the rings themselves would move independent of the optics modules or mounting flanges.

93
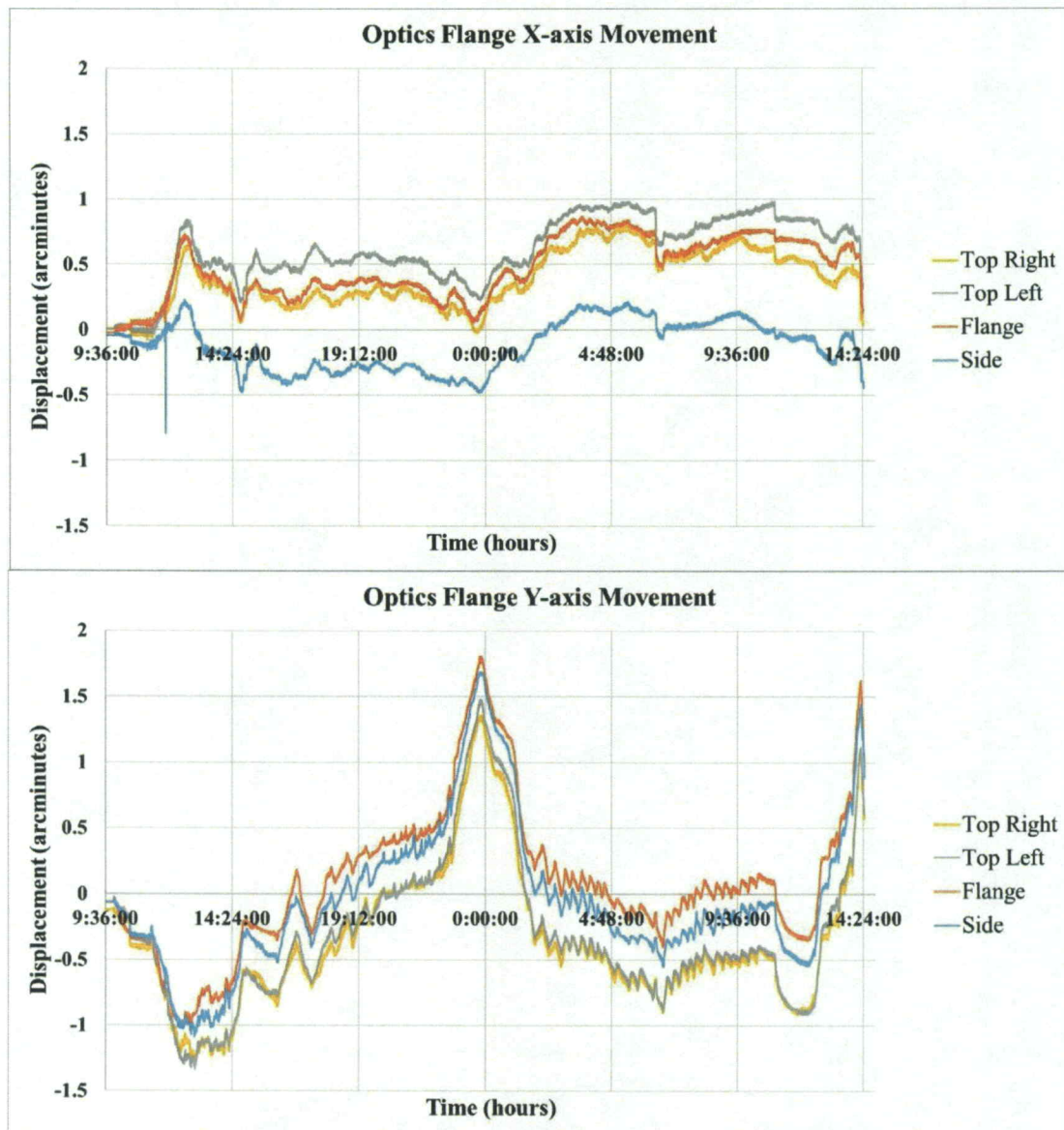
Figure 5.6: Movement of the optical flange X-axis (Upper Plot) and Y-axis (Lower Plot) for the four LED rings mounted to the optics modules and optics flange, over the course of the flight. The reference point for the data (not shown in the plot) is from BAMS data collected the day prior to flight when the payload was in alignment on the ground at an elevation of ~0 degrees.

Once the payload reached its float altitude, the LED rings attached to the optics modules followed roughly the same displacement pattern as the flange LED ring, but with a different offset over the course of the flight (Figure 5.6). This movement is most likely not a result of the detectors moving independently of the detector flange. This is because the detectors were bolted into place prior to ground alignment. Henceforth, the optics flange main ring is referred to as "FWD" and the detector flange ring is referred to as "AFT".

5.2.2 Angle Offset and Elevation Vs Time

The BAMS results for the optics and detector flange rings were plotted against the payload elevation over the course of the flight as shown in Figure 5.7. As discussed in Chapter 4, the elevation of the payload as it pointed toward an astronomical source correlated to movement of the HEROES optics modules. This movement was also seen during flight in the BAMS displacement results; specifically, this is seen between 07:00 to 10:50 when the payload was observing the Crab Nebula. As the payload increased in elevation, the displacement decreased linearly for the AFT rings, and increased linearly for the FWD rings.

Independent movement of the BAMS cameras from the elevation flange was not a concern in contributing to the displacement due to changes in elevation because they were bolted in place at the elevation flange of the HEROES payload, which is the pivot point for the payload. The misalignment due to changes in elevation of the optical bench during the flight followed the movement observed during the hang tests done prior to flight.
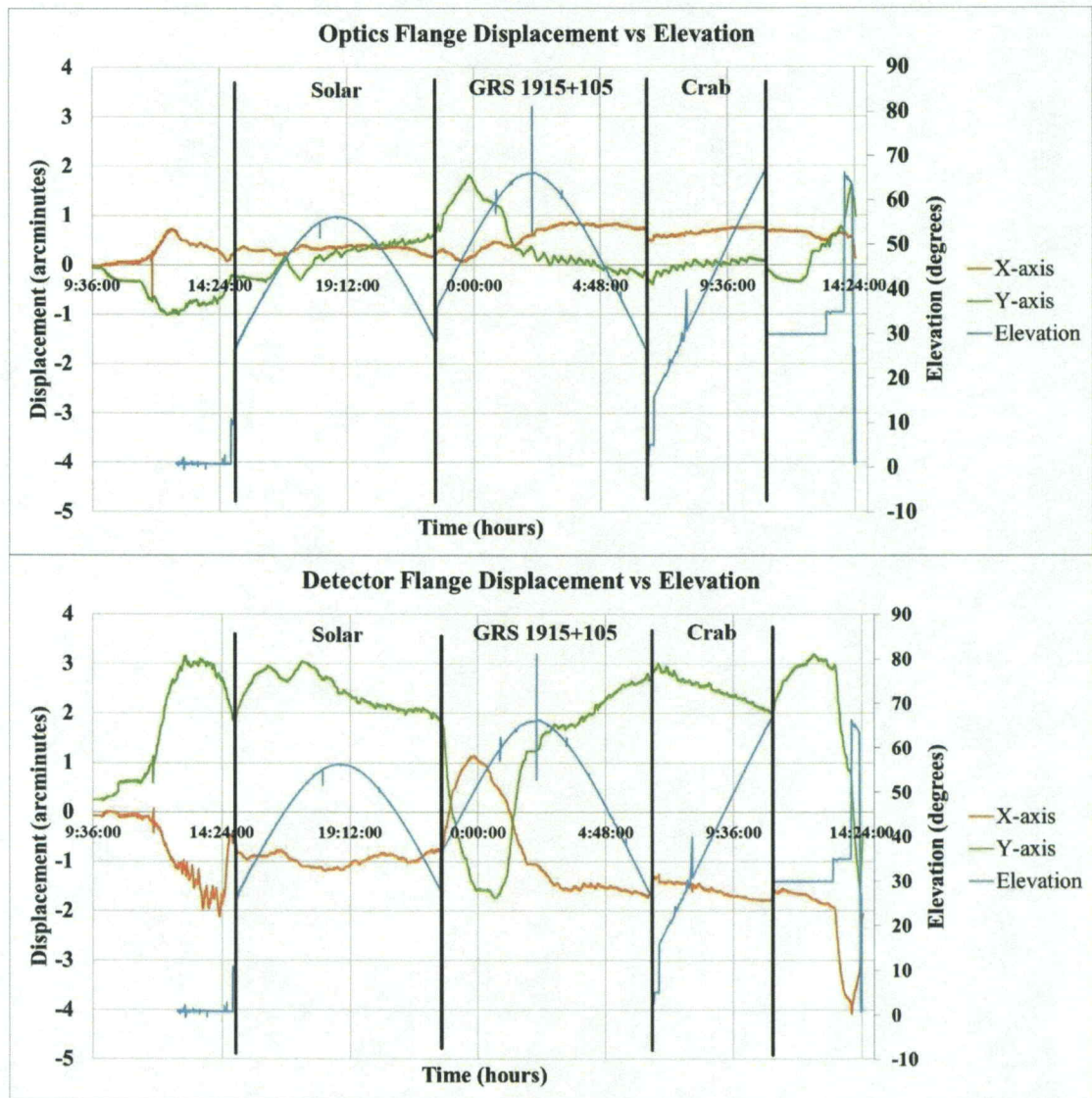
Figure 5.7: Movement of X-axis and Y-axis versus elevation of the payload for optics flange main ring (Upper plot) and detector flange ring (Lower plot). The reference point for the data (not shown in the plot) was selected from images collected the day prior to flight when the payload was in alignment on the ground at an elevation of ~0 degrees.

As the payload changed in elevation, the optical bench experienced sag. The slight changes in sag resulted in a BAMS measured misalignment between the optics modules and their corresponding detectors, with the Y-axis experiencing a larger displacement. In Figure 5.7, the change in sag as a function of the elevation of the optical bench can be seen in several places such as during the Crab Nebula observation, during the second half of the GRS 1915+105 observation, and during the solar observation.

5.2.3 Angle Offset and Temperature VS Time

The HEROES payload was outfitted with temperature sensors to monitor real-time temperature fluctuations and to provide validation for the thermal model produced by other MSFC personnel. As discussed previously, it is not uncommon for high-altitude balloon payloads to experience temperature changes due to the changing position of the Sun relative to the payload during the day and colder nighttime ambient temperature. If the payload has mismatched Coefficient of Thermal Expansion (CTE) between elements, thermal gradients can cause flexing, which can result in small misalignments between the optics and detectors. Even small misalignments on an X-ray telescope can reduce performance and even degrade the Point Spread Function (PSF). The thermal gradient experienced by the HEROES optical bench varied up to 40 degrees Celsius from port to starboard and top to bottom. This was expected and planned for, based on pre-launch thermal analyses of the optical bench as shown in Figure 5.8 and was not expected to cause any issues during flight [48].
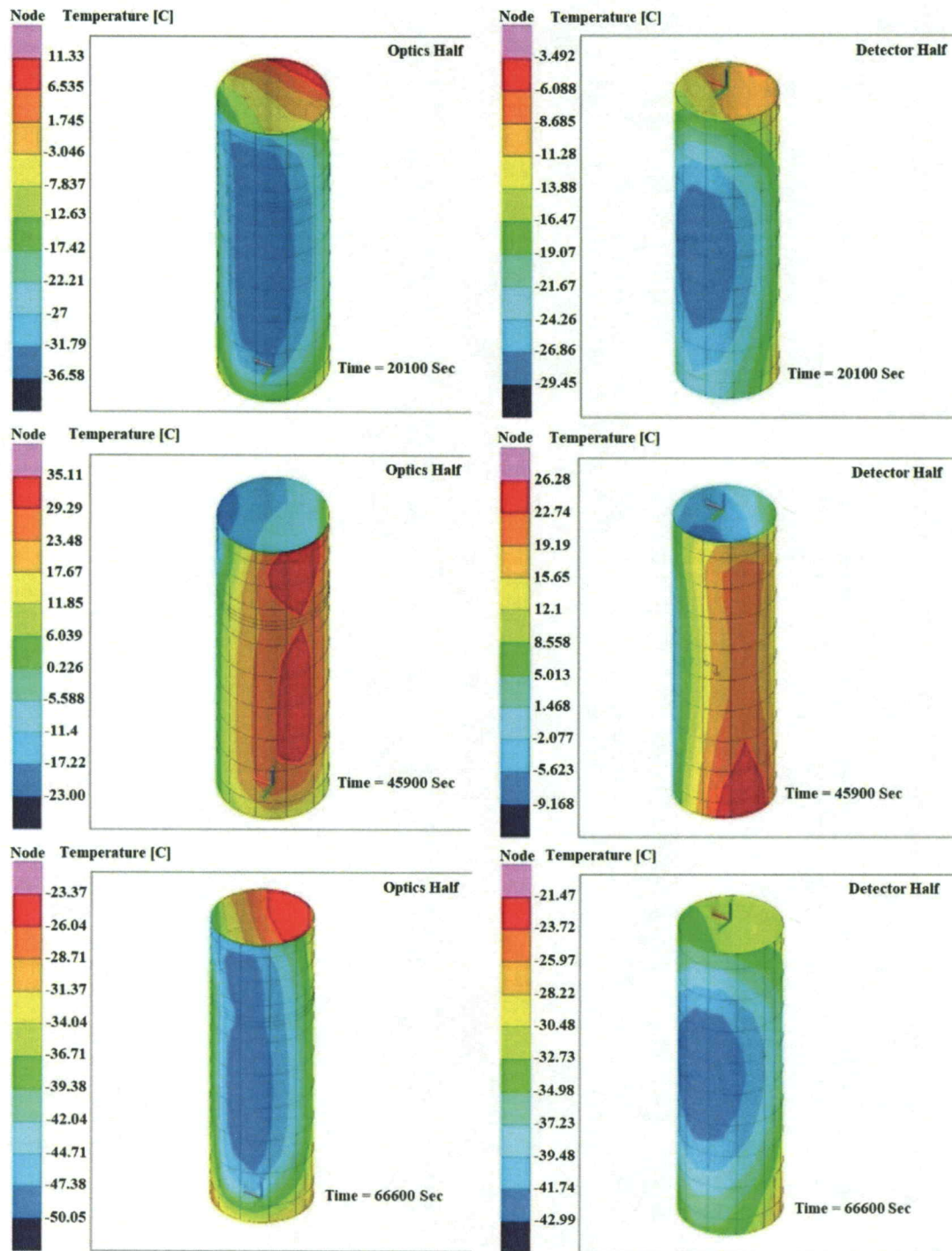
Figure 5.8: Model of the thermal variation experienced by the HEROES optical bench for the optics flange in the left column and the detector flange in the right column. The thermal variation of the payload is shown for three different observations during flight. First row: Solar observation with duration of 5.5 hrs. Second row: GRS 1915+105 observation with duration of 12.75 hrs. Third row: Crab Nebula observation with duration of 18.5 hrs. Model credit: Brian O'Connor NASA/MSFC.

There is substantial correlation between the thermal gradients in the optical bench and the relative movement between the mirror modules and detectors recorded by BAMS. The BAMS cameras were held thermally stable during the flight by employing heaters and were bolted in place at the elevation flange. The LED rings were bolted in place and made of a low CTE plastic. Thermal-vacuum tests were also done on the ground to verify operation of the BAMS system. The possibility of mechanical shifts of the BAMS components was also ruled out during ground tests consisting of hang tests at Fort Sumner which were described in Chapter 4. The BAMS absolute displacement data was also compared to the Pitch-Yaw Aspect System (PYAS) differential displacement data and this is discussed in section 5.3.

The largest movement that BAMS measured was during the observation of GRS 1915+105. During this observation, there was uneven exposure of solar radiation on the payload, causing a thermal gradient across the optical bench as seen in Figure 5.9 and Figure 5.10. One-half of the optical bench is made of carbon fiber that was specifically fabricated to have a CTE matched in the Z-axis to the other half of the optical bench, which is made of aluminum. The two halves are joined by the elevation flange as discussed in Chapter 2. The location of this flange is where the BAMS cameras are also mounted. Both sides are painted with the same bright white paint. BAMS recorded a larger movement for the aluminum side (to which the HEROES detectors are attached) due to the higher CTE than the carbon-fiber side (to which the optics modules are attached). The use of different materials for the optical bench was not by original design. Rather, HEROES was modified following a previous flight mishap that compromised the optical bench. The entire optical bench, the detector half and optics half, was originally

fabricated of carbon fiber. BAMS recorded a sag of 1.74 mm of the X-axis of the aluminum half of the bench during the GRS 1915 observation, which matches the calculated deflection caused by the measured 27 °C gradient across the X-axis of the aluminum half of the optical bench during the flight. For the carbon composite half of the optical bench, a positive Y-axis movement was seen during the GRS 1915+105 observation. The positive movement may be due to the weaving of the carbon fiber, which would contract when it is heated. The temperature gradient required to see the positive Y-axis movement of the carbon fiber during the GRS 1915+105 observation would have to be ~41 °C for the displacement observed during the flight.
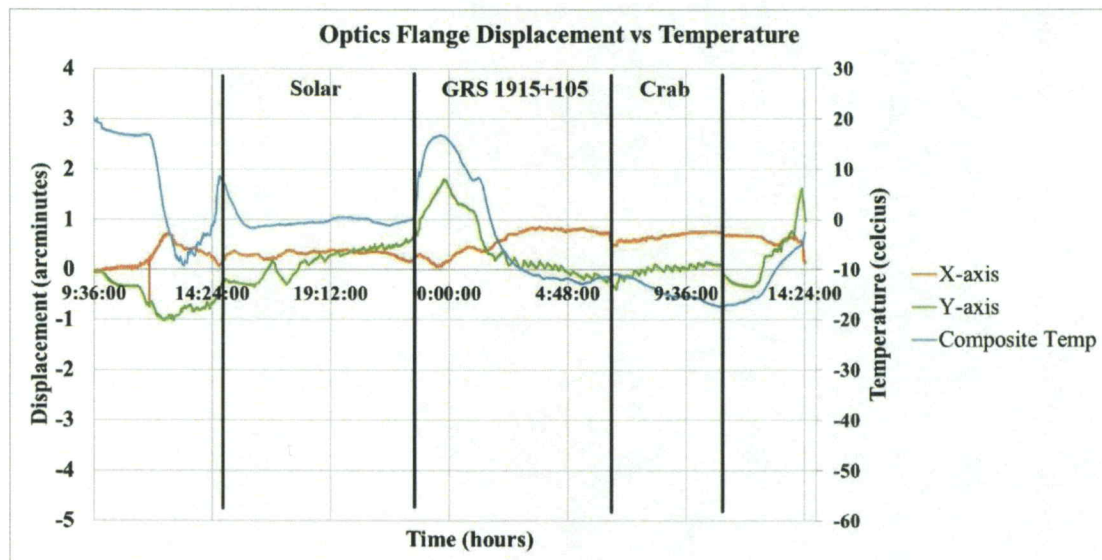
Figure 5.9: BAMS results for the X-axis and Y-axis versus temperature of the carbon fiber half of the payload for the optics flange main ring.
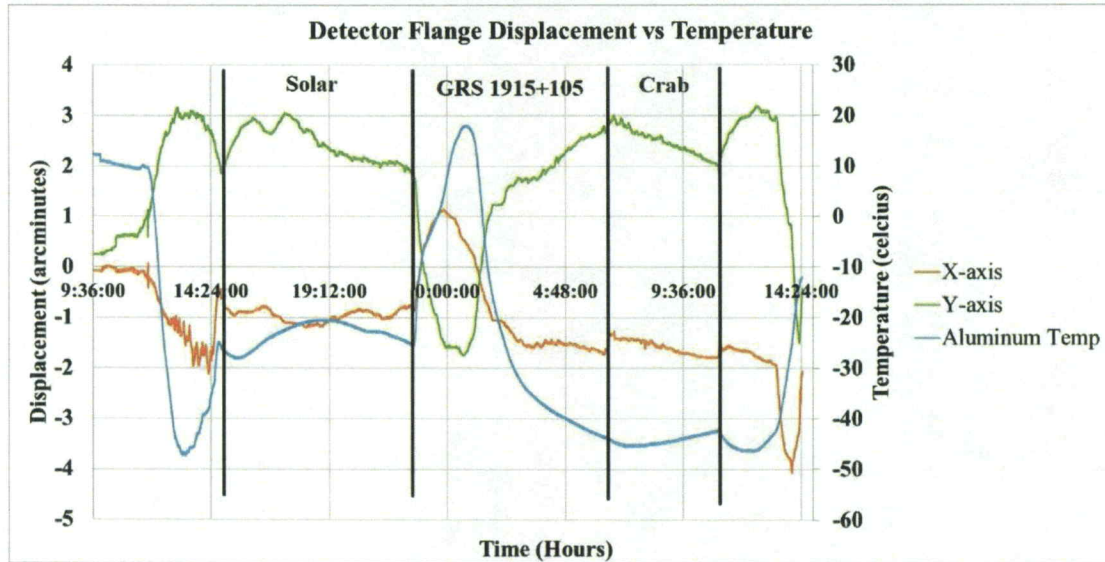
Figure 5.10: BAMS results for the X-axis and Y-axis versus temperature of the aluminum half of the payload for the detector flange ring.

5.2.4 BAMS Error Budget

The BAMS error budget is composed of three different elements: electrical, thermal, and mechanical (Table 5.1). Electrical errors are related to the components of the BAMS system such as the CCDs and LEDs, and indirectly from the gondola power system. These errors are evident in the BAMS software. These errors were discussed in detail in Chapter 4. Thermal errors are caused by thermal gradients across optical bench components. Mechanical errors are due to movements of the optical bench elements and the BAMS mounting hardware, such as the twisting of the elevation flange and movement in the bolts for the LED rings.

It is assumed that mechanical error associated with movement of the bolts holding the BAMS components is negligible, though it is possible that the bolts were not torqued down to the appropriate levels. This human error is difficult to account for and has not been included here. Movement of the bolts holding the LED rings and CCD mount due to thermal variations is unlikely due to the parts being thermally controlled to +/- 5 °C. The possible error due to the movement of the LED ring bolts are not included in the error budget because the results from Section 5.2.1 show that the LED rings moved with the same displacement pattern during the flight which is highly unlikely if the bolts loosened and the components were free to move. The possible error contribution from bolt movement is +/- 8.73 arcseconds for movement of each component such as the mount, CCD and LED ring if they were to come loose.

Movement along the X-axis was observed by the BAMS cameras during the hang tests in Ft. Sumner. There are two possibilities for this movement. The first possibility is that the X-axis movement is mechanical movement of the two halves of the optical bench and the other possibility is that the elevation flange experienced a twisting motion in the crossbars where the CCD mount was attached. If the first supposition is correct, then the X-axis movement is real and therefore does not contribute to the error budget. If the movement is a twisting of the elevation flange, then the movement can be accounted for in a predictable manner and removed from the BAMS data. Similarly, any thermal movement of the CCD and mount also can be accounted for in a predictable manner and removed from the data post flight. The values provided for the thermal CCD/mount and the elevation flange X-axis movement in Table 5.1 are the errors for removing these terms from the BAMS data.

All of the sources of error included in the error budget are of comparable value, so there is no dominant source of error. As mentioned previously, movement of the bolts is unlikely so the possible error from these components are not included in the total. The total error in the BAMS system error budget comes out to +/- 3.0 arcseconds, which is well within the accuracy requirement of 35 arcseconds. The most likely sources of error were the thermal and electrical errors and ultimately what limit the performance of the BAMS system.

Table 5.1: The error budget for BAMS. The errors are added in quadrature to obtain the total value.

Type	Component	Error (arcsecond)	Notes
Electrical			
	LED brightness	+/- 0.3	From Section 4.2.1
	LED stability X-axis	+/- 1.2	From Section 4.2.2
	LED stability Y-axis	+/- 1.2	From Section 4.2.2
	Linear displacement	+/- 0.4	From Section 4.2.3
Thermal			
	CCD and mount (optics)	+/- 1.2	CCD/mount were temperature controlled to +/- 5 °C
	CCD and mount (detector)	+/- 1.2	CCD/mount were temperature controlled to +/- 5 °C
	LED ring	+/- 0.6	Change in LED ring size from thermal expansion of the ABS
Mechanical			
	Elevation flange X-axis movement (detector)	+/- 1.2	Error due to movement of the X-axis during a change in elevation
	Elevation flange X-axis movement (optics)	+/- 1.2	Error due to movement of the X-axis during a change in elevation
Total		+/- 3.0	Maximum error possible

5.3 BAMS Analysis Comparison with PYAS

During the solar observation, the PYAS system, which was described in Chapter 2, recorded the relative alignment of the HEROES payload's optical bench. PYAS consisted of two sub-systems, the PYAS-Front (PYAS-F) and PYAS-Rear (PYAS-R), which have identical configurations and each provided aspect information independent of the other (Figure 5.11) [30]. Each system measured aspect by focusing a narrow wavelength image of the Sun onto a 1 megapixel CCD with a plate scale of 10 arcsec/pixel. PYAS located the center of the Sun using fiducials to determine solar position, which in turn provided pointing offset and aspect data. The lens for PYAS-F was mounted to the optics flange, and its CCD was attached to the elevation flange. The lens for PYAS-R was mounted to the elevation flange, and its CCD was attached to the detector flange. Both sub-systems provided aspect information, but higher accuracy aspect data was obtained post-flight by processing images from each CCD. The PYAS aspect images were recorded at a rate of up to 10 Hz [30].
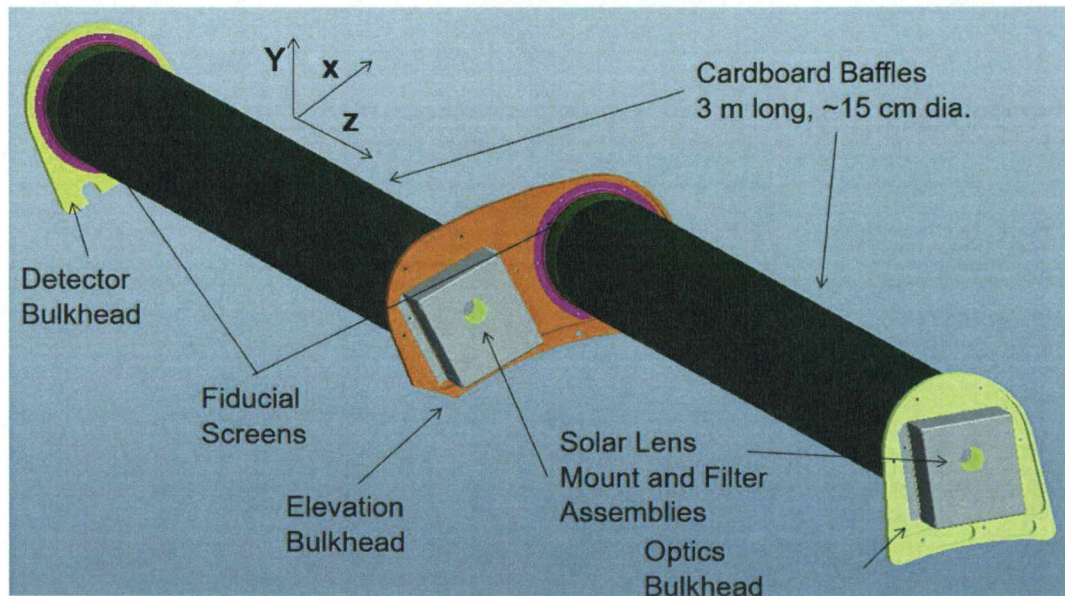
Figure 5.11: CAD model of the PYAS-F and PYAS-R mounted together on the elevation bulkhead. At the end of each baffle is a fiducial screen. At the front of each baffle is a solar lens and filter. Each sub-system has a focal length of 3 m. Image credit: Alex Sobey NASA/MSFC.

A comparison of the PYAS differential displacement data and the BAMS absolute displacement data during the solar observation of the HEROES flight (seen in Figure 5.12) shows that the BAMS measured results matched the PYAS results. The PYAS recorded relative alignment data every second while BAMS recorded alignment data every three seconds. A running average of the PYAS alignment data was done to reduce noise present in the PYAS data. The PYAS alignment monitoring system verified the displacement results produced by the BAMS data, providing confidence that BAMS was reporting accurate alignment information during the flight. The average difference between the two data sets was ~7 arcseconds. The HEROES payload was pointing directly at the Sun so there was minimal thermal gradient across the payload which was the best case scenario for observations while the Sun was above the horizon.
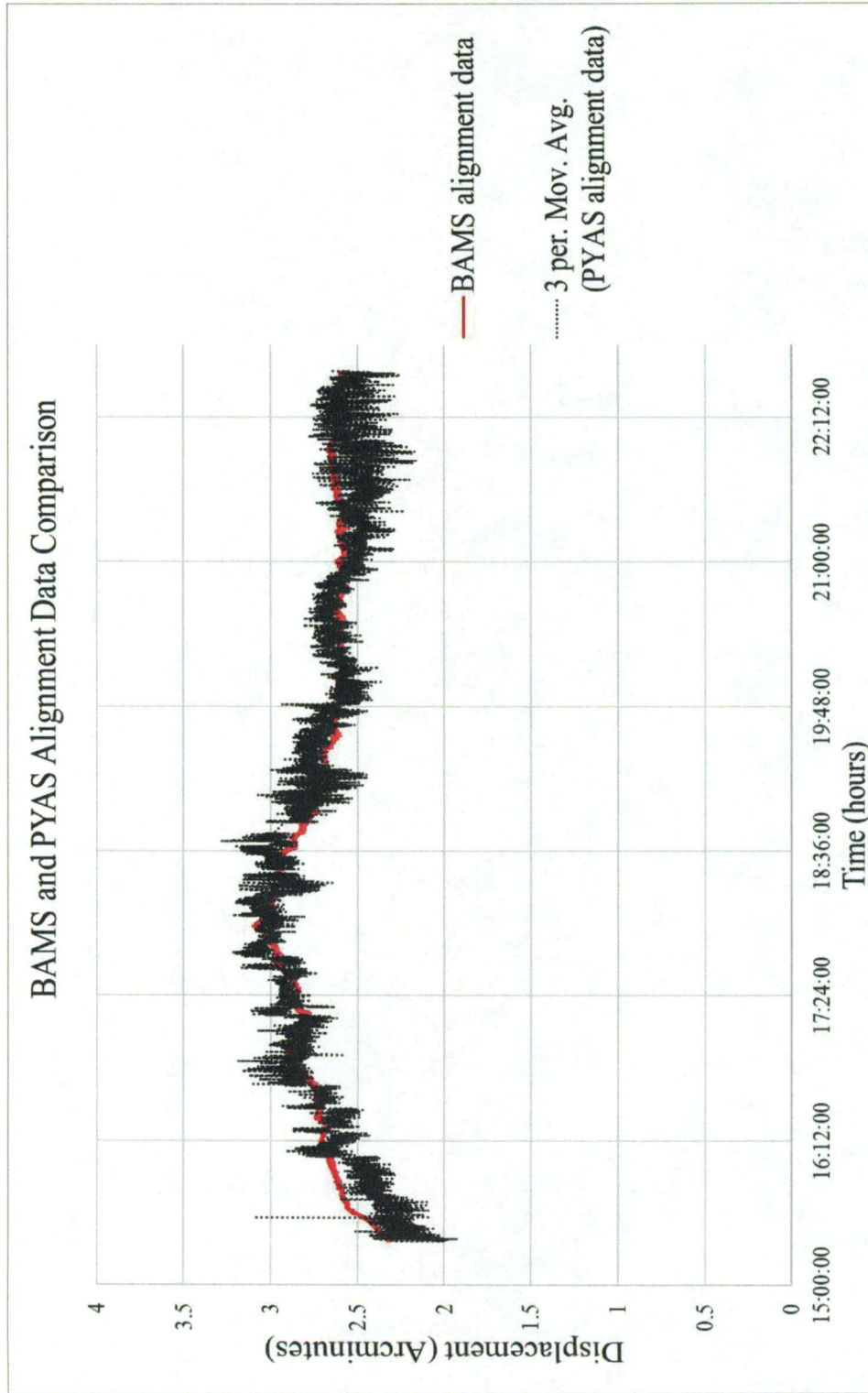
Figure 5.12: Comparison of the BAMS alignment data versus the PYAS alignment data. The PYAS differential displacement data was averaged over every 3 points for smoothing purposes because of high fluctuations.

106

5.4 HEROES X-ray Reconstruction Software

After verification with PYAS that BAMS reported accurate alignment information, installation of the reconstruction software had to be done to process the X-ray data. Post flight, the X-ray data collected by the HEROES payload was processed using software designed by Dr. Allyn Tennant (NASA/MSFC). The software used to analyze the X-ray science data from the HEROES flight is called "HERO_Soft" [49]. The HERO_Soft software is an interactive X-ray image analysis program, originally designed to extract useful results from EXOSAT LE data. It is currently used for analyzing FITS images and/or event lists [50].

HERO_Soft software runs on a Linux operating system and requires prior installation of the HEAsoft-software package. The HEAsoft software package was installed using the g95 Fortran compiler, specifically the 64-bit version [51]. A list of the major program files in the HERO_Soft software and their descriptions is summarized in Table 5.2.

Table 5.2: Descriptions of the main program files in the HERO_Soft program used to reconstruct the X-ray data.

File name	File Description
Caspect.o	Calculates the HEROES aspect solution using GPS data, aspect data, BAMS data and clock sync data. It was also used to obtain the pointing and roll data from the House Keeping (HK) FITS files.
Makefile.xan	Builds the HERO_Soft program so that it had the appropriate inputs.
Mkfits.sh	Converted raw data files for each detector to FITS files that were used later to build the image for each source.
Evt2fits.o	Builds FITS files for each detector and generated the FITS files detXX.fits, detXXt.fits and detXXs.fits where XX is the detector number. The detXX.fits files contained all of the X-ray position and energy data for their corresponding detectors, including pairs of events. The detXXt.fits files then added a time column to the data that was given in Julian time. The final set was the detXXs.fits files that took the detXXt.fits files and separated out the pairs of events leaving only the single count events from the X-ray data due to the issues present with processing pairs of events.
Hgtepc.o	Used to obtain the tap corrections for each detector that was then used to get energy and position of the photons absorbed by the detector. The taps are discussed in more detail in Chapter 2.
Tapfit.o	Applies gain correction to each tap to properly adjust the offset for each. There are 16 taps per detector. This is required to yield the accurate event positions for each of the detectors.
T2dfit.o	Inputs the gain corrected tap data to yield a final accurate event position on the detector.
Gse2fits.o	Reads GSE raw data stream and outputs FITS files for each parameter. It opens the packet decoder files to process the GSE raw data and output a FITS file for each of the packet decoder files. There are several subproject files that process the HK data to obtain information such as observation time, aspect image data packets, M12 GPS data, etc… and outputs the data into FITS files.
Doit.sh	Builds a FITS file from the detector data FITS files and the HK FITS files. The outputted FITS files were corrected for the HK data so that the events corresponded to the same absolute center during the duration of the source observation. Data from all 8 detectors was merged into a single image for the source to get a total FITS file.
Fltofi.o	Converts BAMS data into FITS files to be used by "Caspect.o" to obtain the position data for the reconstruction.

5.5 Reconstruction of Crab Nebula and GRS 1915+105

The two nighttime astrophysical sources that were observed were the Crab Nebula and GRS 1915+105. Reconstruction of the X-ray data is achieved when the astronomical source data is combined from all eight HEROES detectors into a single image along with the spectrum. The reconstruction depends on the number of incident photons. If there are too few photons, then the source photons will not be above the background X-ray photons and the result will be an image with no source that can be distinguished. The number of photons collected during an observation is directly influenced by pointing error and misalignments between the optics and detectors.

5.5.1 Misalignments

Misalignments between the optics and the detectors may impact the post-flight data reconstruction by linearly shifting source X-rays away from the center of the detector focal plane and/or by decreasing the count rates from the observed source. There are three types of misalignment that can affect image reconstruction and they are lateral, angular, and rotational misalignments (Figure 5.13).
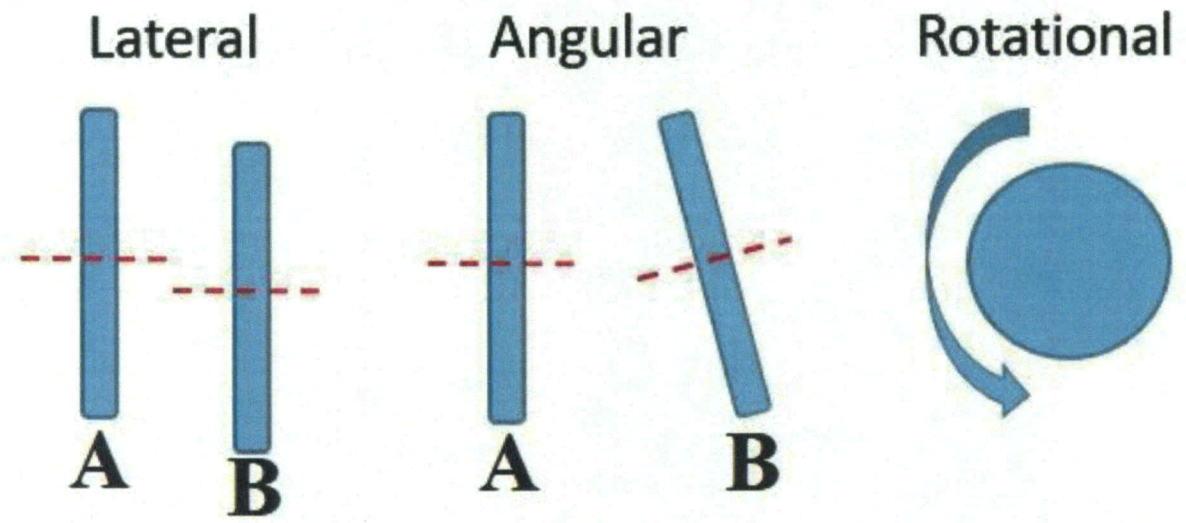
Figure 5.13: Examples of Lateral, angular and rotational misalignment are shown. For the lateral and angular misalignment examples shown, "A" represents the optics flange and "B" represents the detector flange or vice versa. The rotational misalignment example represents either of the flanges. Each of the optics modules can also experience any of these misalignments independently of the optics flange.

BAMS LED rings were attached to the detector flange, optics flange and to three optics modules. The detectors were bolted to their respective flange, which meant that independent movement of the detectors from the flange was less likely, and so individual LED rings were not mounted onto individual detectors. If LED rings were attached to all eight optics modules it would be possible to correct for the total misalignment between these and the detector flange. However, resources only allowed for 3 mirror modules to be monitored on this particular flight.

A rotational misalignment occurs when the optics modules, detectors or the flanges are rotated from their original aligned position. Rotational misalignment of an optics module has minimal effect on the observation of the source; however, if either of the flanges or any of the detectors were to rotate as a function of time over the course of

an observation it could appear as movement of the source X-rays on the detector and be indistinguishable from a lateral misalignment. Future work will involve including the ability to accurately track rotational misalignment similar to the lateral misalignment detected by BAMS.

A lateral misalignment occurs when either the optics modules or the flange shifts up/down or left/right (X-Y direction) from their original aligned position. Lateral misalignments have minimal effect on the count rate for an X-ray observation. The detectors do not have a uniform response across the detector but within the inner 5 arcminutes of the detectors, the position data is relatively consistent, with more distortions present toward the edges of the detectors [4]. The gain is fairly consistent out to ~5-6 arcminutes but with more variation as the source moves toward the edges of the detectors [4]. Lateral misalignment of the optics modules or flanges would appear as though the X-ray source were moving on the detector. BAMS tracks lateral movement of the LED rings during the flight so this type of misalignment would be simple for BAMS to correct. The observed X-rays over time would need to be shifted back to the correct position with the recorded BAMS data. This is critically important information when multiple telescopes are involved, such as on HEROES, which uses 8 optics/detector assemblies to make a single observation.

The third type of misalignment and most difficult to correct for is an angular misalignment (tip/tilt) of the optics modules and/or flanges. An angular misalignment of the optics could severely reduce the observable count rate from an X-ray source because, as was discussed in Chapter 1, the critical angle of X-ray optics is only a few arcminutes. An angular misalignment of the detectors would produce inaccurate position coordinates

for the X-ray photons captured by the detector. Angular misalignments also introduce aberrations into the reconstructed image and are illustrated in Figure 1.5[4]. A more detailed account of this testing is presented in Chapter 1.

An angular misalignment would appear as a tip/tilt of the BAMS LED rings which would cause the LED rings to change in shape as seen by the CCD [4]. The capability to determine angular misalignment has not been integrated into the BAMS software but future work will involve testing BAMS's ability to determine angular misalignment and adding this capability to the software.

5.5.2 Pointing Error Considerations

Telescopes perform two basic functions: pointing to a source that is of interest and collecting photons from the source into an instrument or detector [52]. Pointing error is the difference between where the telescope is supposed to be pointed and where it is actually pointed (Figure 5.14) [52]. In Figure 5.14, the telescope "real target" is offset from the "pointing target." The pointing error along the azimuth axis is ΔA and ΔE is the pointing error in elevation axis. Pointing error can be caused by multiple factors such as optical alignment, flexure of the tube, and CTE mismatch between elements [52]. BAMS can improve image reconstruction due to misalignments between the mirrors and the detectors; however, BAMS cannot improve image reconstruction due to errors in the pointing caused by misalignments between the aspect system (star camera) and the telescope optical axis.
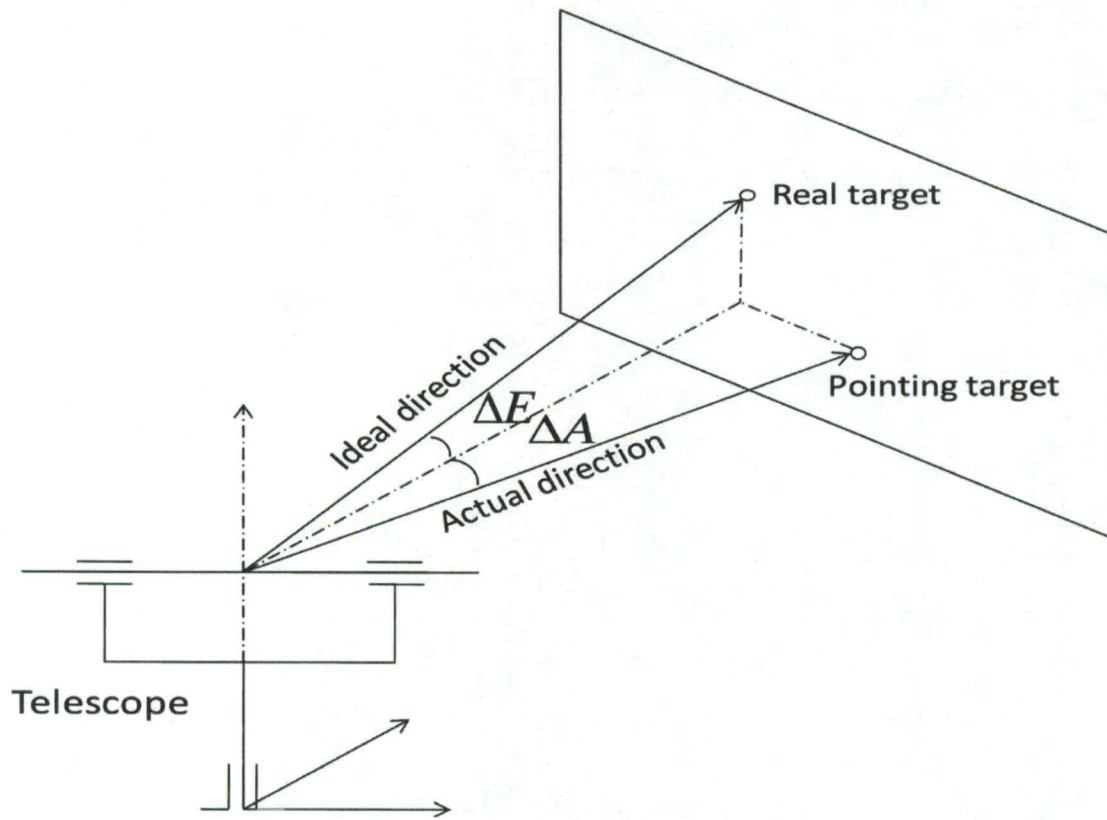
Figure 5.14: Diagram showing pointing error. The telescope should be pointing in the ideal direction toward the real target but is instead directed in the actual direction toward the pointing target. Image credit: Reprinted from New Astronomy, 47, Long Huang, Wenli Ma and Jiarui Huang, Modeling and calibration of pointing errors with alt-az telescope, 105-110., Copyright (2016), with permission from Elsevier. Reprinted from The Lancet, 47, Long Huang, Wenli Ma and Jiarui Huang, Modeling and calibration of pointing errors with alt-az telescope, 105-110., Copyright (2016), with permission from Elsevier. [52]

A pointing error can result in a significant decrease in the number of X-ray photons that are focused by the optics. The pointing errors during the Crab Nebula and GRS 1915+105 observations were calculated post-flight by determining the difference between the image location on the detectors and the telescope's central axis (Table 5.3). Images of the reconstructed X-ray data of the Crab Nebula with and without correction

using the BAMS displacement data are shown in Figure 5.17. The pointing error was

calculated for both of the reconstructed images. The plate scale was 3.4 arcseconds/pixel,

indicating that the payload was pointing ~3.6 arcminutes off-axis of the source location,

or "real target" position.

Table 5.3: Pointing error results for Crab Nebula observation for both the BAMS corrected and uncorrected reconstructions. BAMS data can only correct pointing errors associated with misalignment of the optics and detectors.

	Gaussian X/Y Center of Crab Nebula (pixels)	Gaussian X/Y Center of Detector (pixels)	Pointing Error (arcminutes)
Corrected	981/1028	940/980	3.578
Uncorrected	1008/1020	968/970	3.628

Simulations of the count rates vs photon energy were carried out for the Crab

Nebula and GRS 1915+105 to obtain estimated values. These simulations illustrate the

decrease in source counts as a function of pointing error. Multiple variables were held

constant for the simulation and the average value for each variable was assumed. These

are listed for the Crab Nebula and GRS 1915 + 105 observations in Table 5.4. Variables

not kept constant include the effective optical surface area (the surface area of the optics

that can focus X-rays as a function of energy), mass attenuation, detector quantum

efficiency, photon energy, photon count rate and atmospheric transmission.

Table 5.4: Assumed parameters for simulating the number of X-ray photon counts vs photon energy for the Crab Nebula and GRS 1915+105.

Input variables kept constant	Crab Nebula	GRS 1915+105
Unobstructed View	90 %	90 %
Payload Elevation	49.4 degrees	52.9 degrees
Float Altitude	35.8 km	35.4 km
Atmospheric Column Density	5.23 mb	5.47mb
Elevation Angle	49.4 °	52.9 °

Simulations of the count rate versus photon energy for both the Crab Nebula and GRS 1915+105 were carried out assuming no pointing error and a pointing error of 3 arcminutes (i.e., the source is 3 arcmins off-axis). The results of this simulation are shown in Figure 5.15. A spike can be seen at approximately 40 keV because at this energy, the K-edge of Xenon occurs, which is where the K-shell electron interactions dominate. At photon energies less than 40 keV, the L-shell electron interactions dominate. The change to K-shell interactions corresponds to a change in the quantum efficiency of the detector [4]. In general, the Crab Nebula count rate is much higher than that of GRS 1915+105 due to the intrinsic nature of the sources.
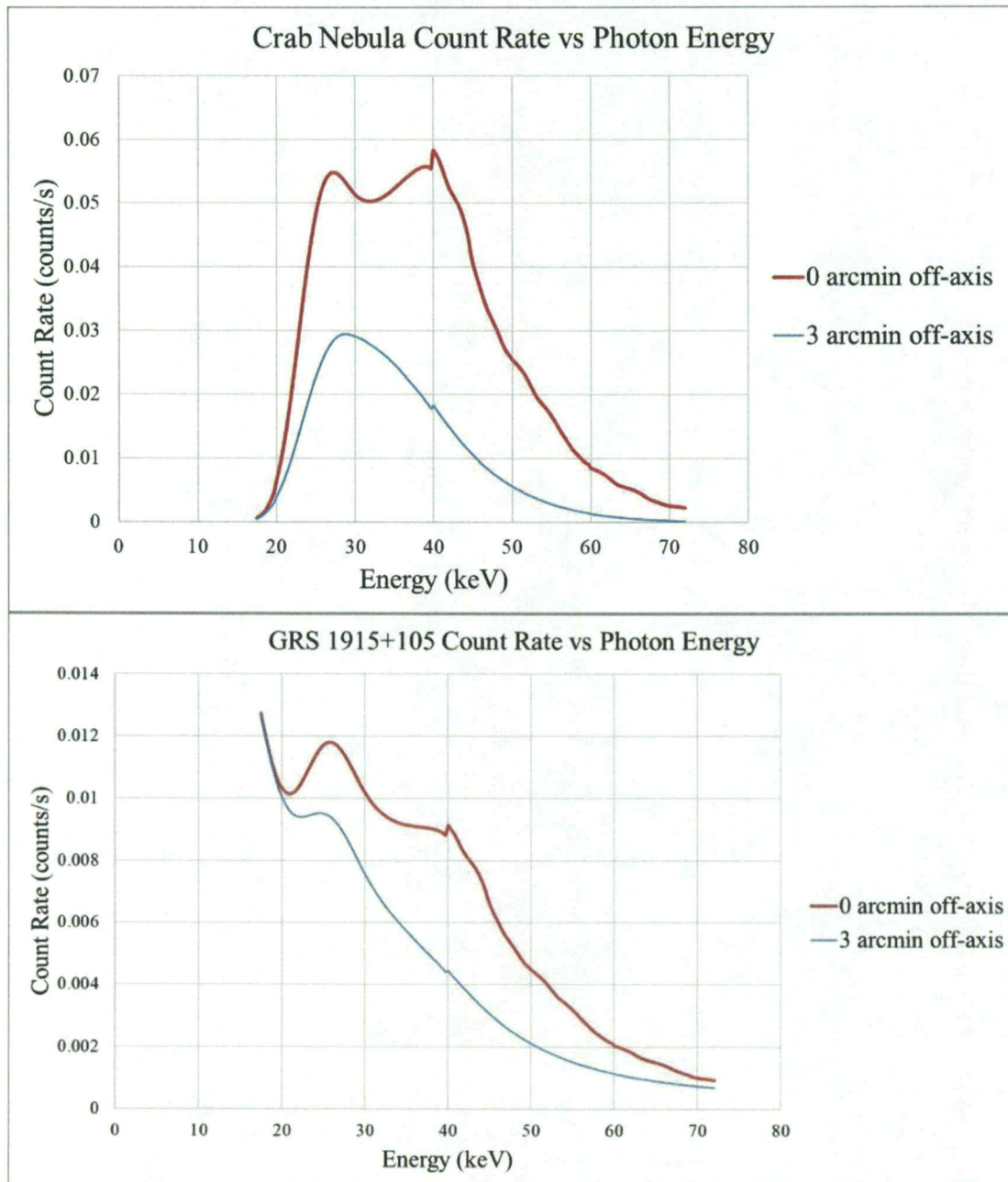
Figure 5.15: Simulation of the count rate vs the photon energy for the Crab Nebula (upper plot) and GRS 1915+105 (lower plot). The count rate vs photon energy is shown for no pointing error and for 3 arcminutes pointing error. The addition of a pointing error ensures that this source is not detectable by HEROES. The count rate decreases as the photon energy increases. Image credit: NASA/MSFC.

When the source is on-axis (where on-axis means that the source is centered on the payload's optical axis so the pointing error is ~ 0 arcminutes), the photon count for the Crab Nebula during the duration of the flight time should be ~1.3889 cts/s, while the source being off-axis by 3.6 arcminutes reduces the count rate to ~0.4583 cts/s. This amounts to a 66% decrease in the photon count rate by being off-axis as little as 3.6 arcminutes. For GRS 1915+105, the on-axis count rate should be 0.25 cts/s, while at 3.6 arcminutes off-axis this is reduced to ~0.0833 cts/s [4]. How the reductions in count rate affects the X-ray data collected from the sources is discussed in sections 5.5.2 and 5.5.3.

5.5.3 Crab Nebula Observation

The Crab Nebula observation took place at 02:05 to 05:01 Mountain Standard Time (MST) (08:05-11:01 UTC) on September 22, 2013. During the 4 hour observation, the payload was at an altitude that varied from ~34 km to ~36 km. This observation was done during the night, so there were minimal thermal variations throughout the payload, unlike during the GRS 1915+105 observation. During the observation, the BAMS optics flange rings all moved by approximately the same amount, but with an offset from one another as shown in Figure 5.16. This is more obvious in the Y-axis movement of the optics flanges ring. Over the course of the Crab Nebula observation, a displacement between the optics and detectors was determined to be approximately 0.6 arcmin along the X-axis and approximately 1 arcmin along the Y-axis. As mentioned in section 5.5.1, BAMS only aids the reconstruction process if there is misalignment between the optics and detectors. If there is movement of the optics and detector flanges during an observation, BAMS will not significantly improve the PSF of the reconstruction.
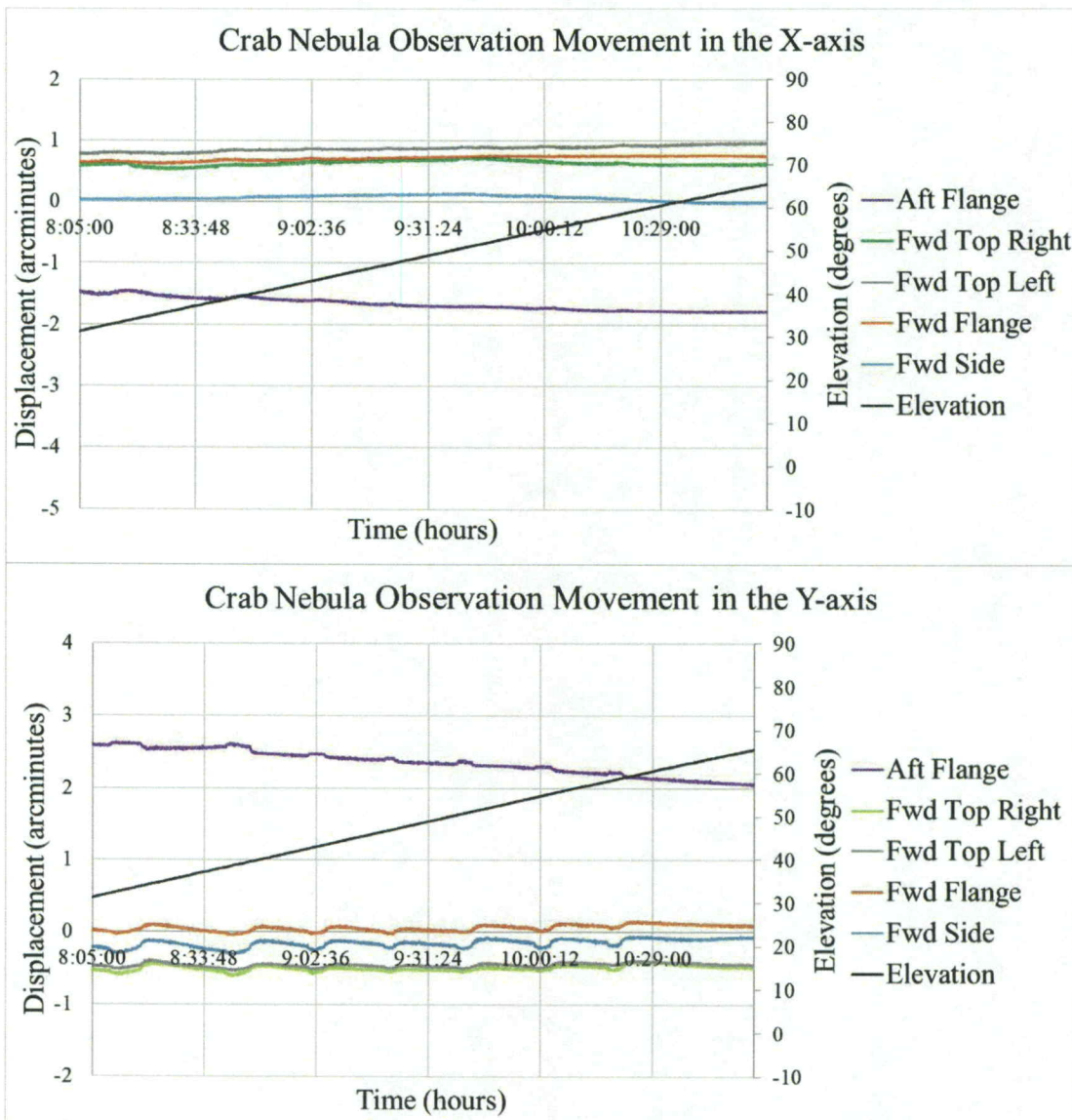
Figure 5.16: BAMS X-axis (Upper Plot) and Y-axis (Lower Plot) displacement results for the HEROES flight during the Crab Nebula observation. BAMS data for all LED rings attached to the HEROES payload are shown.

118

Images of the Crab Nebula reconstructed using the HERO_Soft software with and without the BAMS data are shown in Figure 5.17. The top image shows the Crab Nebula without the BAMS correction applied, which was fit with a Gaussian with a variance of 38.69 arcseconds. This corresponds to a PSF half power diameter (HPD) of the same value. The bottom image shows the reconstruction with the BAMS correction applied, and a Gaussian fit results in an HPD of 37.98 arcseconds. The bright red spot in both images is the Crab Nebula.

The optics modules used in the HEROES flight had an HPD of ~33 arcseconds, which is less than both reconstructions [4]. Potentially, additional alignment error could have been introduced if the locking-screws used to mount the mirror modules onto the optical bench loosened during launch. The shift in offset from ground alignment that the optics modules experienced could not be factored into the BAMS correction due to most of the modules not having an LED ring that could be monitored for movement. The offsets in alignment between each of the optics modules, along with the optics modules having an HPD of ~33 arcseconds, are most likely the reasons there was not a significant improvement in the width of the Gaussian fit for the reconstructed X-ray image of the Crab Nebula even with the use of the BAMS displacement data.
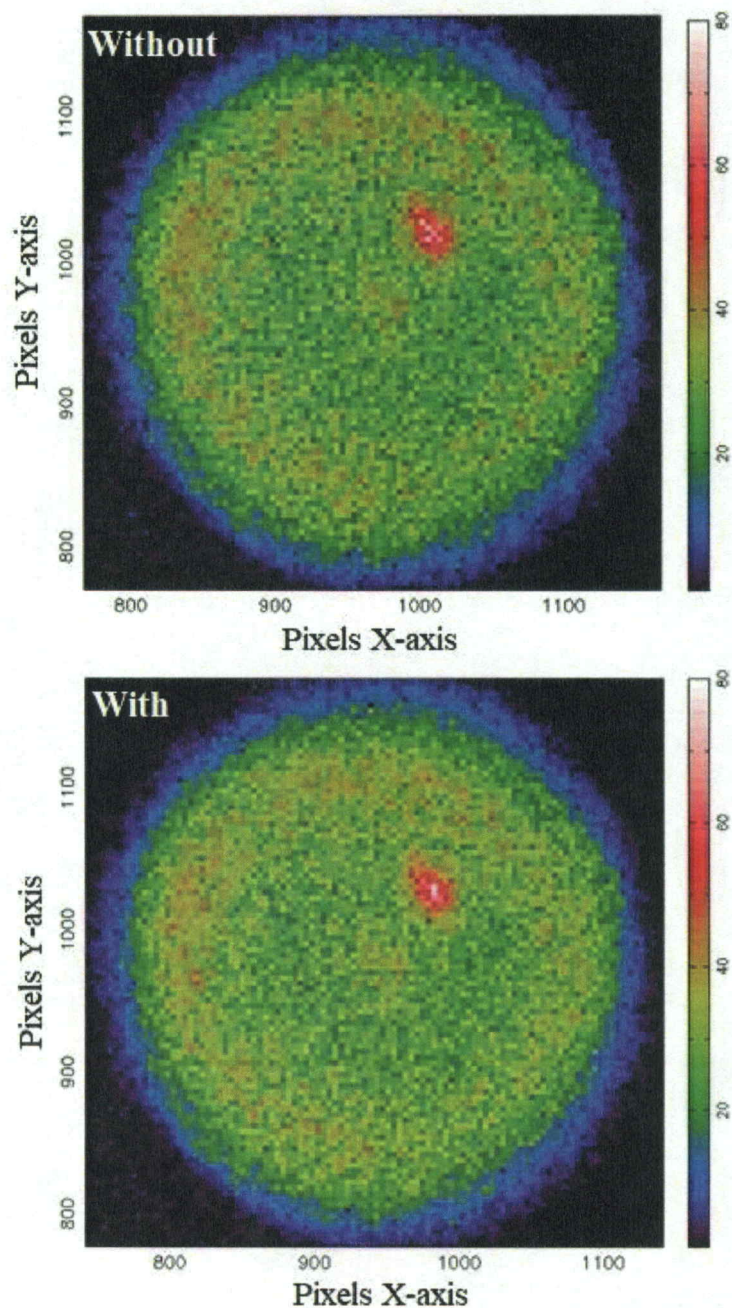
Figure 5.17: Reconstructed images of the Crab Nebula without (Upper Image) and with (Lower Image) the BAMS correction factored in respectively. The large red spot in both images is the Crab Nebula. The BAMS-corrected, reconstructed image of the Crab Nebula has a smaller PSF (less spread). The blue circle is due to background X-rays and the green is also due to background X-rays incident on the detector during the observation.

120

5.5.4 GRS 1915+105 Observation

The GRS 1915+105 observation took place between 16:57 MST (22:57 UTC) on 09/21/2013 to 00:14 MST (06:14 UTC) on 09/22/2013. During the observation, the payload altitude was between 34-38 km. The GRS 1915+105 measurement took place while the Sun was above the horizon, so there was a thermal gradient across the payload, which may have caused the displacement between the detectors and optics as shown in Figure 5.18. As the source was being observed, the Sun was shining on one side of the optical bench (top and starboard sides). From the data recorded by thermal sensors attached to the optical bench, post-flight assessment indicated there was a large thermal gradient on the optical bench during this time on the order of 50 Celsius. Once the Sun set, the payload cooled and the thermal gradient began to dissipate.
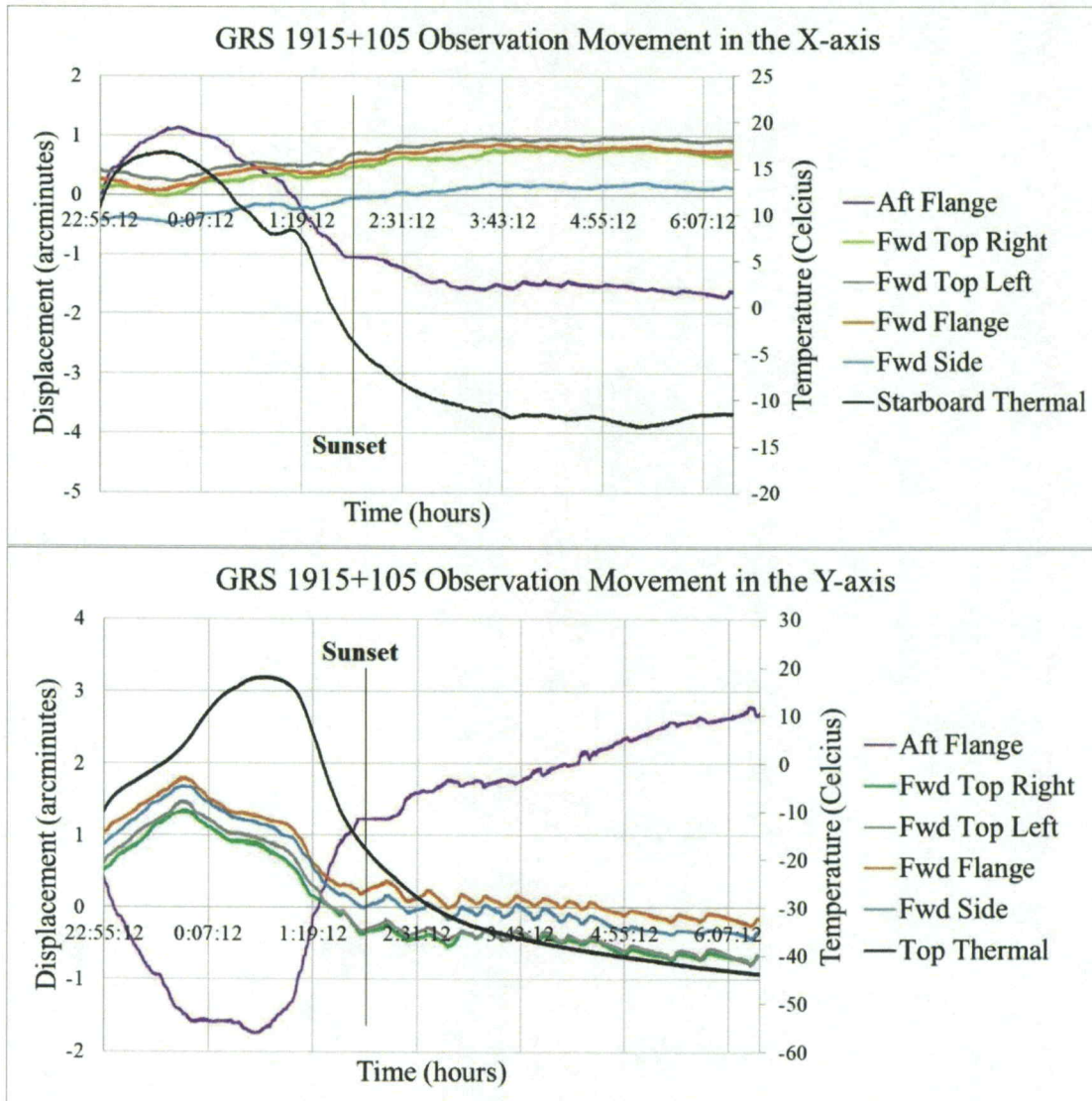
Figure 5.18: BAMS X-axis (Upper Plot) and Y-axis (Lower Plot) displacement results along with thermal data for the HEROES flight during GRS 1915+105 observation. Data for all LED rings attached to the HEROES optical bench along with thermal data are shown. A black line is shown where sunset occurs in the plots.

GRS 1915+105 is an X-ray source that fluctuates between high and low flux states over the HXR energy range. This means that during different times, the source will have a high or low flux as can be seen in Figure 5.19 from the SWIFT transient database, which has an energy range of 15-50 keV. Depending on the state, the GRS 1915+105 count rate can be as high as ~0.15 cts/cm^2/s and lower than ~0.01 cts/cm^2/s. During the GRS 1915+105 observation, the count rate was measured by SWIFT to be 0.038 cts/cm^2/s [53].
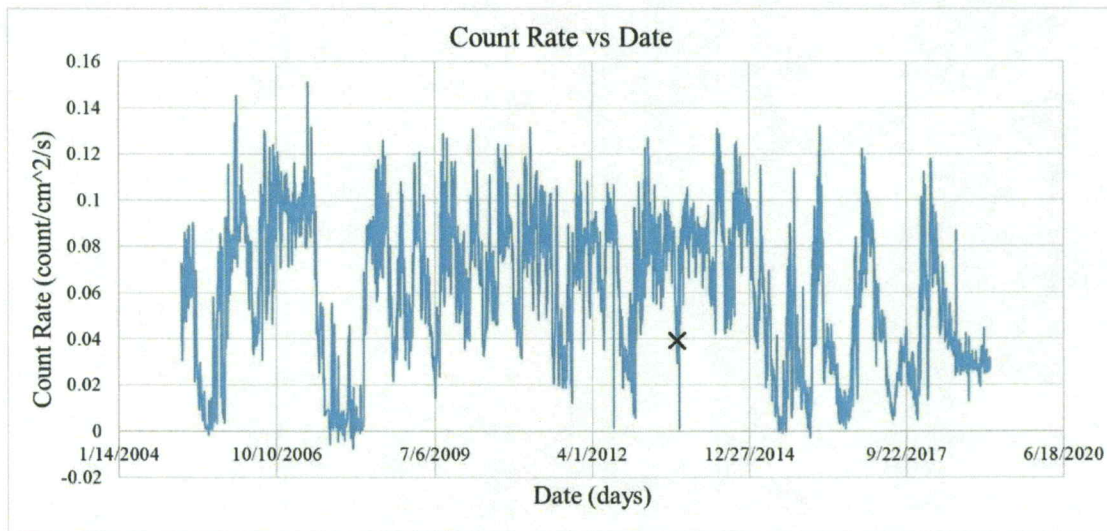
Figure 5.19: Count rate for GRS 1915+105 using the SWIFT database for 2005 – current day. The data shown comes from the SWIFT BAT transient monitor database. The black "X" signifies the date of the HEROES flight. [53]

During the HEROES observation, the source was in a low flux state over the HEROES bandpass. Along with the low flux, there was pointing error during the observation that further decreased the number of photons that could have been observed. The result of these combined factors was that the source flux of GRS 1915+105 was not observable by HEROES and thus could not benefit from BAMS reconstruction.

5.6 Chapter Summary

HEROES successfully launched on Sep 21, 2013 from Fort Sumner, NM. Over the course of the ~26 hour-long flight, HEROES observed the Sun, the Crab Nebula, and attempted an observation of GRS 1915+105. The BAMS data from the flight was processed through the BAMS software to obtain the relative displacement between the optics flange rings and the detector flange ring. The BAMS displacement results were then plotted against the payload recorded elevation and thermal measurements. The temperature versus BAMS displacement plots showed a major correlation between the thermal gradient across the payload and the displacement data reported by BAMS. This was most significant during the GRS 1915+105 observation when the payload had one of its sides exposed to the Sun. The BAMS cameras were temperature controlled and mounted to the elevation flange so if there had been thermal flexing of the elevation flange, the detector and optics flanges would have shifted as well because they are attached to the payload at the elevation flange. The payload elevation versus BAMS displacement plots showed a direct correlation in multiple places such as during the Crab Nebula observation and during the second half of both the GRS 1915+105 and solar observations. BAMS cannot measure tip/tilt very well so if this was a contributing factor to the displacement it could not be corrected for. This feature will be added to the system in the future.

The displacement of the optical bench obtained from BAMS was compared to the PYAS data during the solar observation. It was shown that the results are comparable, further validating the BAMS results during the astronomical observations and validating the fact that BAMS itself was most likely not the source of the movement/measured

displacement. The HERO_Soft software was used to analyze the X-ray data collected for the Crab Nebula and GRS 1915+105. The HERO_Soft software reconstructed the X-ray data from all eight detectors into a single image along with the spectrum.

Pointing error was shown to be ~3.6 arcminutes during the Crab Nebula observation. Pointing errors significantly decrease the photon count rate and this was seen in both astrophysical observations. The Crab Nebula data showed minor improvement when corrected with the BAMS data. Corrections consisted of applying offsets between each of the optics modules from ground alignment and the minimal movement of the optics and detectors flange. Obtaining reconstructed images of GRS 1915+105 was not possible due to the low source photon count caused by the off-axis source position.

Chapter 6

BAMS Hardware Selection and Future Work

6.1 Introduction

As shown in the previous chapters, the BAMS software is able to track an LED ring to give accurate optical axis alignment information for a flight mission. Each flight mission has unique BAMS hardware requirements such as: accuracy, ring size, weight, and placement in the payload. The LED pattern, cameras, lenses, object distance and LED wavelength were taken into consideration when deciding the setup of the BAMS system. Discussed in this chapter is how hardware choice played a role in the functionality of the BAMS software. Future work to be done will also be explored.

6.2 LED Pattern Selection

Choosing the correct LED pattern is one of the critical components of the BAMS setup, and is essential for accurate alignment information. As discussed in Chapter 3, the pattern selected must meet the conditions of being asymmetric and nonrepeating, but there are no restrictions on the shape of the pattern itself. Although a particular ring was selected for use on the HEROES payload flight, multiple shapes and patterns would function as well. Any design has to fit into a 256 pixel square box when processed through the BAMS software (Figure 6.1).
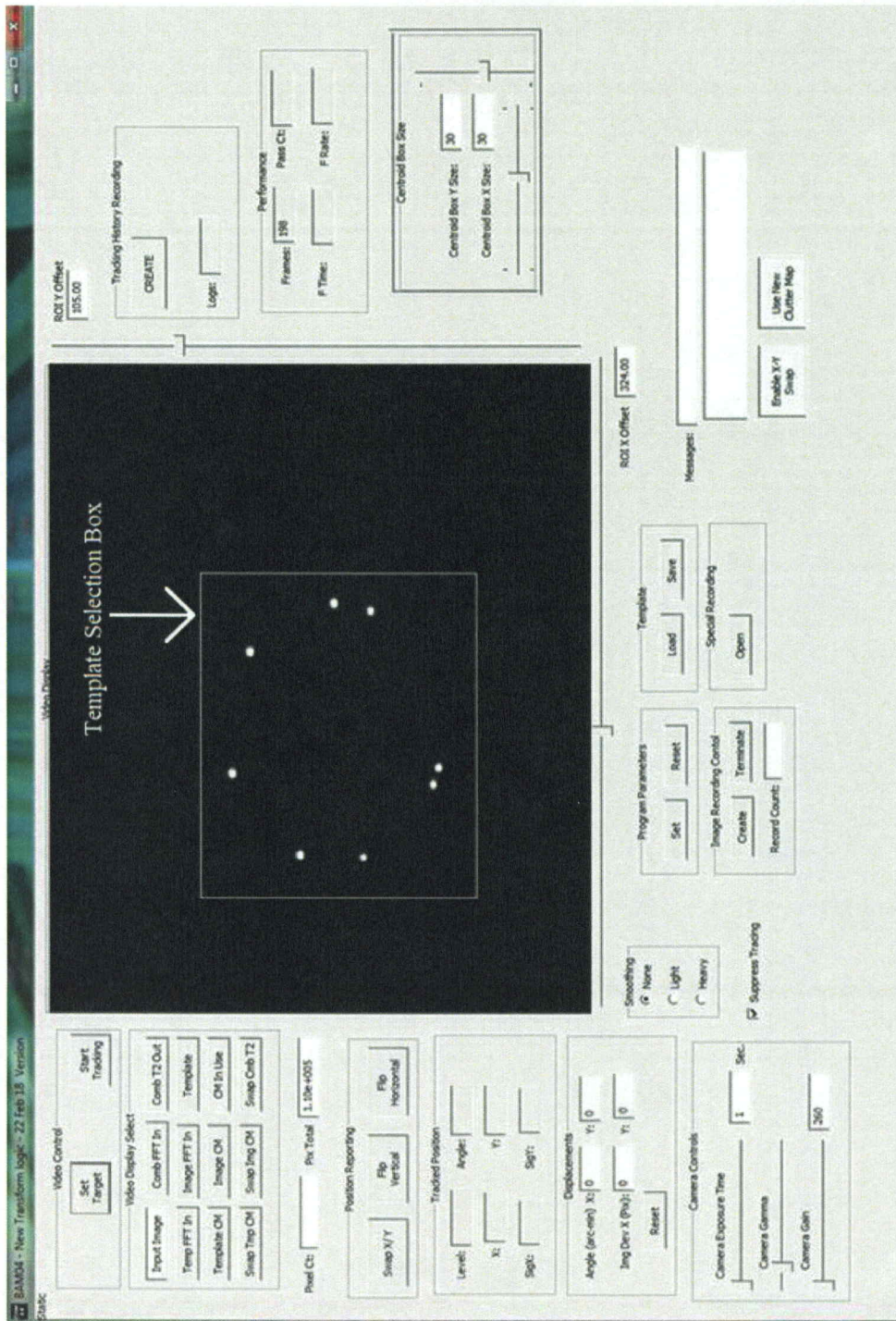
Figure 6.1: The BAMS Graphical User Interface with an LED ring target image displayed. The white square around the LED ring is the template selection box that allows a user to select the target to track.

The most important part of designing any such pattern, aside from the constraints mentioned above, is ensuring the spacing of the cross-correlation for the LEDs do not interfere with the cross-correlation of the overall pattern. A MATLAB simulation was done to demonstrate how LED separation in the reference target affects the end result of the JTC. A composite scene was created with two identical LED rings which had a small separation between two of the LEDs in each ring (Figure 6.2). The JTC produced the bottom image in Figure 6.2, which shows the cross-correlation of the LED ring pattern. On either side of the LED ring cross-correlation are the cross-correlations of the LEDs. This simulation demonstrates the importance of the separation between any two LEDs. choosing carefully keeps the LED cross-correlations from interfering with the subpixel centroiding that is done on the LED pattern cross-correlation.
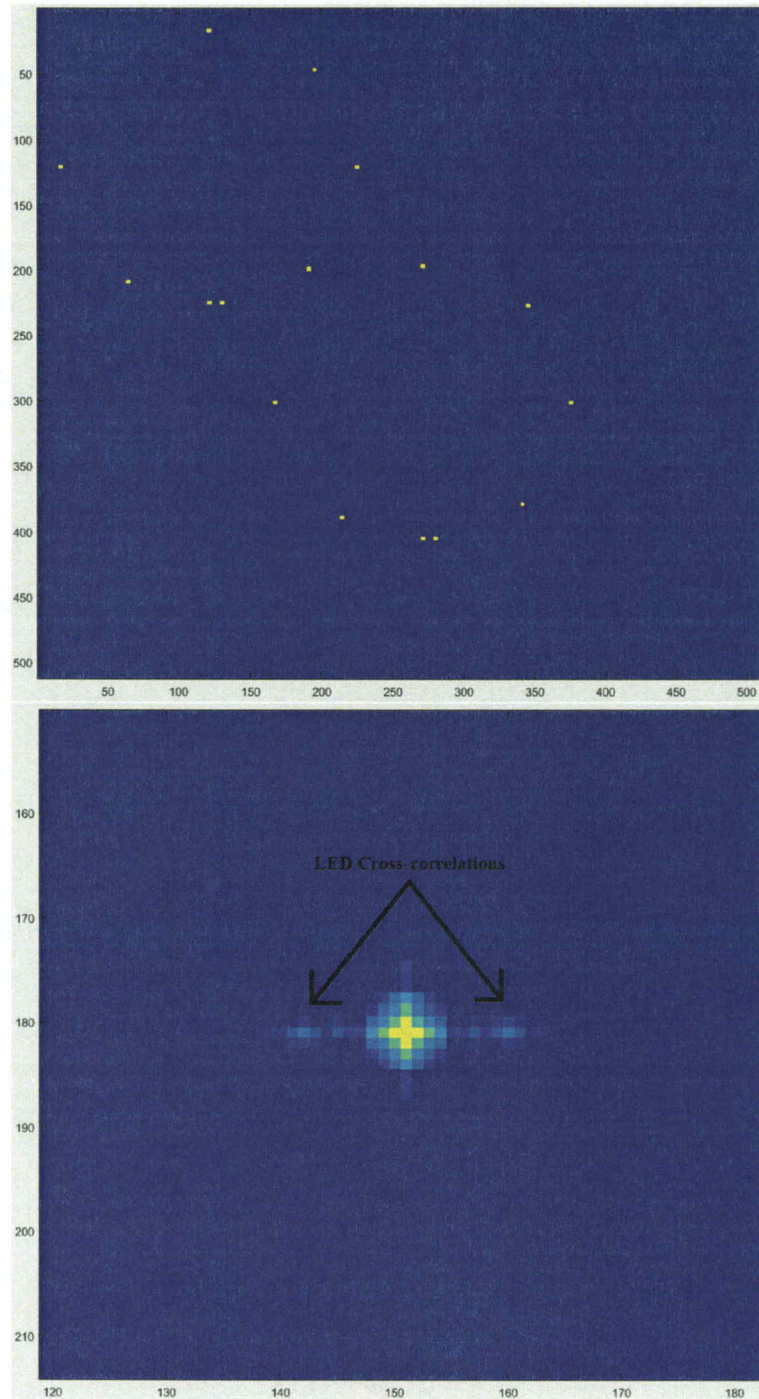
Figure 6.2: BAMS simulation of two LED rings with two LEDs in the ring placed close together. The top image shows the composite scene used with two LED rings that have a separation between two individual LEDs in each ring slightly larger than the led ring cross-correlation diameter. In the bottom image the JTC process has been done and the cross-correlation of the LEDs in close proximity can be seen on either side of the pattern cross-correlation.

Another simulation was done to further demonstrate how LED separation impacts the JTC. Two composite scenes were constructed that contained two concentric LED rings as the main target, and a set of two identical concentric rings placed in the same image a known distance away (Figure 6.3). The first composite scene consisted of two sets of concentric rings with the radius of the outer ring being 104 pixels, and the radius of the inner ring being 78 pixels. The second composite scene consisted of two sets of concentric rings with the radius of the outer ring being 104 pixels, and the radius of the inner ring being 97 pixels. The second test scene placed the rings closer together, this was to demonstrate how having two LEDs in close proximity can affect the results.
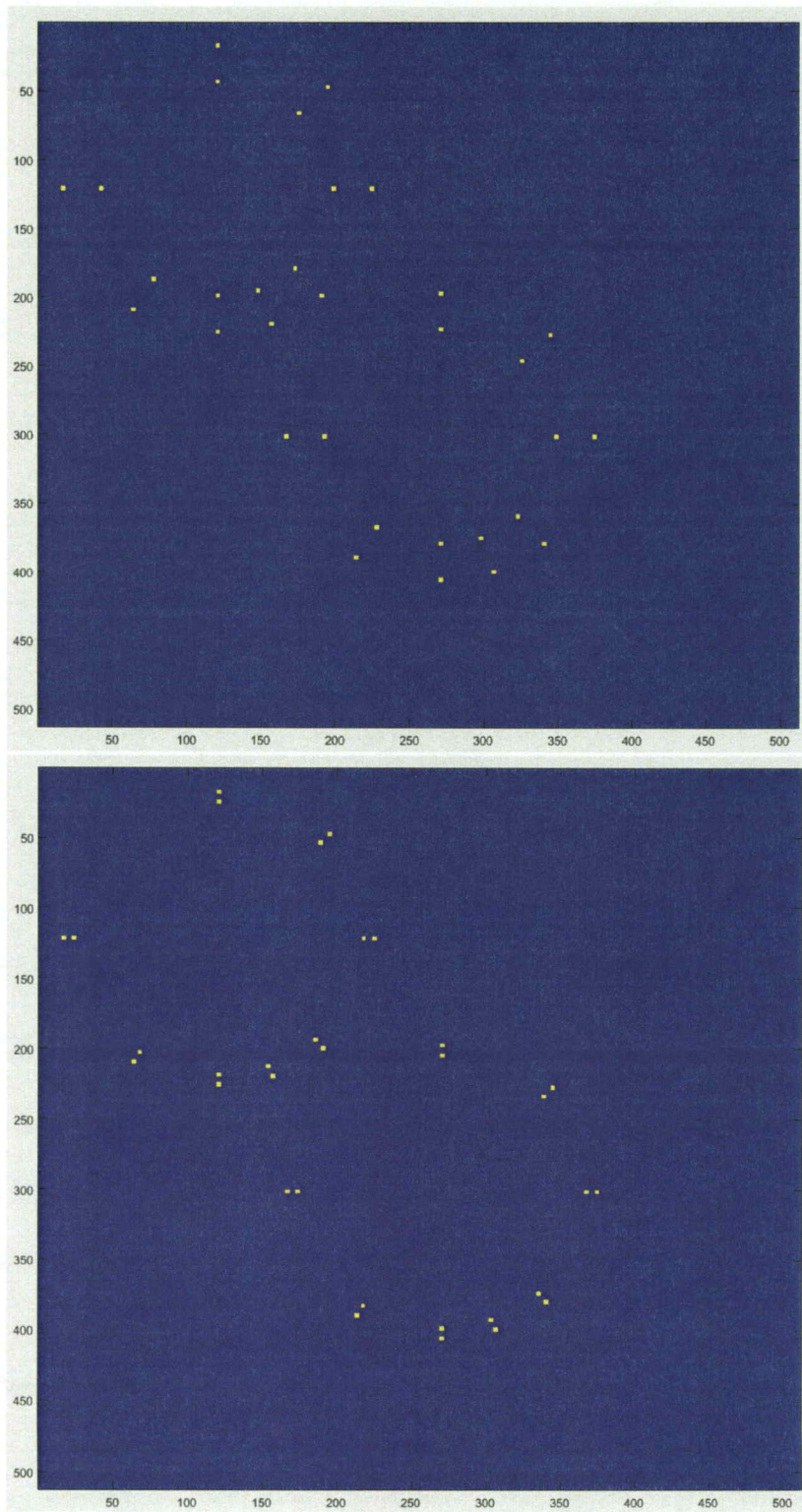
Figure 6.3: Images of the test scenes used in the MATLAB simulation to demonstrate how placement of the LEDs has an effect on the JTC results. The images consist of two sets of concentric LED rings that are separated by a known distance.

The test scenes were then analyzed through the JTC process to produce second transforms which contained cross-correlations of the LED ring patterns, cross-correlations of the individual LEDs, and an autocorrelation signal. The second transforms for the top and bottom images in Figure 6.3 are respectively shown below with the top and bottom images in Figure 6.4. As it can be seen in both second transforms, the LED cross-correlation spots encircle the ring cross-correlation spot. The LED cross-correlations are much closer to the ring cross-correlation in the second transform of the test scene, where the concentric LED rings are closer together.
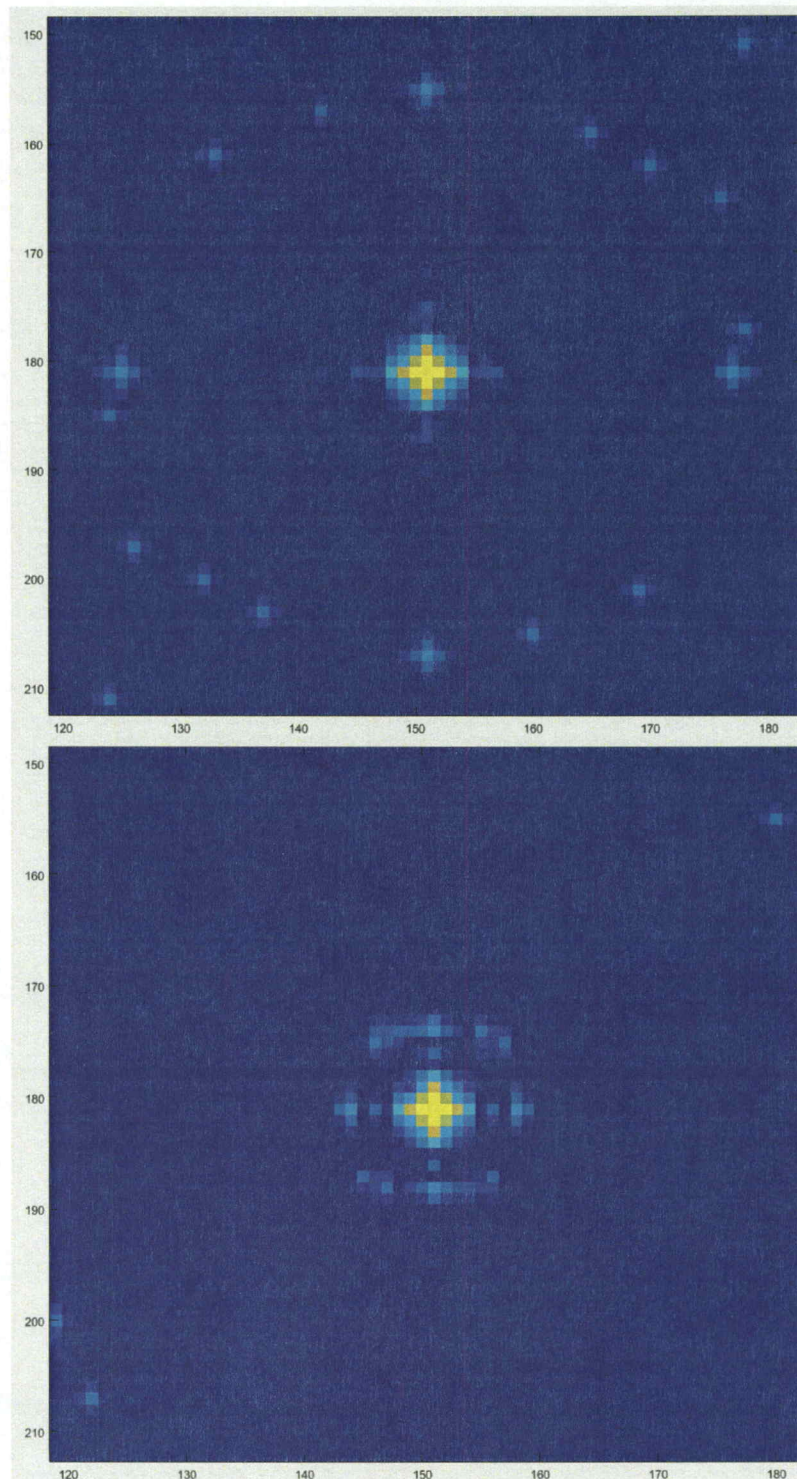
Figure 6.4: The second transform cross-correlation spots for the test scenes shown in the top and bottom images respectively in Figure 6.3. The LED cross-correlation spots in the top images are farther away from the ring cross-correlation spot than the bottom image where the LED cross-correlations spots are close to the ring cross correlation.

The results of the simulations show that the farther apart the LEDs are in the ring the better the results of the JTC. This is because the LED cross-correlations spots are outside the radius of the LED ring cross-correlation spot, so they do not interfere with the subpixel centroiding results. The separation between two LEDs in the same LED ring determines the distance the LED cross-correlations will be from the LED ring cross-correlation spot. It is essential to have the distance between any two LEDs in the same ring be farther apart than the size of the LED ring cross-correlation spot.

6.3 Camera and Lens Selection

Along with selection of a suitable LED pattern, the choice of camera and lens plays an important role in the BAMS setup. As mentioned in the previous section the pattern must fit into a 256 pixel square box specified in the BAMS software. The lens and camera selection play major roles in determining the size of the LED pattern that can be created. Selection of a camera with a small pixel size and a lens with a longer focal length provides a better overall resolution for BAMS. Presented in Table 6.1 are different camera and lens combinations which show how the plate scale (arcsec/pixel) changes with each as calculated using Equation 3.1. As the focal length increases and the pixel size decreases, resolution of the BAMS system improves.

Table 6.1: Resolution (plate scale) for combinations of pixel sizes and lens focal lengths.

	Lens focal length 16 mm	Lens focal length 35 mm	Lens focal length 50 mm	Lens focal length 75 mm	Lens focal length 100 mm
Pixel size 1.67 micron	21.529 arcsec/pixel	9.842 arcsec/pixel	6.889 arcsec/pixel	4.593 arcsec/pixel	3.445 arcsec/pixel
Pixel size 2.2 micron	28.361 arcsec/pixel	12.965 arcsec/pixel	9.076 arcsec/pixel	6.05 arcsec/pixel	4.538 arcsec/pixel
Pixel size 4.65 micron	59.945 arcsec/pixel	27.404 arcsec/pixel	19.183 arcsec/pixel	12.788 arcsec/pixel	9.591 arcsec/pixel

There are multiple factors such as Field of View (FOV), resolution, and LED ring size that determine what lens/camera combination should be used in the system. If there are multiple X-ray optics modules to be tracked for alignment like there were on the HEROES flight, then a larger FOV is necessary. Depending on the accuracy needed for the mission, a longer focal length and smaller pixel size are required to obtain a better plate scale, which will yield higher tolerances. The LED ring size and optical distances required for the mission also determine the lens and camera combination. For example, the HEROES flight had LED rings that were clamped around the X-ray optics modules that were 3 m away from the CCD, so a shorter focal length and larger CCD pixel size were needed. BAMS hardware must be tailored for each specific flight mission. Minor aberrations in the camera lens were not a concern for BAMS due to the small displacements that occur on a flight mission. The BAMS system takes residual lens aberrations into account with an initial zeroing of the displacement value.

6.4 Maximum LED Ring Size

The object distance and the resolution of the BAMS camera/lens setup determines the maximum possible LED ring size. The maximum ring size is directly proportional to the length of the optical axis, so a longer optical axis allows for a larger LED ring to be used. If the ring is too large, the LEDs will not fit into the required 256 pixel square box in the BAMS software. Maximum LED ring size is determined by the following equation

$$Ring\ size\ (mm) = tan\left(\frac{256\ pixels * resolution\left(\frac{arcseconds}{pixels}\right)}{3600\frac{arcseconds}{degree}}\right) * distance\ (mm) \qquad (6.1)$$

Resolution is the plate scale (arcsec/pixel) of the system (which was described in Chapter 3) and the distance is the length between the CCD and the LED ring (object distance). To demonstrate how the lens focal length and length of the optical axis affect ring size, Table 6.2 lists the maximum ring size for a 2.2 micron pixel size CCD with a combination of different focal length lenses and optical axis lengths. As the length between the CCD and the LED ring increases for each lens, the maximum ring size also increases.

Table 6.2: Maximum ring size for a combination of optical axis lengths and lens focal lengths using a CCD with a 2.2 micron pixel size.

Object Distance	16mm lens	35 mm lens	50 mm lens	75 mm lens	100 mm lens
3 m	105.6 mm	48.3 mm	33.8 mm	22.5 mm	16.9 mm
5 m	176.1 mm	80.5 mm	56.3 mm	37.5 mm	28.2 mm
10 m	352.1 mm	160.9 mm	112.6 mm	75.1 mm	56.3 mm
15 m	528.2 mm	241.4 mm	169.0 mm	112.6 mm	84.5 mm
20 m	704.3 mm	321.9 mm	225.3 mm	150.2 mm	112.6 mm

6.5 Changing Object Distance

Changing the object distance also changes the size of the LED ring as used by the BAMS software (due to the LED ring moving closer to or farther away from the CCD). Changing object distance affects BAMS performance because the JTC is not scale invariant. To determine how changing the length of the optical axis affects the results, a test was performed that involved changing the object distance between the LED ring and the CCD. The test was conducted on an air bearing table in an environmentally controlled room (shown in Figure 4.8).

The CCD was attached to a stage that allowed the object distance to change. The object distance was increased in steps of 2 inches from an initial starting point. As the distance increased, the LED pattern cross-correlation spot spread into individual LED cross-correlations, as can be seen in Figure 6.5. The central spot disappeared as the image of the test LED ring increased in diameter (as seen by the BAMS software). This is due to the reference and test LED rings not overlapping when the images are processed by the JTC.
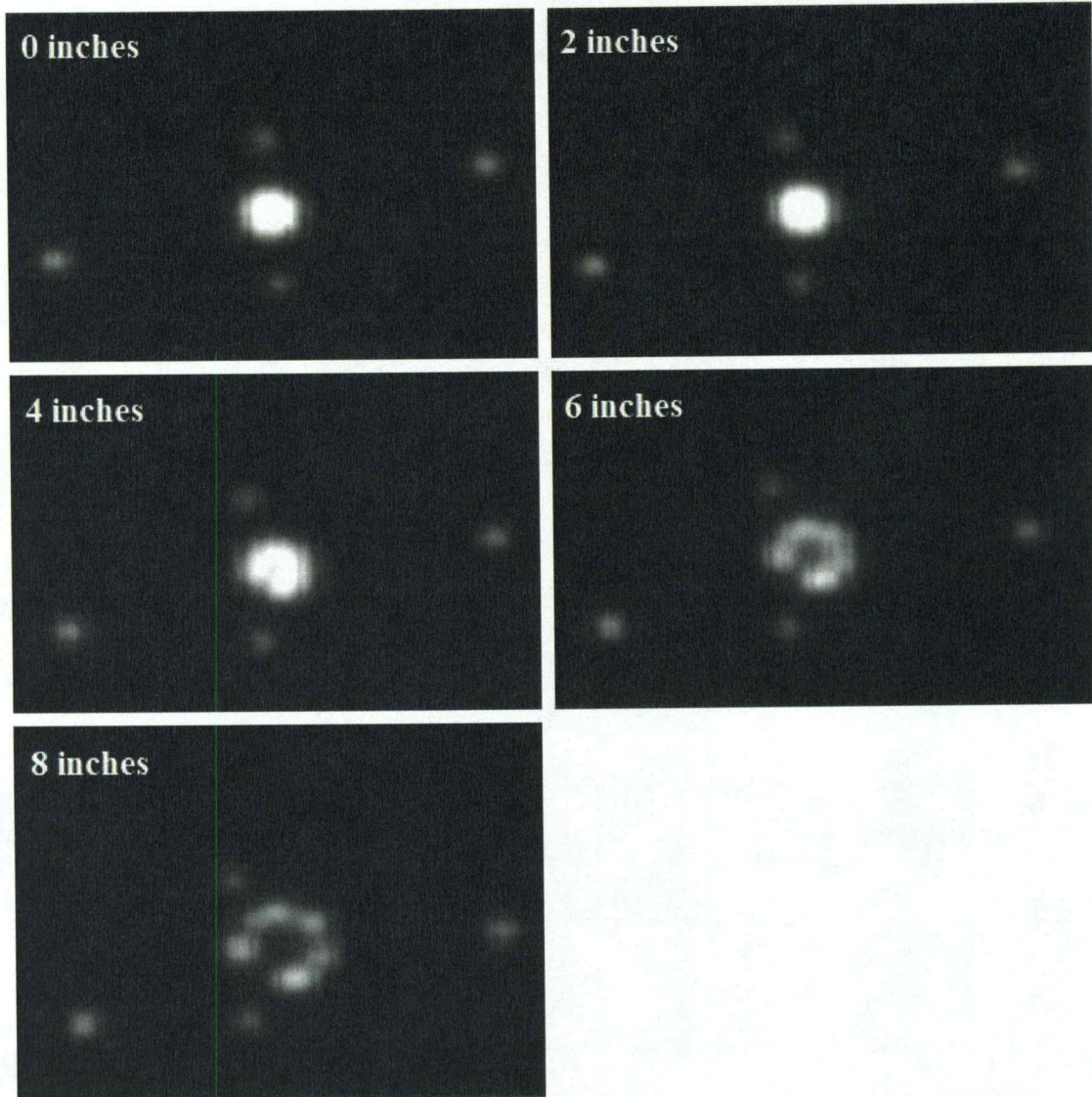
Figure 6.5: JTC second transform LED ring cross-correlation spot for a changing object distance. The object distance changed in increments of 2 inches per image. As the separation length increased, the cross-correlation spot begins to spread from the center.

6.6 LED Wavelength Choice

The wavelength range a mission is observing determines what wavelength LEDs should be used for the BAMS rings. The science goals thus determine what wavelength of LEDs and subsequently what type of camera should be used during the flight. BAMS is fully functional with UV, IR and visible LEDs as long as a monochrome FITS image file is provided for BAMS software analysis. For example, the BAMS flight NIR LEDs were selected due to the lower IR photon count (when compared to the visible photon count) coming from the Sun that could cause stray light to affect the BAMS results. In the GHAPS flight mission, UV LEDs were to be used because IR and visible LEDs would interfere with the science goals of the mission.

6.7 Future Work

Further work will be done to improve and test the capabilities of the BAMS software so that it may be considered for future missions. There are multiple improvements that can be made, such as adding the capability to obtain tip/tilt data for a payload, the capability to determine a changing object distance, and determining optimum ring patterns.

6.7.1 Tip and Tilt Measurements

Features to be added include tip and tilt (pitch and yaw) measurements along with displacement measurements. Tip and Tilt information can be obtained by observing how the LEDs change in size in the X-axis and Y-axis as the payload changes in tip/tilt. This test can be done by attaching an LED ring to a goniometer and moving the ring by a

139

known amount. By observing how the LEDs change in size, an algorithm can be created to correlate the LEDs change in size to movement in pitch and yaw.

6.7.2 Changing Optical Distance

As mentioned in section 6.5, a change in object distance will change the size of the LED ring as seen by the BAMS software. Determining the distance between the CCD and the LED ring as they move away from each other would be useful on flight missions that have an extending boom or a rocket booster that has separated. Determining object distance changes can be accomplished by detecting the apparent size of the LED ring as it moves away from the CCD and correlating this to the distance the ring has moved. Tip and tilt measurements would need to be factored into this calculation as well, because a change in tip/tilt would change the apparent size of the ring. This effect would need to be compensated for before the ring size can be calculated. The JTC would not be used in this calculation so scale invariance would not be a factor.

6.7.3 LED Ring Patterns

Although LED rings were used on the HEROES flight mission there is no requirement that a ring pattern must be used. Other patterns would potentially work equally well such as a box or a star pattern. Other patterns will be tested in the future to at least qualitatively determine the general shape that performs best.

6.7.4 SuperHEROES LED Ring Pattern

The SuperHEROES mission will be the successor to HEROES and will be a long duration balloon-borne flight. Presented in Figure 6.6 below are two prototype LED patterns that will be investigated for use on the SuperHEROES flight. The left image is a spoke wheel LED ring pattern and the right image is concentric circles that are rotated with respect to each other. Both of these patterns will be built and tested. They should produce the same size cross-correlation signal. Using concentric LED rings over a single LED ring will increase the correlation signal.
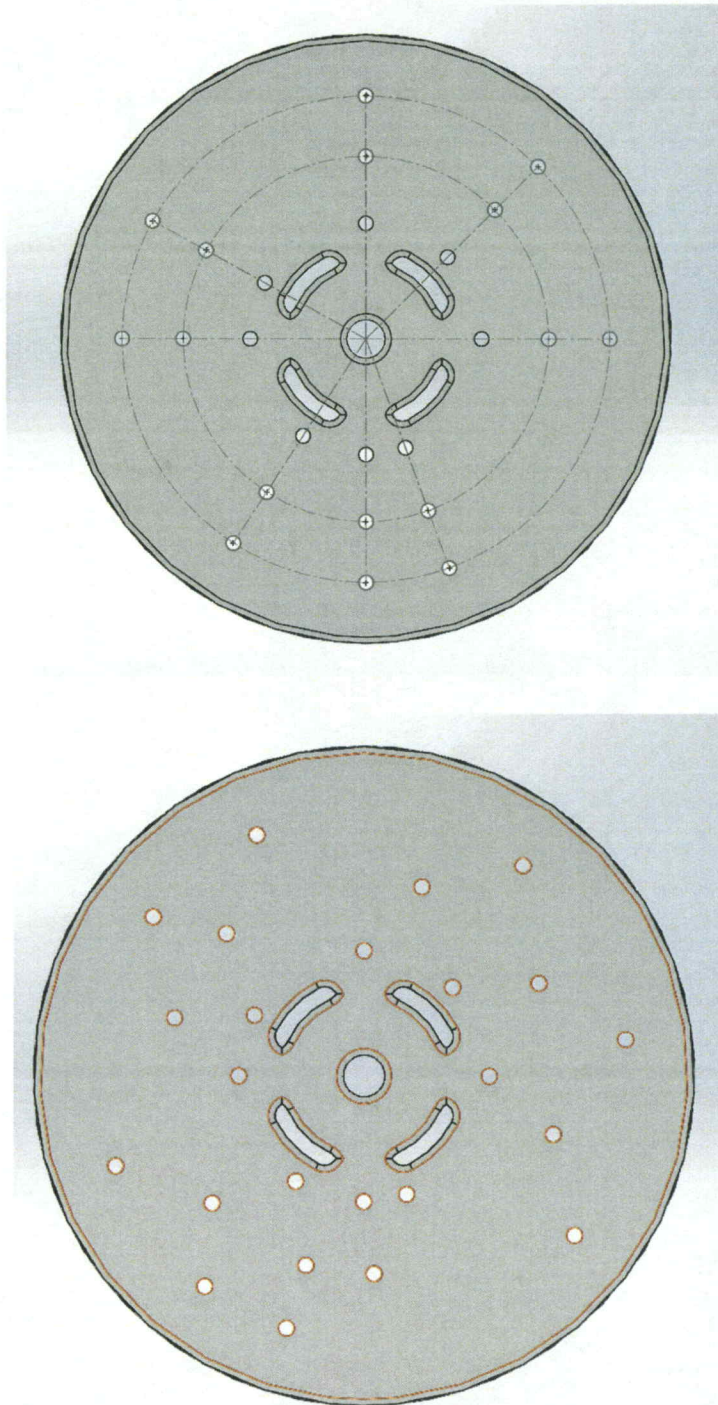
Figure 6.6: Prototype LED ring patterns for use on the SuperHEROES flight mission. Each ring has three concentric LED rings. The top image has the rings in the same orientation but at different radii. In the bottom image the rings are rotated with respect to each other along with having different radii.

6.8 Chapter Summary

The LED pattern can be in almost any shape as long as it is nonrepeating, asymmetric, and the LEDs are farther apart than the diameter of the cross-correlation spot. The accuracy required for a payload determines the pixel size and lens focal length selected. Both of these factors determine the resolution of the system. A smaller pixel size and longer focal length results in better resolution and accuracy. The length of the payload and the plate scale determine the maximum LED ring size that can fit into a 256 pixel square box in the BAMS software. A change in object distance will increase or decrease the LED ring size as seen by the BAMS software and substantially affect the JTC cross-correlation spot. The BAMS setup works with any wavelength as long as a monochromatic FITS file image is provided to the software, and the wavelength does not interfere with the science goal of the flight mission. Future work will be done to add capabilities to the software such as determining tip/tilt and distances.

Chapter 7

Conclusion

The primary objective of this investigation was to demonstrate the Benchtop Alignment Monitoring System (BAMS) viability for use on suborbital (and space-based) missions that require maintaining high precision alignment between critical payload elements, such as X-ray mirror assemblies and their detectors. The testbed for BAMS was the High Energy Replicated Optics to Explore the Sun (HEROES) suborbital, balloon-based telescope, which uses X-ray optics to focus hard X-rays (20-70 keV) onto complementary detectors. In general, focusing hard X-rays requires the use of very shallow angles to focus the photons, critical angles that are on the order of a few arcminutes, which makes them very sensitive to certain misalignments that can significantly impact the scientific data collected. A system, such as BAMS, that can provide information on these misalignments during flight improves post-flight data reconstruction and enables a more robust future design of the payload. Ultimately, BAMS could provide real-time misalignment data for in-situ corrections and realignments of payload elements for improved data acquisition.

The design of BAMS had to be such that it could be incorporated into the existing HEROES payload. This condition constrained the design and the requirements of the BAMS system. BAMS consisted of two cameras mounted on the elevation flange of the

HEROES optical bench and Near-Infrared (NIR) LED rings mounted to three of the optics modules, the optics flange and the detector flange. BAMS acquired images of these rings throughout the flight to determine misalignment as a function of time, such that the BAMS software reported post-flight corrections could be applied to the image reconstruction of the observed astronomical sources.

The BAMS software was initially written by Mr. John Jasper (self-employed) as an adapted version of a star tracker, and modifications were made to the software throughout this effort. The BAMS software operates by using a composite scene comprised of a reference LED pattern selected by the user and a test ring. BAMS uses the Joint Transform Correlator (JTC) operation to track movement between the two LED rings in the test scene. The JTC produces an image that contains a cross-correlation signal from the two LED rings that is monitored for movement to determine the misalignment of the payload. The cross-correlation signal is centroided for subpixel alignment information to obtain even more accurate misalignment data. The JTC calculation is done using Nvidia's GPU processing capability, providing faster processing of images over conventional means.

A simulation of the JTC was done in MATLAB to verify the results generated with the BAMS software and an LED ring. The simulation indicated that an incorrect Nvidia Fast Fourier Transform (FFT) was being used for the BAMS software. The Real to Complex (R2C) transform was used for the first transform because it was believed that the resulting (Fourier transform) image would be symmetric. The R2C provided half of the Fourier transformed image, which was copied to the other half of the image. By only using half of the transform, a substantial amount of data was being lost because of

approximation errors associated with the Nvidia FFT software. A correction was made by using the Nvidia Complex to Complex (C2C) FFT, which supplied a full image for the first Fourier transform.

After the correct FFT was implemented, the BAMS software was tested to characterize the systematic error present in the system. The total systematic error for BAMS was 1.02 arcseconds, well below the 35 arcsecond requirement for the HEROES flight. After benchtop testing verified the systematic error, the system was integrated onto the HEROES payload for testing. Two "hang tests" were done at the CSBF facility in Fort Sumner, NM, where the payload was lifted using a crane and the telescope was cycled through the full range of its elevation capability multiple times to test BAMS's ability to track changes in alignment of the mirrors to the detectors. The hang tests confirmed BAMS's ability to track payload misalignments in both the X-axis and Y-axis and verified that the system was ready to be used on the HEROES flight.

HEROES was a balloon-borne flight mission to obtain high-resolution hard X-ray images of the Sun, the Crab Nebula, and GRS 1915+105. The HEROES telescope was the successor to the HERO telescope and used heritage hardware along with several hardware upgrades such as the Solar Aspect System (SAS), BAMS, etc... The SAS contained two subsystems: the Pitch Yaw Aspect System (PYAS) and the Roll Aspect System (RAS), which were used to monitor the alignment of the HEROES optical bench during solar observations along with BAMS. BAMS's role was to monitor the alignment of the optics and detector flanges to obtain misalignment information for reconstruction of the hard X-ray data taken during the HEROES flight.

HEROES was launched on Sep 21, 2013 and the flight lasted approximately 26.5 hours, during which the Crab Nebula, GRS 1915+105, and the Sun were observed. During the course of the HEROES flight, BAMS images were taken every three seconds, to be analyzed post-flight. The BAMS images were processed to obtain linear misalignment information along the X- and Y-axes between the optics and detectors.

Misalignment data from the optics flange rings indicated that the rings attached to optics modules moved independently from the ring attached to the optics flange. The difference in movement of the optics module rings was potentially due to movement in the mounts that attached the optics modules to the optics flange, which were used for alignment during launch. Once at float altitude, the LED rings mounted to the optics modules all followed the same movement as a function of time, but each ring had a different offset from what was recorded during alignment on the ground prior to launch.

The BAMS flight misalignment data between the optics and detectors was compared to the telescope elevation and thermal measurements recorded by the HEROES House Keeping (HK) data that was taken during the flight. The BAMS data, when compared to the elevation data, showed that there was a direct correlation between the optical bench changing elevation and the amount of misalignment experienced and it was most apparent during the Crab Nebula observation and during the second half of the GRS 1915+105 observation (when thermal gradients from the Sun across the optical bench had dissipated). The HK data also showed that there was a thermal gradient experienced by the optical bench that most likely caused large deviations in the optical bench alignment, as reported by BAMS, especially during the GRS 1915+105 observation when the payload had its side exposed to the Sun. The BAMS cameras were held thermally stable

during the flight using heaters so there is minimal chance of the cameras contributing to the large misalignment seen.

The BAMS flight misalignment data was also compared to the relative misalignment data obtained by the PYAS subsystem during the solar observation. These independent systems agreed with each other, strengthening the supposition that movement of the BAMS hardware elements was not the cause of the observed misalignments.

The X-ray data collected for the Crab Nebula and GRS 1915+105 was reconstructed and analyzed using the HERO_Soft software created by Dr. Allyn Tennant (NASA MSFC). Reconstruction of the X-ray data is achieved when the astronomical source data is combined from all eight HEROES detectors into a single image along with the spectrum. The reconstruction depends on the number of incident photons while the number of photons collected during an observation is directly influenced by pointing error.

Misalignments between the optics and the detectors impact the post-flight data reconstruction by linearly shifting source X-rays away from the center of the detector focal plane and/or by decreasing the count rates from the observed source. There are three types of misalignments that can affect image reconstruction and they are rotational, lateral, and angular misalignments. A rotational misalignment occurs when the optics modules, detectors or the flanges are rotated from their original aligned position. Rotational misalignment of an optics module has minimal effect on the observation of the source; however, if either of the flanges or any of the detectors were to rotate as a function of time over the course of an observation it would appear as movement of the

source X-rays on the detector. A lateral misalignment results in a similar shift in the position of the observed X-ray source on a given detector or detectors. The GSPC detectors do not have a uniform response, so as the source moves farther from the center of the detector there are distortions. BAMS tracks the LED rings as they change position over time so correction for lateral misalignment is straightforward using BAMS data. The third misalignment and most difficult to correct is an angular misalignment of the optics modules or flange. Angular misalignments can severely reduce the observed count rate from an X-ray source. Angular misalignments also cause aberrations in the observed X-rays in the form of coma. These misalignments are indistinguishable from HEROES telescope pointing errors.

The HEROES aspect (telescope pointing) system used a star camera, which was mounted on the outside of the optical bench. If the star camera is not perfectly aligned with the telescope axis, pointing errors will occur. The star camera and telescope were aligned on the ground prior to launch, but it is likely they became misaligned during flight, possibly due to larger than expected thermal gradients across the payload. Pointing errors caused a significant reduction in the photon count from the astrophysical sources observed during the HEROES flight.

Following observations of the Sun, the first astrophysical source observed during the HEROES flight was GRS 1915+105. The GRS 1915+105 source goes through periods of high and low flux. During the observation, the Sun was above the horizon and the payload was oriented such that only one side of the telescope was heated. It is believed that this uneven heating caused substantial flexure in the aluminum half of the optical bench. Reconstruction of this hard X-ray source was not possible due to multiple

factors: the flux of the source being in a low state at the time of observation, with a count rate of 0.038 cts/cm2/s and the pointing of the optical axis being off by 3.6 arcminutes. This pointing error resulted in a significantly reduced count rate (by approximately 66%). Combined with the already low intrinsic count rate, this resulted in a flux that was not observable by HEROES. Therefore, no reconstruction was possible.

The second astrophysical source observed was the Crab Nebula. The source was observed while the Sun was below the horizon, which meant there were minimal thermal gradients across the optical bench, unlike the GRS 1915+105 observation. The Crab Nebula unlike GRS 1915+105 had a flux large enough for reconstruction of the X-rays.

Analysis of the reconstructed Crab Nebula X-ray data indicated that the telescope was not well aligned to the star camera. The pointing error was shown to be ~3.6 arcminutes which means that there was a significant decrease in the number of photons being focused from the source. The Crab Nebula X-ray data was reconstructed with and without the use of BAMS. With the BAMS correction applied, the Gaussian fit had a width of 37.98 arcsec while without the BAMS correction applied the Gaussian fit had a width of 38.69 arcsec. The improvement is small but could be significant in future missions. The small decrease in Gaussian fit was due to the HEROES payload setup and not the ability of BAMS to track the alignment of the optical bench.

There were multiple hardware design elements that had to be taken into consideration when designing BAMS for HEROES. The LED pattern is critical for the system to function correctly and it was designed to have a nonrepeating and asymmetric pattern of LEDs with the spacing between individual LEDs larger than the diameter of the cross-correlation spot. Another factor that was taken into consideration was the

detection accuracy required to measure misalignments between the payload mirrors and detectors. The accuracy required determines what pixel size is needed in the BAMS cameras as well as the lens focal length. The plate scale has to be sufficient for the system that BAMS is being designed for and as such, the pixel size of the camera and the focal length of the lens have to be tailored to the fit the requirements of the system. The object distance along with the plate scale determines the maximum ring size that can be used. The LED ring also had to fit into a 256 pixel square box in the BAMS software. A change in object distance will increase or decrease the LED ring size as processed by the BAMS software, and substantially affects the JTC cross-correlation spot. The BAMS setup works with any wavelength as long as a monochromatic FITS file image is provided to the software and as long as the wavelength does not interfere with the science goal of the flight mission.

Future work for BAMS include modifications to the software to determine the effects of tip/tilt or angular misalignment results. Another improvement to be investigated is the ability to determine changing object distance, which requires that tip/tilt effects be taken into account. Testing multiple LED ring patterns will also be done to determine what pattern works best. Other future work includes finding new flight missions that could benefit from BAMS.

References

[1] J. H. Wittke, *Electromagnetic spectrum*, https://www2.nau.edu/micro-analysis/wordpress/index.php/signals/ (Accessed 15 November 2018).

[2] W. H. Tucker, Beam Line. **25** (2), 45 (1995).

[3] D. Schwartz, X-ray Optics X-ray Astronomy School VI, http://cxc.cfa.harvard.edu/xrayschool/talks/optics.pdf (Accessed 19 February 2016).

[4] C. A. Wilson-Hodge, J. Gaskin, S. Christe, A. Shih, A. Tennant, D. Swartz, K. Kilaru, R. Elsner, J. Kolodziejczak, and B. Ramsey, J. Astron. Instrum. **03** (2), 1440007 (2014), https://doi.org/10.1142/S2251171714400078

[5] California Institute of Technology, HEFT Instrument Overview, http://www.srl.caltech.edu/HEFT/instrument.html (Accessed 02 May 2015).

[6] K. P. Singh, J. Opt. **40** (88), 88 (2011).

[7] K. Iniewski, editor, Semiconductor Radiation Detection Systems, 1st ed. (CRC Press, Boca Raton, 2018).

[8] Chandra X-ray Observatory, The Chandra Mission, http://chandra.harvard.edu/about/axaf_mission.html (Accessed 20 Mar 2015).

[9] Chandra X-ray Observatory, Chandra Chandra Spacecraft Components, https://chandra.harvard.edu/graphics/resources/illustrations/craft_lable_300.jpg (Accessed 15 September 2019).

[10] Chandra X-ray Center, Chandra Absolute Astrometric Accuracy, http://cxc.harvard.edu/cal/ASPECT/celmon/ (Accessed 15 March 2015).

[11] Chandra X-ray Observatory, The Chandra Proposers' Observatory Guide, http://cxc.harvard.edu/proposer/POG/html/chap5.html (Accessed 15 March 2015).

[12] F. A. Harrison, S. Boggs, F. Christensen, W. Craig, C. Hailey, D. Stern, W. Zhang, L. A., H. An, V. Bhalerao, N. Brejnholt, L. Cominsky, W. R. Cook, M. Doll, P. Giommi, B. Grefenstette, A. Hornstrup, V. Kaspi, Y. Kim, T. Kitaguchi, J. Koglin, C. C. Liebe, G. Madejski, K. K. Madsen, P. Mao, D. Meier, H. Miyasaka, K. Mori, M. Perri, M. Pivovaroff, S. Puccetti, V. Rana and A. Zoglauer, in: *Proceeding of SPIE 7732, Space Telescopes and Instrumentation 2010: Ultraviolet to Gamma Ray*, edited by M. Arnaud, S. S. Murray and T. Takahashi (SPIE, San Diego, 2010), pp. 1-8.

152

[13] NuSTAR Bringing the High Energy Universe into Focus, About, http://www.nustar.caltech.edu/page/about (Accessed 16 April 2015).

[14] C. C. Liebe, J. Burnham, R. Cook, B. Craig, T. Decker, D. I. Harp, B. Kecman, P. Meras, M. Raffanti, C. Scholz, C. Smith, J. Waldman and J. Wu, in: *2010 IEEE Aerospace Conference* (IEEE, Big Sky, 2010), pp. 1-11

[15] F. Kislat, B. Beheshtipour, P. Dowkontt, V. Guarino, R. Lanzi, T. Okajima, D. Braun, S. Cannon, G. Geronimo, S. Heatwole, J. Hoorman, S. Li, H. Mori, C. Shreves, D. Stuchlik, and H. Krawczynski, J. Astron. Instrum **06** (02), (2017), https://doi.org/10.1142/S2251171717400037

[16] B. D. Ramsey, C. D. Alexander, J. A. Apple, R. A. Austin, C. M. Benson, K. L. Dietz, R. F. Elsner, D. E. Engelhaupt, J. J. Kolodziejczak, S. L. O'Dell, C. O. Speegle, D. A. Swartz, M. C. Weisskopf, and G. Zirnstein, in: Proceedings Volume 4138, X-Ray Optics, Instruments, and Missions IV, (SPIE, San Diego, 2000), https://doi.org/10.1117/12.407554

[17] D. Swartz, Pictures of the Spring 2005 HERO Launch, https://wwwastro.msfc.nasa.gov/research/hero/flight2005_image/HEROLanding1.jpg (Accessed 18 January 2015)

[18] J. Gaskin, J. Apple, K. S. Chavis, K. Dietz, M. Holt, H. Koehler, T. Lis, B. O'Connor, M. R. Otero, J. Pryor, B. Ramsey, M. Rinehart-Dawson, L. Smith, A. Sobey, C. Wilson-Hodge, S. Christe, A. Cramer, M. Edgerton, M. Rodriguez, A. Shih, D. Gregory, J. Jasper, and S. Bohon, in: 2013 IEEE Aerospace Conference, (IEEE, Big Sky, 2013), pp. 1-11, https://doi.org/10.1109/AERO.2013.6497198

[19] T. Lis, J. Gaskin, J. Jasper and D. A. Gregory, Opt. Eng. **57** (1), 013104 (2018). https://doi.org/10.1117/1.OE.57.1.013104

[20] C. M. H. Chen, Ph.D. dissertation, California Institute of Technology, 2008.

[21] North Carolina Climate Office, Structure of the Atmosphere, https://climate.ncsu.edu/edu/Structure (Accessed 03 September 2019).

[22] Rocket and Space Technology, ATMOSPHERE PROPERTIES, http://www.braeunig.us/space/atmos.htm (Accessed 28 January 2016).

[23] Comet MetEd, THE ATMOSPHERE IN THE VERTICAL, https://www.meted.ucar.edu/ams/wim_2014/2b.html (Accessed 08 August 2019).

[24] M. Johnson, Scientific Balloons, https://www.csbf.nasa.gov/mission.html (Accessed 04 October 2015).

[25] E. M. Marconi, What is a Sounding Rocket?, https://www.nasa.gov/missions/research/f_sounding.html (Accessed 13 August 2015).

[26] G. M. Figliozzi, Ballooning experiment to study bacteria on the edge of space, https://phys.org/news/2015-09-ballooning-bacteria-edge-space.html (Accessed 27 July 2015).

[27] M. Johnson, Scientific Balloons, https://www.csbf.nasa.gov/balloons.html (Accessed 05 October 2015).

[28] M. Johnson, NASA - Columbia Scientific Balloon Facility, http://www.csbf.nasa.gov/ (Accessed 29 September 2015).

[29] J. Gaskin, C. Wilson-Hodge, B. Ramsey, J. Apple, K. Dietz, A. Tennant, D. Swartz, S. Christe and A. Shih, in: 2014 IEEE Aerospace Conference, (IEEE, Big Sky, 2014), pp. 1-11, https://doi.org/10.1109/AERO.2014.6836281

[30] S. Christe, A. Shih, M. Rodriguez, K. Gregory, A. Cramer, M. Edgerton, J. Gaskin, B. O'Connor and A. Sobey, in: 2014 IEEE Aerospace Conference, (IEEE, Big Sky, 2014), pp. 1-9, https://doi.org/10.1109/AERO.2014.6836366

[31] R. A. Austin, B. D. Ramsey, C. L. Tse, and C. G. Zirnstein, in: Proceedings Volume 3765, EUV, X-Ray, and Gamma-Ray Instrumentation for Astronomy X, (SPIE, Denver, 1999), https://doi.org/10.1117/12.366553

[32] The Imaging Source, DMK 41BU02.H, http://www.theimagingsource.com/en_US/products/cameras/usb-ccd-mono/dmk41bu02/ (Accessed 15 August 2016).

[33] Edmund Optics, 16mm C Series VIS-NIR Fixed Focal Length Lens, https://www.edmundoptics.com/p/16mm-c-series-vis-nir-fixed-focal-length-lens/22382/ (Accessed 21 September 2012).

[34] Edmund Optics, M25.5 x 0.5 Mounted IR Cut-Off Filter, https://www.edmundoptics.com/p/m255-x-05-mounted-ir-cut-off-filter/10273/ (Accessed 21 September 2012).

[35] Vishay, CQY36N, https://www.vishay.com/docs/81001/cqy36n.pdf (Accessed 12 February 2013).

[36] T. J. Jensen, Budget Astrophotography: Imaging with Your DSLR or Webcam (Springer, New York, 2014), p. 238

[37] W. Goodman, Introduction to Fourier Optics (Roberts and Company Publishers, Greenwood Village, 2007), p. 239

[38] D. Mendlovic, E. Marom and N. Konforti, Opt. Lett. **15** (21), 1224 (1990). https://doi.org/10.1364/OL.15.001224

[39] D. A. Gregory, J. A. Loudin, and F. T. S. Yu, Appl. Opt. **28** (16), 3288 (1989). https://doi.org/10.1364/AO.28.003288

[40] D. A. Gregory, J. C. Kirsch and J. L. Johnson, Appl. Opt. **26** (2), 192 (1987). https://doi.org/10.1364/AO.26.000192

[41] B. Daga, A. Bhute, and A. Ghatol, in: International Conference on Advances in Computing, Communication and Control ICAC3 2011: Advances in Computing, Communication and Control, edited by S. Unnikrishnan, S. Surve, and D. Bhoir (Springer, Berlin, 2011), pp. 457-464, https://doi.org/10.1007/978-3-642-18440-6_58

[42] M. Frigo and S. G. Johnson, Proceedings of the IEEE **93** (2), 216 (2005). https://doi.org/10.1109/JPROC.2004.840301

[43] C. Zhai, M. Shao, R. Goullioud, and B. Nemati, Proceedings: Mathematical, Physical and Engineering Sciences **467** (2136), 3550 (2011). https://doi.org/10.1098/rspa.2011.0255

[44] Nvidia, CUDA Toolkit Documentation, https://docs.nvidia.com/cuda/cufft/index.html (Accessed 15 Feb 2018).

[45] A. A. A. Elfaki, A. A. A. Elfaki, M. D. Abd-Alla, R. A. Elgani, A. S. Mohammed, A. A. Mohammed, A. A. Elamin and S. A. Elhouri, American Journal of Physics and Applications **5** (1), 1 (2017), https://doi.org/10.11648/j.ajpa.20170501.11

[46] X. A. Cao and S. F. LeBoeuf, IEEE Transactions on Electron Devices **54** (12), 3414 (2007). https://doi.org/10.1109/TED.2007.908532

[47] J. A. Gaskin, I. S. Smith and W. V. Jones, J. Astron. Instrum. 03, 1403001 (2014). https://doi.org/10.1142/S2251171714030019

[48] B. F. O'Connor, in: AIAA 43rd International Conference on Environmental Systems, (AIAA, Vail, 2013), https://doi.org/10.2514/6.2013-3467

[49] A. Tennant, HERO_Soft, (NASA MSFC, Huntsville, AL, 2001).

[50] A. Tennant, Lextrct, https://wwwastro.msfc.nasa.gov/qdp/lextrct/lextrct.html (Accessed 10 July 2017).

[51] A. Tennant, lextrct install guide, https://wwwastro.msfc.nasa.gov/ftp/tennant/install.txt (Accessed 29 May 2018).

[52] L. Huang, W. Ma and J. Huang, Journal: New Astronomy **47**, 105 (2016). https://doi.org/10.1016/j.newast.2016.02.007

[53] NASA, Swift/BAT Hard X-ray Transient Monitor, https://swift.gsfc.nasa.gov/results/transients/GRS1915p105.lc.txt (Accessed 27 June 2018).